CFD Optimization of a Net Design and Seakeeping Analysis for an Offshore Fish Cage

Master's Degree Thesis

Facultat de Nàutica de Barcelona
Universitat Politècnica de Catalunya

Author:
Domi Luis Montenegro Castillo

Thesis Committee:
Assoc.Prof. Ir. Daniel Sá - Director
Prof. Dr. Joel Jurado - Co-Director
Prof. Dr. José Enrique Gutiérrez - External

UNIVERSITAT POLITÈCNICA DE CATALUNYA
BARCELONATECH
UPC
Facultat de Nàutica de Barcelona

Acknowledgment

I would like to take a moment to express my heartfelt gratitude to my thesis advisor, Professor Daniel Sa. His guidance and support throughout this project have been truly invaluable. I am incredibly thankful for his unwavering patience, multiple words of wisdom, and constant availability whenever I needed assistance. I want to thank Compass for giving me a free educational license of the software TDYN for one year.

In addition, I would like to extend my sincere appreciation to Dr. Prof. Jose Enrique Gutierrez, whose vast experience and knowledge have played a crucial role in the development of my project. His insightful feedback and expert advice have been instrumental in shaping my understanding and skills. I am grateful for his unwavering support and mentorship throughout this process.

I also want to express my special thanks to Professor Cristian Cifuentes from the Universidad Austral de Chile. It was under his guidance during my undergraduate studies that I was first introduced to the world of aquaculture, his passion for the subject inspired me to pursue this project.

Furthermore, I would like to acknowledge the generous support of the Instituto para la Formación y Aprovechamiento de Recursos Humanos (IFARHU). Their financial assistance has made it possible for me to pursue this master's degree.

Last but certainly not least, I want to express my heartfelt gratitude to my family, my loving girlfriend, and my amazing friends. Their encouragement has been vital in enabling me to achieve excellence and to give my best. I owe all my success in life to them. I would also like to take a moment to honor and remember my late grandfather, who has been a constant source of inspiration and a true role model in my life. His unwavering determination, kindness, and wisdom continue to guide me every day. Though he is no longer with us, his spirit lives on within me, pushing me forward on this journey of self-improvement and growth.

ii

Abstract

The present study conducted a comprehensive examination of the design and analysis of an offshore fish cage based on an existing fish cage known as "Shenlan." Various aspects, including site selection, net type optimization, weights and center of gravity estimation, and seakeeping analysis, were investigated.

The study began with a thorough site selection process, which resulted in the decision to position the fish cage around 20 kilometers from the Massachusetts bay shore, at a water depth of 64.6 meters. The site characteristics, such as wave and wind directions, were obtained from the National Oceanic and Atmospheric Administration (NOAA) database. Extreme condition analysis revealed a significant wave height of 3.1 meters and an average period of 6.5 seconds.

To optimize the net design, Computational Fluid Dynamics (CFD) simulations were conducted using the Tdyn CFD+HT software. Different net types were tested at various speeds, considering the site conditions. The aim was to identify the net type with the most optimal drag coefficient in relation to the solidity ratio. The findings indicated that hexagonal meshes with a solidity ratio of 0.27 performed better than square meshes with similar solidity ratios.

Once the hexagonal net was selected, the weights and center of gravity of the structure were calculated for different draft conditions, taking into account the material, thicknesses, and dimensions of the fish cage. Two conditions were studied: the operational draft (30 m) and the transport draft. A stability study was conducted to ensure safe transport.

A seakeeping analysis was performed using the Tdyn SeaFEM software to assess the fish cage's motions within acceptable limits. The net was modeled using morison elements, considering wave-induced drag and inertia forces. A mooring system arrangement with 8 catenary lines, each 300 meters long and weighing 107 kg/m, was proposed. The simulations, considering 2nd order wave diffraction radiation, revealed a maximum tension of 5291 kN. The selected mooring chain proved capable of withstanding this tension. The surge degree of freedom reached a maximum value of 2.67 m, which was deemed acceptable considering the transit activity at the site.

Contents

List of Tables

List of Figures

Chapter 1

Introduction

1.1 Project Objective

The primary objective of this project is to apply CFD analysis to optimize the size and form of a fish cage net panel based on the type of fish it will hold. The structure will next be subjected to seakeeping calculations for wave, current and wind loads, depending on the site chosen, utilizing the design of an existing fish cage.

In addition to accomplishing its main objective, this project provides a brief introduction of aquaculture as a sustainable industry, the advantages and disadvantages of offshore fish farming, the most recent developments in fish cage technology, and a description of net panels used in fish cages.

1.2 Aquaculture according to the FAO

According to the Food and Agriculture Organization of the United Nations, aquaculture is defined as *"the farming of aquatic organisms including fish, molluscs, crustaceans and aquatic plants. Farming implies some sort of intervention in the rearing process to enhance production, such as regular stocking, feeding, protection from predators, etc. Farming also implies individual or corporate ownership of the stock being cultivated, the planning, development and operation of aquaculture systems, sites, facilities and practices, and the production and transport"*. [1]

Aquaculture has evolved gradually (Figure 1.1), frequently by building on traditional knowledge, positive experience, and mistakes. The consequence has been phenomenal expansion, with aquaculture currently supplying more than half of the world's seafood for human consumption [1].
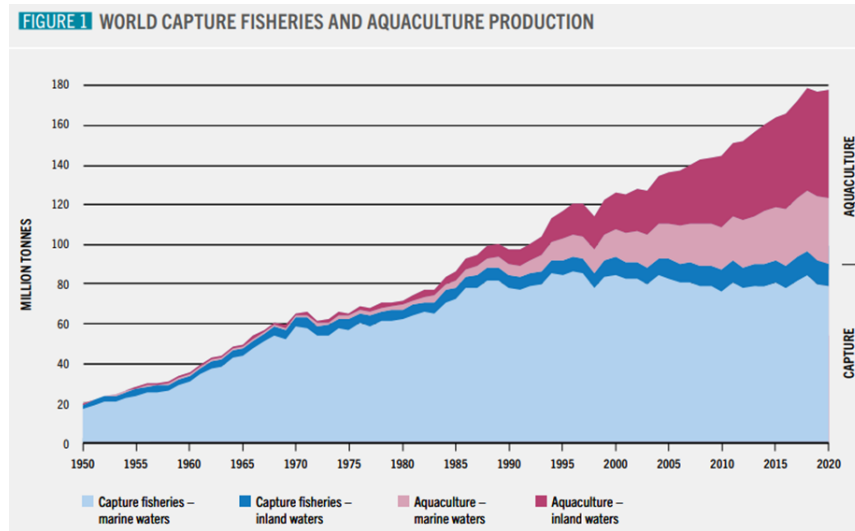
Figure 1.1: *World capture fisheries and aquaculture production.*

The global aquaculture fish production in 2018 was 114.5 million tons (Figure 1.2). Finfish obtained from inland aquaculture, as well as marine and coastal aquaculture, dominated aquatic animal farming in 2018. Inland aquaculture, primarily in freshwater, produced the majority of farmed fish (62.5 percent of the global total) [1].
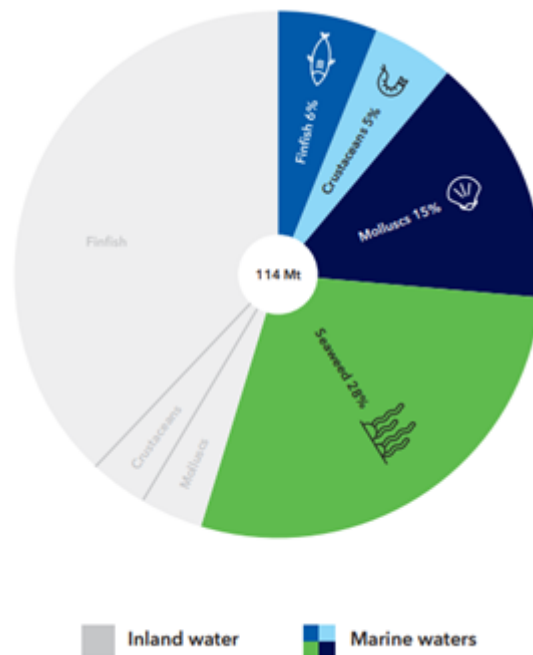
Figure 1.2: *Inland and Marine waters production of species.*

Asia dominates fish farming, producing 89% of the global total in volume terms during the previous 20 years [1]. On growth is carried out in flexible sea cages either in protected coastal regions or in sites more exposed to natural influences in Norwegian

salmon farming [2].

Aquaculture now accounts for more than half of worldwide human fish consumption. From 1961 and 2017, average yearly increases in demand for fish were 3.1% (almost double the annual global population growth rate of 1.6%, Figure 1.3). As a result, aquaculture has become the fastest-growing animal protein food-production industry [3].
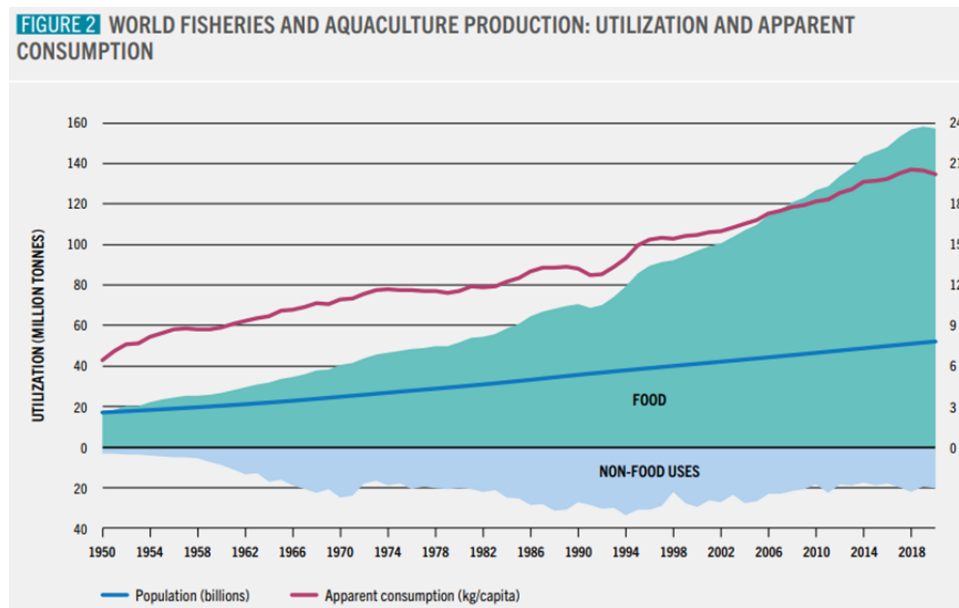
Figure 1.3: *World Fisheries and Aquaculture production: Utilization and Apparent Consumption.*

Aquaculture has indisputably established a critical position in global food security and nutrition, helping to close the supply-demand gap for aquatic food. The beneficial impact of the industry on livelihoods and employment is predicted to expand as productivity and modernization, intensification, and regional access to farmed aquatic goods improve. Aquatic food output is expected to rise by 15% by 2030. This necessitates the creation of innovative, sustainable, and equitable aquaculture development techniques (Figure 1.4) [4]. Growth of sustainable aquaculture will need more technological advances, legislative support, and incentives along the value chain [5].

These include, among other things, access to water, optimizing carrying capacity, excellent environmental standards, regulating the use of chemicals and antibiotics, innovative offshore and onshore production technology, and multifunctional platforms [4].

1.2.1 Advantages and disadvantages

Because there are few chances for sustainable expansion in catch fisheries, the majority of future gains in food production from the seas will have to come from marine aquacul-
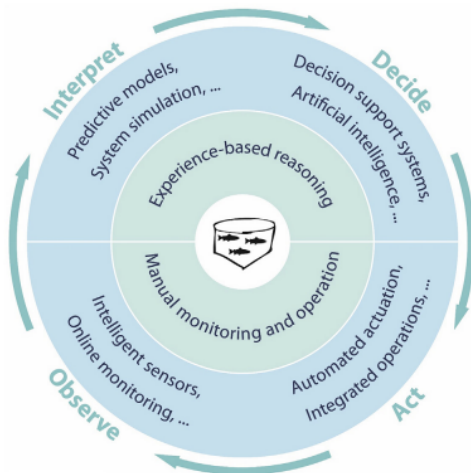
Figure 1.4: *Techniques for making aquaculture sustainable.*

ture [5]. According to the FAO, fish farming is one of the ways to fulfill the increased need of a growing population since fish is an effective protein production technique (Figure 1.5) [6].
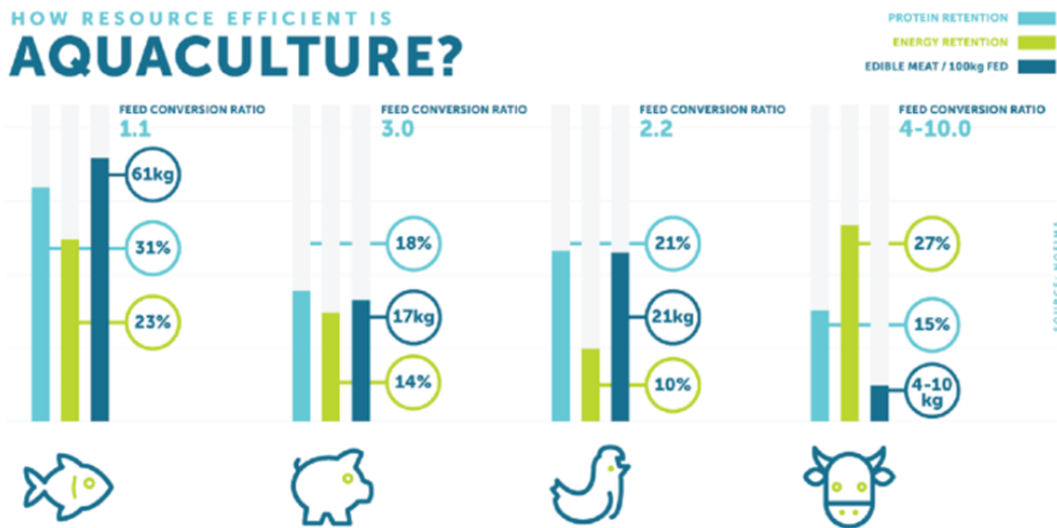
Figure 1.5: *Aquaculture resource efficiency compare with others meat-producing enterprises.*

Farmed seafood has the potential to significantly improve the lives of farmers and their families. Aquaculture, when done properly, may fulfill numerous environmental and social impact goals, including relieving stress on stressed and overfished oceans. The following are some of the benefits that aquaculture may provide to potential farmers and society in this booming sector [7],

- Firm agreements from large seafood purchasers.

- A thriving industry.

- A protein source that is both nutritious and healthier.

- Better for the environment.

Another driver of demand is growing consumer knowledge of the health benefits of seafood over red meat. Aquaculture emits less CO2 (Figure 1.6) and has a lower feed-conversion ratio than other meat-producing enterprises. Fish will become an even more important protein source as a result of this resource-efficient manufacturing [5].
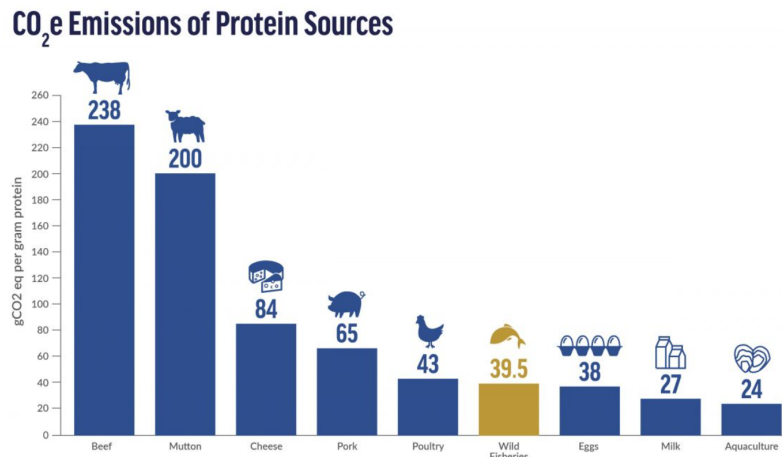
Figure 1.6: *CO2 Emissions of protein sources.*

However, there have been negative environmental consequences, including as habitat degradation, water pollution, the use of hazardous chemicals and veterinary treatments, the influence of escapees on wild stocks, and social and cultural consequences for aquaculture workers and communities [1].

Another major concern is parasite proliferation, which is the most significant danger to the aquaculture business. Sea cages with high fish densities provide a perfect environment for parasites that cause diseases. These infections cause the immune system to weaken, which can end to the animal's death. There is a definite opportunity to lessen parasite burden by situating cages widely apart in more open and dispersed situations [3].

Nevertheless, not all sea creatures are hazardous to fish; marine bivalves and seaweeds are frequently referred to as extractive species because they may improve the ecosystem by collecting waste items, including waste from feeding species, and decreasing the nutrient load in the water [1].

In its current form, the industry is mostly focused on marine cages within sheltered fjordic sea lochs with low water exchange. Because of new techniques, creativity, and technology, nations such as Scotland, Ireland, Norway, Spain, Italy, the United States,
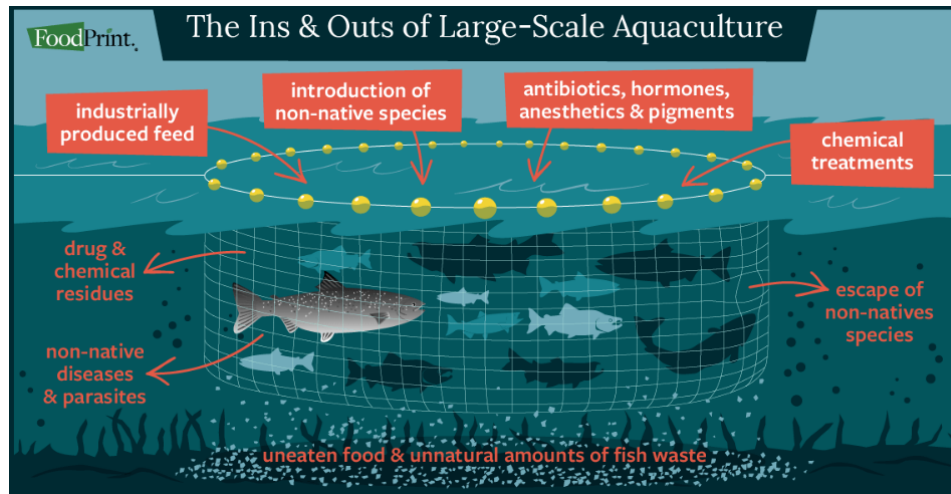
Figure 1.7: *Large-Scale Aquaculture disadvantages.*

and Australia have been involved in offshore aquaculture in recent years [3]. According to experts, offshore facilities are better for salt-water fish [8].

1.3   Offshore Fish Farming

Farm locations in offshore aquaculture are becoming increasingly exposed, with the goal of eventually having entire offshore operations in open rough waters. Offshore aquaculture can be defined as taking place in areas that are at least 3 km from the coastline and in 50 m of water depth [9]. Just a few species, such as salmon and cobia, have the potential to be farmed offshore because their high value allows them to absorb the increased investment necessary, but even if the cost increases, the open system's simplicity makes this approach more competitive today [2] and the scale of offshore fish farms might ensure the profitability of such investment [10]. Australia, China, the Faroe Islands, Norway, and Panama have all been included in groundbreaking work in recent years [5].

Land-based systems rely on regulated aquatic habitats, which need a lot of energy; relocating offshore, on the other hand, implies that the ocean takes care of that [8].

Offshore farms often have harsh production conditions in exposed positions at sea, as well as significant maintenance distances to shore [6].

The shortage of sheltered places for fish farming and the realization that there is plenty of open water in the world are the primary drivers of offshore farming development worldwide. Also, exposed areas can withstand higher nutrient loading, and coasts, rivers, and lakes would be less endangered [6]. Five major processes must be considered while building a sustainable offshore fish farming model, which are described

below [10],

- Fish welfare and growth process.

- The production processes.

- Farm Assets.

- Farm Services.

- Farm site and its environmental loads and conditions.

Figure 1.8 describes the aquaculture production chain.
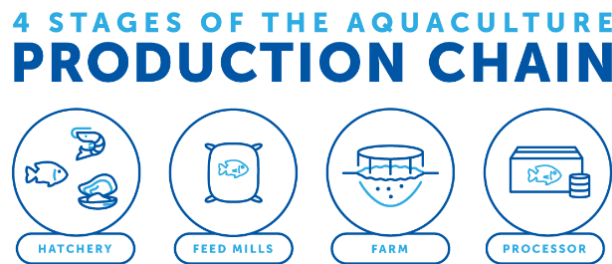
Figure 1.8: *Aquaculture production chain.*

Feeding costs, energy consumption costs, net exchange and cleaning costs, fish treatment costs, maintenance costs, and wages all contribute to the running costs of any offshore fish farm. Treatment and maintenance are the most variable cost categories, with some being predictable and others being more random, but in general, these cost categories have a clear link with environmental loads and events that may raise or reduce their levels [10].

1.3.1   Fish Cages

Nowadays, cage culture is gaining popularity among both researchers and commercial producers because it allows farmers to employ existing water supplies that, in most cases, have limited usage for other purposes [11].

Cage aquaculture is the practice of growing fish in existing water resources while encased in a net cage that permits free flow of clean, oxygenated water and can be placed in a reservoir, river, lake, or sea. Cage culture is a low-impact farming approach with excellent returns and minimal carbon emission activities [11].

Aquaculture cages are divided into four categories: fixed, floating, submersible, and submerged. Because of its enormous culturing volume and simple and visible operation,

the floating gravity type cage is the most extensively used fish cage globally. A floating gravity fish cage is typically made up of four parts: floating collars, flexible nets, bottom sinkers, and a mooring system (Figure 1.9) [12].
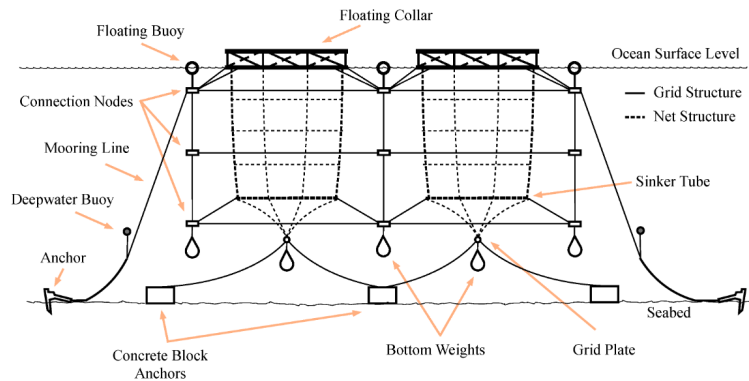
Figure 1.9: *Offshore fish cage layout.*

Farmers may increase aquaculture activities in exposed and vulnerable sea areas using submersible cages (Figure 1.10), increasing the potential productivity of coastal regions while guaranteeing the environmental sustainability of farming sites [11].
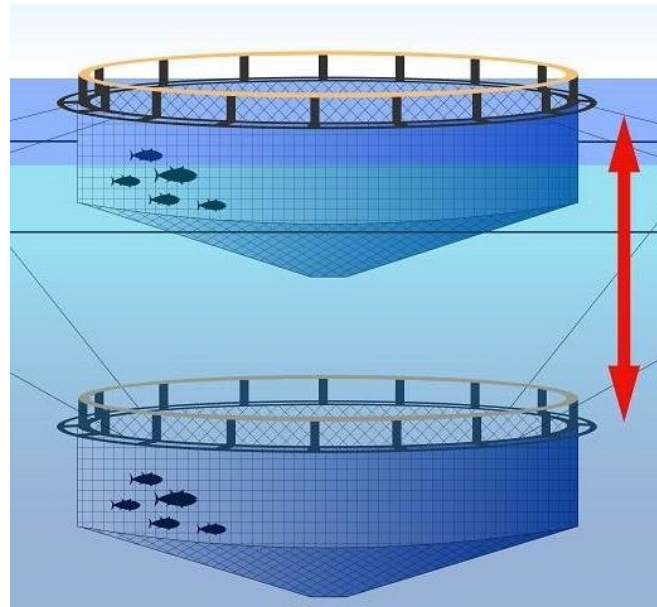
Figure 1.10: *Submersible cage.*

The advantage of adopting a submersible cage over typical floating frames is that it reduces the possibility of biomass loss and, as a result, the possible substantial economic loss [11].

Deeper habitats feature more constant temperatures and salinities (thermoclines and haloclines), are less affected by storms heat waves or swells, and are less preferred

by the infectious stage of troublesome parasites and fouling algal species. Use of sub-merged cages may also open up new production locations when surface-based sea-cage technologies are ineffective owing to surface wind and waves, or due to societal restrictions such as space disputes with other coastal users. As an added bonus, less frequent or severe storm damage to marine cages will reduce the quantity of farmed fish escaping into the wild [13].

Farming of fish in cages: Key Concepts

- Site Selection.

- Cage Size.

- Cage frames and nets.

- Potential species and criteria of selection of species for cage culture.

- Stocking.

- Feeds and feed management.

- Harvest.

- Fouling of cage net.

- Disease monitoring.

1.3.2 Materials used for the net panel

Several developments have occurred in the rope and net sector in recent years. Initially, only steel and natural fibers were used, then polymers and polyamides (nylon) were developed (Figure 1.11a). The former offers chemical composition benefits, such as the fact that water has no effect on their qualities; moreover, their chemical composition results in features such as UV weathering and wet abrasion resistance that are significantly superior to those of other materials [14].

However, there are some drawbacks to using nylon, such as net panel deformations and cage volume reductions due to drag forces in high currents, risks of fish escapes due to net failures in storms, predator attacks or biting behaviors from fish, or the development of biofouling on fish nets, which causes significant problems such as reduced water flows and thereby lower fish welfare [15].

Copper alloy mesh (Figure 1.11b) is reported as a new technology with the potential to improve fish welfare in lower stress conditions, prevent risks of fish losses in storms and escaping from biting behaviors, reduce environmental impacts compared to traditional nylon nets, and avoid biofouling development on the mesh as a new approach

to overcoming these problems encountered in cage farms under high energy conditions. Nevertheless, this alternative introduces other issues, such as heavy weight, corrosion, and a new problem known as "interlocking" [15].

There are also alternative and innovative solutions, such as Econets from AKVA-group (Figure 1.11c). Econets are a new brand and have numerous positive properties in offshore settings, such as preserving their shape and durability, as well as being highly eco-friendly; nevertheless, they are heavier and have a stiff nature [6].

(a) *Nylon.*   (b) *Copper.*   (c) *Econets.*
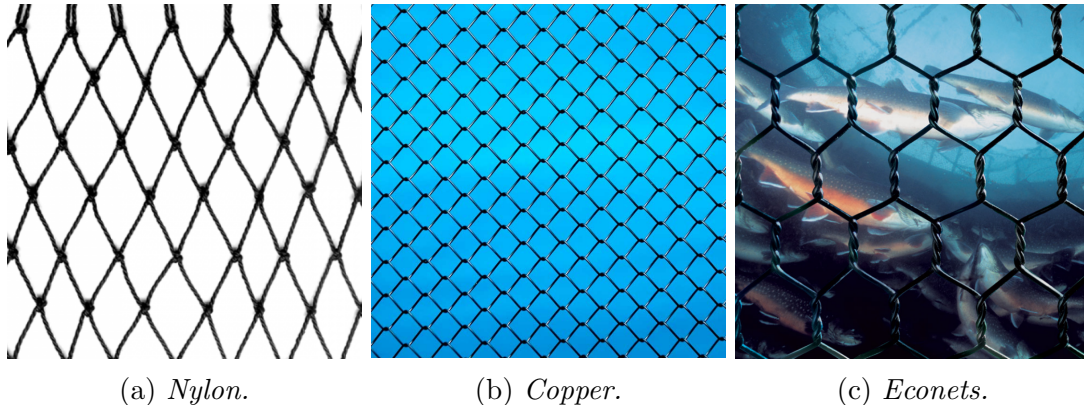
Figure 1.11: *Netting materials used in fish cages.*

Choosing the most effective net panel for a fish cage is critical because sea currents generate forces on cage arrays, causing deformation of the net cage and modifying the available volume for the fish, impacting the fish's behavior. Many experiments have been carried out using multiple net panels (varying in shape and size), such as towing tank experiments or CFD analysis, in an effort to reduce uncertainties in current force calculations, optimize cage system design, and reduce the dimensions of mooring system components.

1.3.3   Advantages and disadvantages of cage culture

Cage culture has advantages which include [11]:

- A relatively low initial investment is required in an existing body of water.

- Harvesting is simplified.

- Observation and sampling of fish is simplified.

- Less manpower requirement.

Cage culture also has some distinct disadvantages. These include [11]:
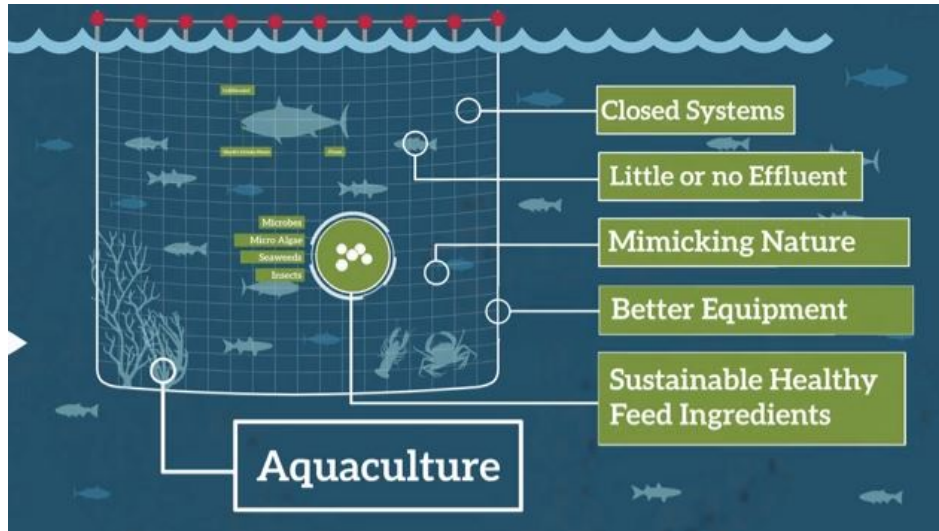
Figure 1.12: *Fish cage's advantages.*

- Low Dissolved Oxygen Syndrome (LODOS).

- Fouling of net cage.

- The incidence of disease can be high, and diseases may spread rapidly.

- Accumulation of unused feed and excreta (water pollution).

- Predation by aquatic mammals and birds.

- Escape.

- Overcrowding of aquatic organisms in cages.

1.3.4   Technological innovation and State of the art offshore aquaculture

What are the requirements for farming fish in the middle of the ocean? In a nutshell, technology. Advocates of offshore farms claim that technology will allow them to scale up in the future years, transforming industrial offshore fishing into industrial production [8].

   "*The fisher of the future is probably going to be sitting down in front of a big bank of computer screens monitoring fish behavior through AI and machine learning that can tell when the fish are hungry*" - Neil Sims (founder of Ocean Era) [8].

   Several corporations (i.e., Ocean Era) are already attempting to address the issue of fish management and experimenting with new forms of fish food to maintain them healthy, since it is not a simple chore to do so 30 to 50 feet deep, as it is on land.

When units get larger and the maintenance distance rises in global offshore farming, two frequent feeding techniques are to employ feed barges or to blow the feed to the fish from the boat. Each method has advantages and downsides [6].

To avoid influencing the genetics of wild fish stocks, companies like Ocean Era strive to produce the same species found outside their nets. To prevent fish from escaping, the industry is also developing strong net mesh enclosures that can resist high-energy offshore environments [8]. In Finland, the most popular choice for growing fish in offshore finfish farms has been to employ durable and flexible plastic rings and net cages. Yet, there are other innovative offshore fish farming ideas, some of which are now in operation (Figure 1.13) [10]

(a) *Ocean Farm.*   (b) *Havfarm.*   (c) *Aquapods.*
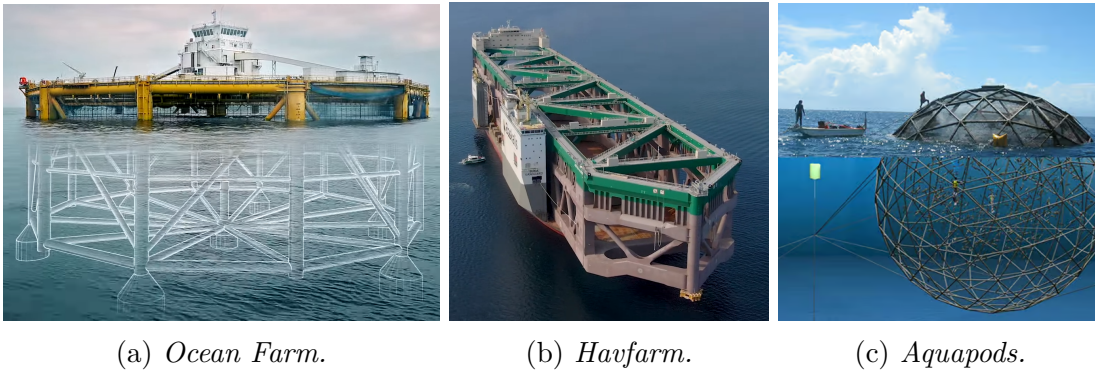
Figure 1.13: *Innovative offshore fish farming designs.*

Chapter 2

Species and Site Selection

2.1 Species Selection

The salmon will be the species chosen for this project, since is often considered one of the best species to farm for several reasons:

- Popularity and Demand: Salmon is a highly popular fish consumed worldwide, and the demand for salmon products continues to grow. This makes salmon farming a lucrative industry with a ready market (Figure 2.1).
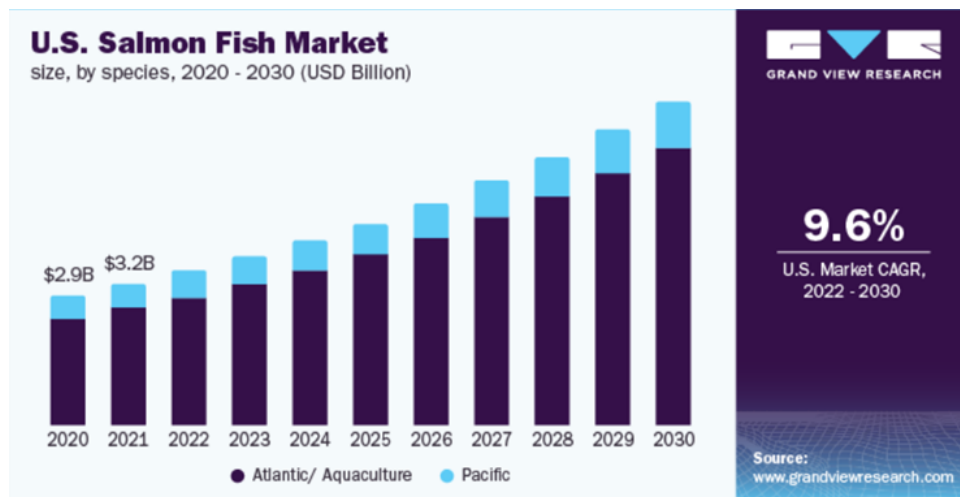
Figure 2.1: *U.S. Atlantic Salmon Fish Market.*

- Fast Growth Rate: Salmon are known for their relatively fast growth rate compared to other fish species and they have a high feed conversion ratio (for salmon, the FGR is around 1.2).

- Nutritional Value: Salmon is highly nutritious, rich in omega-3 fatty acids, high-quality proteins, and essential vitamins and minerals. It is considered a healthy food choice and has various health benefits, including heart health and brain development.

- Well-Researched Species: Salmon farming has been extensively studied and developed over the years, resulting in a wealth of knowledge and best practices.

- Market Size and Premium Pricing: Farmed salmon has a significant market share, complementing wild-caught salmon. The ability to supply a consistent quantity of high-quality salmon throughout the year enables farmers to establish strong relationships with buyers and command premium prices for their products.

The Atlantic Salmon will be the species chosen for this particular scenario. It is the third biggest salmon species and may grow to be one meter long. Atlantic salmon are native to the rivers of the North Atlantic, primarily found in northeastern North America and Europe, and also in South America and Oceania. These fish range in length from 71 cm to 76 cm and weigh between 3.6 kg and 5.4 kg [16].

Atlantic salmon undergo anadromous behavior, meaning they migrate from freshwater to the ocean and back. After hatching from eggs in freshwater rivers, the young salmon, called fry, spend one to three years in freshwater before smolting (a physiological change that allows them to adapt to saltwater). They then migrate to the ocean, where they grow and mature. Upon reaching sexual maturity, usually after two to four years, they return to their home rivers to spawn, and the cycle continues (Figure 2.2 shows the Life Cycle of an Atlantic Salmon).
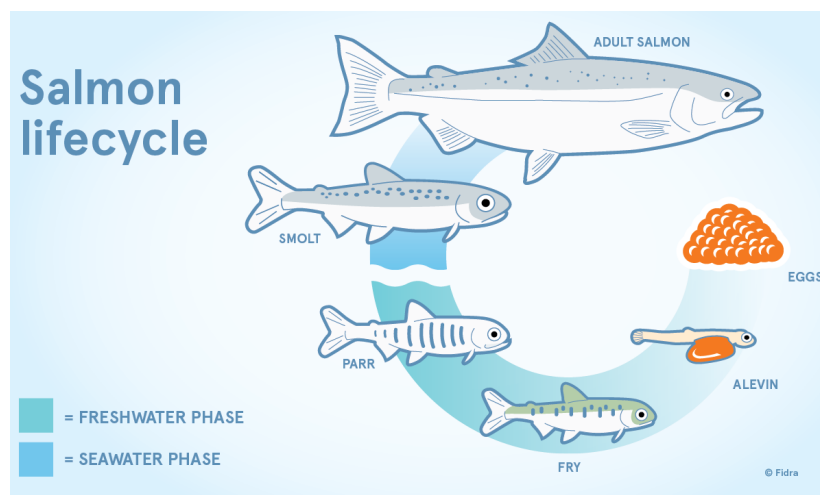
Figure 2.2: *Atlantic Salmon Life Cycle.*

Atlantic salmon is highly valued for its culinary qualities, making it a prized fish for commercial and sport fishing industries. It is considered a delicacy and is often featured in fine dining. Additionally, it plays a significant role in the cultures and traditions of

regions where it is native, such as Scotland, Norway, Canada, and the United States. It is one of the most commonly farmed fish species globally. Aquaculture operations cultivate Atlantic salmon in open net pens or land-based closed containment systems. Farmed Atlantic salmon is an important source of seafood, meeting the high demand for salmon products and reducing pressure on wild populations.

Continuous monitoring of water quality, feeding, disease control, and environmental effect is critical throughout the Atlantic Salmon production process to preserve the fish's health and welfare and to maintain sustainable farming techniques. The following steps are involved in the aquaculture production (Figure 2.3) of Atlantic Salmon:

- Broodstock Management.

- Spawning and Egg Incubation.

- Fry Rearing.

- Smolt Production.

- Marine Rearing.

- Harvesting.

- Processing and Distribution.

2.2 Requirements for Site Selection

Selecting a suitable site for farming Atlantic salmon involves considering various factors, for example water quality. Atlantic salmon requires clean and well-oxygenated water for optimal growth and health. The site should have access to a reliable source of high-quality water with suitable temperature, pH levels, and oxygen content. Conducting water quality assessments and monitoring is essential to ensure the site meets the salmon's requirements. Table 2.1 shows the limit values in seawater, which are capable of supporting salmonids.

Parameter	Limit Values
Oxygen (mg/lt)	5-12
Temperature °(C)	>0-20
pH	6-9

Table 2.1: *Limit Values for water parameters for Salmon Farming.*

The optimal temperature range for farming Atlantic salmon depends on the specific life stage of the fish. Once the smolts are transferred to saltwater for marine rearing, the
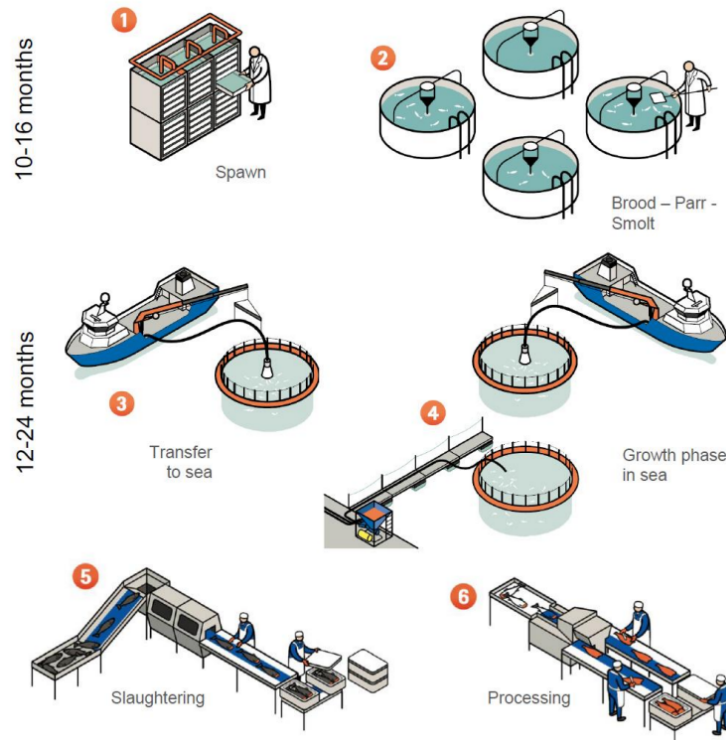
Figure 2.3: *Production Process of Atlantic Salmon in Aquaculture.*

optimal temperature range for Atlantic salmon is generally between 8 ℃ to 15 ℃. These temperatures support optimal growth, feed conversion, and overall health. Although salmon can withstand cold temperatures, temperatures below -5 ℃ are fatal and fish cannot live. It is also vital to note that the upper fatal temperature for post-smolt phases is over 25 ℃ [17].

The minimal amount of oxygen dissolved in the water with which salmon may be kept alive for lengthy periods of time is 5 mg/lt. Levels of 3 mg/lt or less are already deemed fatal. The pH of the water must be between 6 and 9, which are the most typical values of water in nature. Salmon can endure a minor rise or reduction in pH range, although it is best to avoid them since they induce stress [17].

Considering accessibility and closeness to markets near zones with a high demand for salmon is especially essential, because picking a site widely renowned for its product quality and easily accessible for transportation is key for the successful distribution of farmed salmon to markets.

The site should have suitable conditions to ensure the security and safety of the farmed fish. Protection from predators, such as seals or birds, should be considered. The site should have sufficient water flow to flush out waste and maintain optimal oxygen levels. The direction and strength of currents should be favorable for fish health and prevent the accumulation of waste or debris. The meteorological conditions in the

zone, such as significant wave heights, wave periods, wind speeds, and so on, should be considered while assessing the loads on the structure of the fish cage.

As the fish cage is projected to be designed for offshore application and will be moored to the ocean floor, the depth of the site should be tackled, especially because the average depth range of the Atlantic salmon is 10 to 23 m [18].

2.3   Site Selected

Following all of the previous section's criteria, the chosen location is in Massachusetts Bay since it fits most of the basic requirements. The NOAA public database used to choose the buoy station (Figure 2.4) to gather all weather-related data. The buoy is around 20 kilometres from the shoreline, with a 122-yard watch circle radius and a water depth of 64.6 meters.
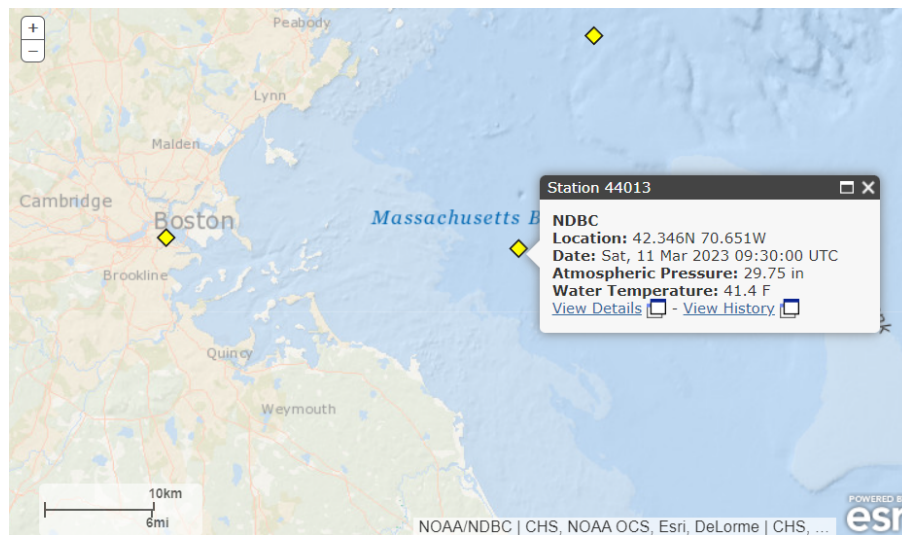
Figure 2.4: *Site Selected - NOAA Station 44013.*

Massachusetts as a state has a notable presence in aquaculture. Several regions within Massachusetts, such as Cape Cod, Martha's Vineyard, and Nantucket, have a long-standing tradition of fish farming. Additionally, Massachusetts has made efforts to promote sustainable aquaculture practices and has several research institutions dedicated to marine science and aquaculture, such as the Woods Hole Oceanographic Institution and the University of Massachusetts Dartmouth's School for Marine Science and Technology. As a result, it was determined that Massachusetts is an excellent location for developing the fish cage for this project.

2.4   Sea Water Parameters

2.4.1   Temperature

For each month from 1984 to 2008, the values for the maximum, minimum, and average sea temperatures (°C) are shown in Table 2.2, along with the quartiles and the standard deviation.

Sea Temperature (°C)						
Date	Max	Mean	75PCTL	50PCTL	25PCTL	S.D.
august/1984 - august/2008	23.2	18.3	19.4	18.3	17.3	1.5
september/1984 - september/2008	22.2	16.4	17.3	16.4	15.2	1.5
october/1984 - october/2008	17.5	12.6	13.4	12.5	11.7	1.4
november/1984 - november/2008	12.5	9.5	10.3	9.4	8.7	1.0
december/1984 - december/2008	10.2	6.8	7.6	6.7	6.0	1.1
january/1985 - january/2008	7.8	4.4	5.2	4.4	3.6	1.1
february/1985 - february/2008	5.5	3.0	3.5	2.9	2.4	0.8
march/1985 - march/2008	7.1	3.1	3.6	3.1	2.5	0.9
april/1985 - april/2008	11.4	5.4	6.3	5.2	4.4	1.4
may/1985 - may/2008	17.2	9.5	11.0	9.4	8.0	2.0
june/1985 - june/2008	22.7	14.2	15.7	14.2	12.6	2.2
july/1985 - july/2008	24.2	17.5	18.7	17.5	16.5	1.7

Table 2.2: *Station 44013 Sea Temperature (°C) 8/1984 - 12/2008.*

Table 2.2 shows that the maximum and minimum sea temperatures ever recorded from 1984 to 2008 were 24.2° and 3.0°, respectively, with an average of all mean values of 10.1° . As a result, the temperature of the zone is suitable for Atlantic Salmon farming based on the sea water parameter restrictions from Table 2.1.

2.4.2   Oxygen

In Massachusetts Bay, the dissolved oxygen levels typically range from approximately 7 to 9 milligrams per liter (mg/L) or parts per million (ppm), according to the Massachusetts Division of Marine Fisheries [19]. These values are within the recommended range for marine rearing of Atlantic salmon in aquaculture, as mentioned earlier.

2.4.3   pH

Figure 2.5 a pH mapping of the ocean's surface. The color scale shows that the range of values is between 8.1 and 8.05, indicating that the pH level in the open sea will always be suitable for farming Atlantic Salmon.
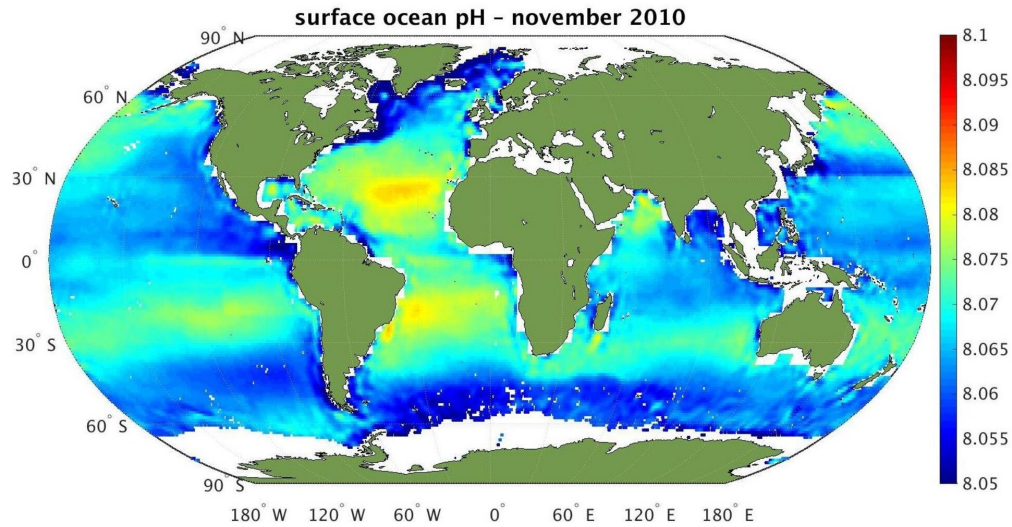
Figure 2.5: *Surface Ocean pH.*

2.5 Wind Speed

Table 2.6 shows the frequency of average wind speeds against average wind directions for each month from 1984 to 2008.

Wind Speed	N	NE	E	SE	S	SW	W	NW	Tot %
0-3	0.675	1.05	0.475	1.05	0.575	1.35	0.675	1.25	7.1
4-6	1.2	1.9	0.9	1.9	1.4	3.4	1.7	3.1	15.5
7-10	1.5	2.8	1.6	3.8	2.4	6.5	2.8	5.4	26.8
11-15	0.8	2.7	1.7	4.9	2.6	5.8	2.2	3.6	24.3
16-20	0.4	2.2	1.1	4.7	2.5	2.9	0.8	1.3	15.9
21-24	0.2	0.8	0.4	2.1	1.3	0.8	0.1	0.3	6
25-33	0.1	0.7	0.4	1.2	1	0.3	0.1	0.2	4
34-47	0.1	0.2	0	0	0	0	0	0.1	0.4
> 48	0	0	0	0	0	0	0	0	0
Tot %	4.975	12.35	6.575	19.65	11.775	21.05	8.375	15.25	100

Figure 2.6: *Percent Frequency of Average Wind Speed vs Average Wind Direction (1984-2008).*

Figure 2.7 displays the wind rose from the buoy's data obtained from the NOAA. The data show that the average wind direction with the highest frequency is southwest, and the average wind speed with the highest frequency is between 7 and 10 knots.
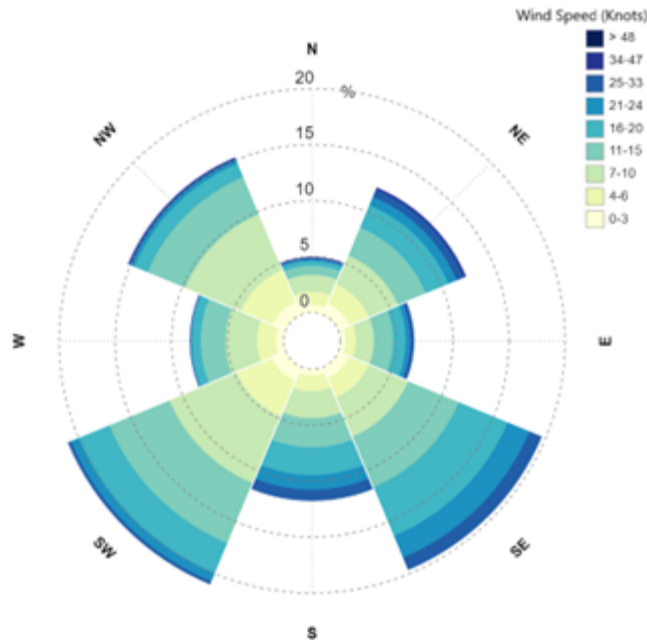
Figure 2.7: *Station 44103 Wind Rose (1984-2008).*

2.6   Current Speed

Generally, the average current speeds in Massachusetts Bay range from 0.5 to 2 knots (0.5 to 2 nautical miles per hour). However, it's important to note that currents can be stronger in certain areas and during specific tidal phases.

The currents in Massachusetts Bay can vary depending on factors such as tidal cycles, wind patterns, and specific locations within the bay. Massachusetts Bay is part of the Gulf of Maine, which is known for its complex oceanographic conditions. Because of the latter, it was difficult to find a complete database with enough data to set the current speeds.

Figure 2.8 and Figure 2.9 show the current speeds observed during May and June of 2011 at sea depths of 9.02 m and 17.01 m [20]. At 9.02 m, the average current speed is around 0.5 m/s, whereas at 17.01 m, the average current speed is around 0.35 m/s. These current speeds were chosen to be considered for the design of the fish cage, as well as a current speed of 0.65 m/s, which is roughly the average of the higher current speed values at both depths.

2.7   Wave Direction

Table 2.10 shows the frequency of average significant wave heights against average wave directions for each month from 1984 to 2008.
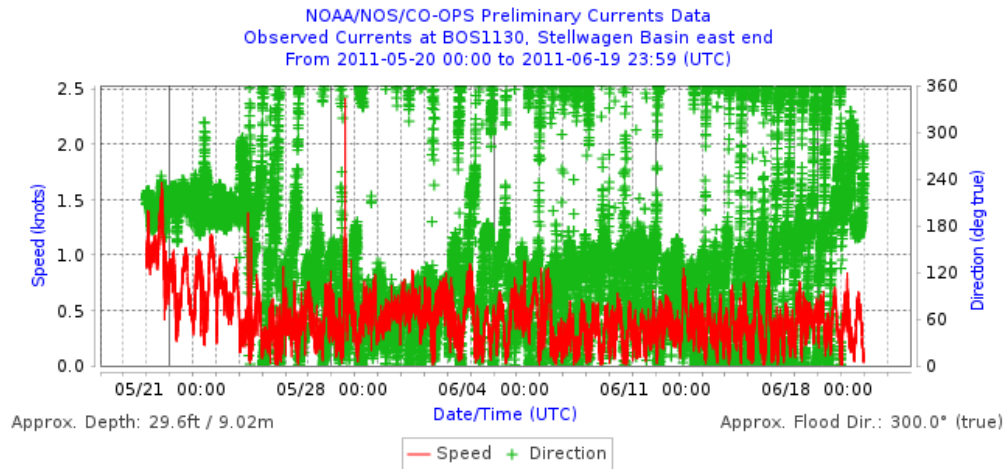
Figure 2.8: *NOAA Observed Current Data. Depth: 9.02 m.*
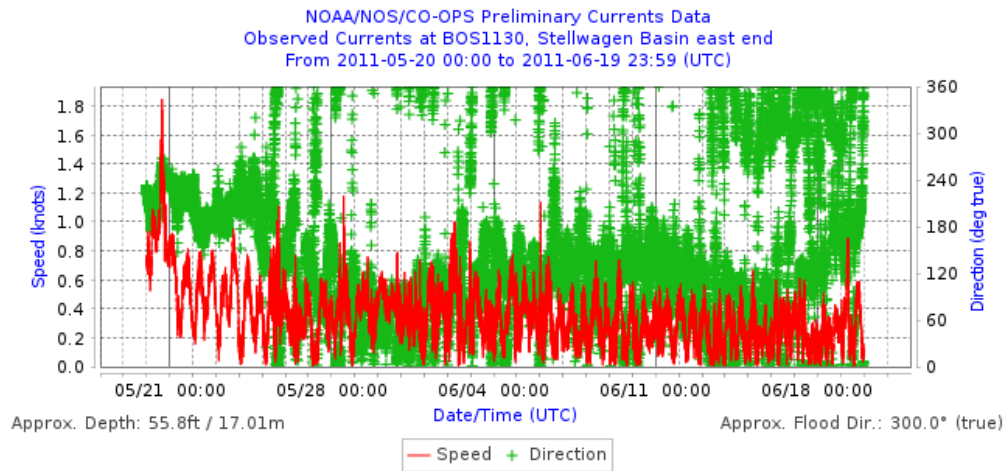
Figure 2.9: *NOAA Observed Current Data. Depth: 17.01 m.*

Wave Height	N	NE	E	SE	S	SW	W	NW	Tot %
< 0.5	17.6	2.8	0.1	0.6	0.4	0.4	0.2	3.9	26
0.5 - 1.4	26.8	9	0.9	8.5	3.4	2.2	0.6	8.1	59.5
1.5 - 2.4	5	3.3	0	0.9	0.3	0.1	0	1	10.6
2.5 - 3.4	1.3	1	0	0	0	0.1	0	0.1	2.5
3.5 - 4.4	0.5	0.4	0	0	0	0	0	0	0.9
4.5 - 5.4	0.2	0.2	0	0	0	0	0	0	0.4
> 5.5	0	0.1	0	0	0	0	0	0	0.1
Tot %	51.4	16.8	1	10	4.1	2.8	0.8	13.1	100

Figure 2.10: *Percent Frequency of Significant Wave Height vs Average Wave Direction (1984-2008).*

Figure 2.11 displays the wave direction rose from the buoy's data obtained from the NOAA. The data show that the average wave direction with the highest frequency is north, and the average significant wave height with the highest frequency is between

0.5 and 1.4 m.
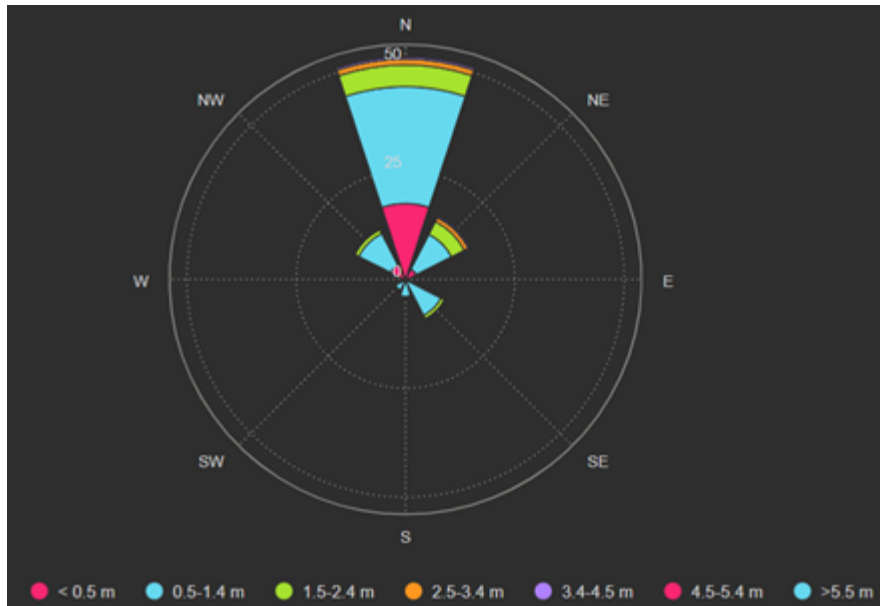
Figure 2.11: *Station 44103 Wave Direction Rose (1984-2008).*

2.8   Extreme Design Wave

The estimate of an extreme design wave based on recorded or hindcast wave data is a crucial design phase. Selecting and fitting an appropriate probability distribution to wave height data and extrapolating to a suitable design wave with a set return period are the general steps. The actual choice of a design wave is a matter of engineering judgement and will vary depending on the risk level chosen for the design.

The first step in selecting a design wave is to collect oceanographic data over a long period of time. For this study, it was decided to consider all the data from the year 2019 at the site of interest. Figure 2.12 depicts a plot of the significant wave height vs the average period of all data gathered; a power regression was used to establish the relationship between the two variables. As can be seen, the correlation obtained is 0.25, which is quite low, consequently after the design has been determined, it will be impractical to estimate the average period using the regression.

The significant wave heights are then divided into bins and their exceedance probabilities are calculated depending on the frequency of each one. Figure 2.13 presents the histogram plotted from the significant wave height bins and the frequency with which they occur.
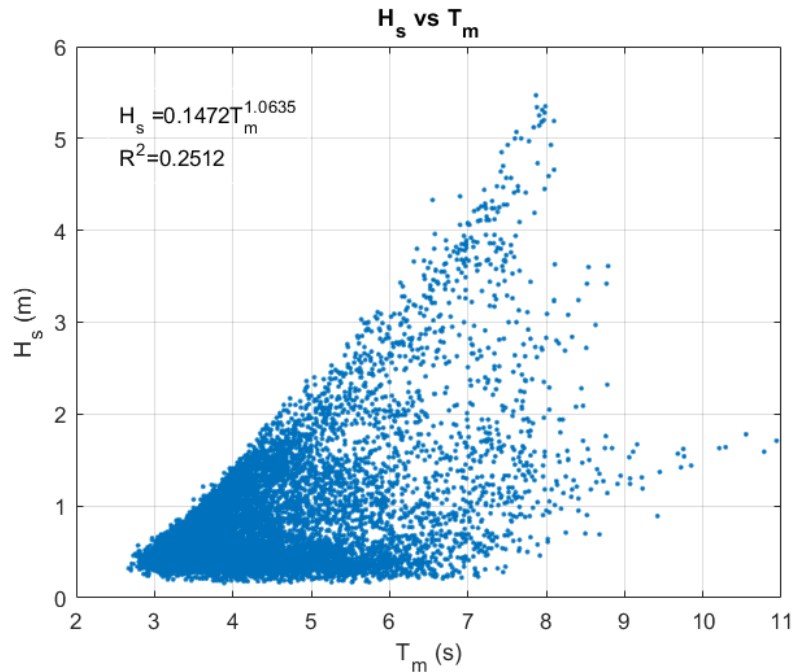
Figure 2.12: *Significant Wave Height vs Average Period. 2019 Data Buoy Station 44013.*
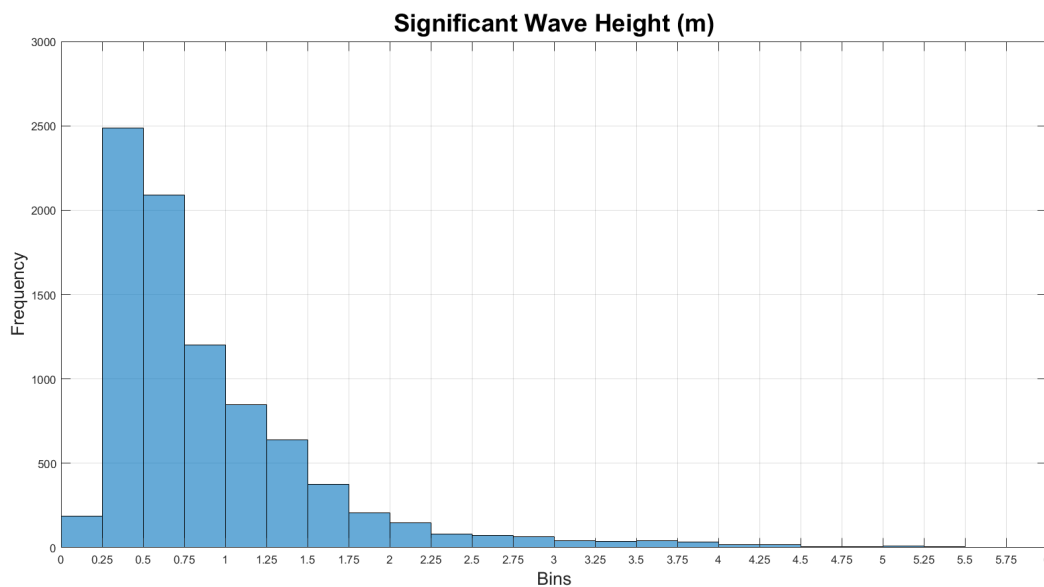
Figure 2.13: *Significant Wave Height Histogram.*

2.8.1 Weibull Distribution

Following the collection of all data, a plotting formula is employed to convert the data to a set of points reflecting the probability distribution of wave heights. These

points are plotted on extreme value probability corresponding to the desired probability distribution function. The Weibull function was used for the probability distribution in this study.

$$P\left(H_s\right) = 1 - exp\left\{-\left(\frac{H_s - \alpha}{\beta}\right)^{\gamma}\right\} \tag{2.1}$$

Where,

- $P(H_S)$ is the cumulative distribution function at a significant wave height (exceedance probability).

- α: Shape parameter.

- β: Scale parameter.

- γ: Location parameter.

To acquire these parameters, the Weibull function must first be adjusted into a linear curve. A few mathematical procedures must be done in order to accomplish this. Finally, the formula for a two-parameter Weibull is as follows,

$$\ln\left(-\ln\left(1 - P\left(H_s\right)\right)\right) = A \cdot \ln\left(H_s\right) + B \tag{2.2}$$

Where,

$$A = \gamma \tag{2.3}$$

$$\beta = e^{\frac{-B}{A}} \tag{2.4}$$

Hence, by graphing the preceding equation using the values acquired from the cumulative probability function, these parameters may be determined by fitting a straight line through the points to present a trend (Figure 2.14). Finally, the slope of the trendline will be the location parameter (γ) and the intersection with the axis will assist to obtain the scale parameter (β).

Table 2.3 contains the Weibull parameters obtained from the data.

Parameter	
α	0.0000
β	0.8525
γ	1.4643
R^2	0.9061

Table 2.3: *Weibull probability distribution function parameters.*
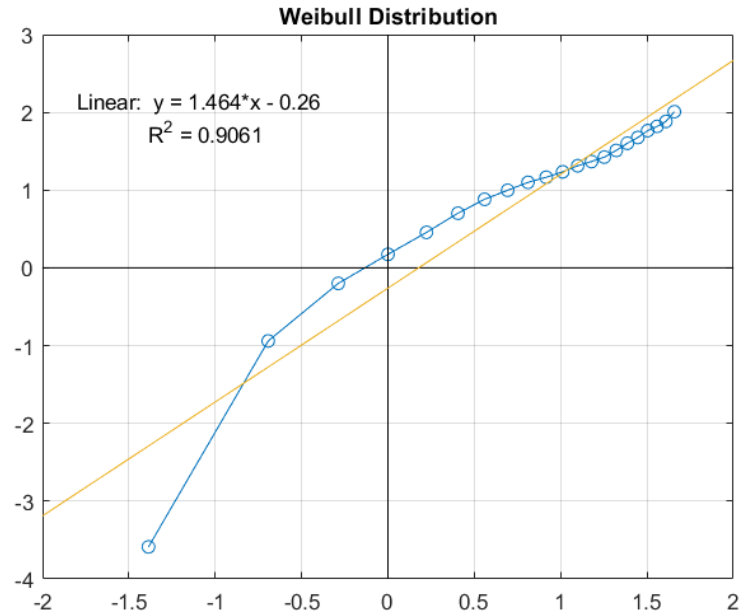
Figure 2.14: *Weibull Plot.*

2.8.2   Extreme Design Wave Height and Average Period

After obtaining the Weibull parameters, the maximum predicted wave height is calculated using the following formula,

$$H_d = \beta \left(-ln \left(\frac{1}{\lambda T_R} \right) \right)^{\frac{1}{\gamma}} + \alpha \tag{2.5}$$

Where,

- λ is the average number of storms in a particular year. It is common to find a number of storms ranging from 12 to 24 every year, thus in this case, a number of 15 was selected based on NOAA statistics.

- T_R is the return period. The American Bureau Society (ABS) claims that the rule stipulates a minimum return period of 100 years for manned floating fish farming installations and a minimum return period of 50 years for unmanned floating fish farms when combining current, wind, and wave [21]; hence, it is important to defined whether the fish cage will be manned or unmanned. For this study it was decided to consider an unmanned installation, therefore the return period must be given a value of 50 years.

Based on the assumptions and regulations evaluated, as well as the Weibull parameters input into the equation for determining the highest expected wave height, the

extreme design wave height obtained is,

$$H_d = \beta \left(-ln\left(\frac{1}{\lambda T_R}\right)\right)^{\frac{1}{\gamma}} + \alpha = 3.1 \ m \qquad (2.6)$$

After obtaining the extreme design wave height, the final step is to calculate the average wave period for the obtained wave height. However, it is important to consider that the correlation between the significant wave height and the average wave period obtained from the data was relatively poor, therefore, a different approach must be used in order to calculate the average period.

It was determined to depend on NOAA data to estimate the average wave period by combining the probabilities of the significant wave height and the average wave period from 1984 to 2008 (Table 2.15). Given that the extreme wave height estimated is 3.1 m, the range of wave heights chosen should be 2.5-3.4; therefore, the most probable average wave period range for the given range of significant wave heights is 6.0 - 6.9, according to the data. Based on this, it was determined that the average wave period should have a value of 6.5 s.

Wave Period	0.0 - 0.4	0.5 - 1.4	1.5 - 2.4	2.5 - 3.4	3.5 - 4.4	4.5 - 5.4	5.5 - 6.4	6.5 - 7.4	7.5 - 8.4	8.5 - 9.4	9.5 - 10.4	10.5 - 11.4	11.5 - 12.4	12.5 - 13.4	>13.4	Tot %
< 3.0	0.2	0.1	0	0	0	0	0	0	0	0	0	0	0	0	0	0.3
3.0 - 3.9	6	16.8	0	0	0	0	0	0	0	0	0	0	0	0	0	22.8
4.0 - 4.9	8.6	15.5	2.7	0	0	0	0	0	0	0	0	0	0	0	0	26.8
5.0 - 5.9	8.7	9.6	3.4	0.5	0	0	0	0	0	0	0	0	0	0	0	22.2
6.0 - 6.9	5.7	6.8	2	1.1	0.3	0	0	0	0	0	0	0	0	0	0	15.9
7.0 - 7.9	2.2	3.9	1	0.5	0.3	0.2	0	0	0	0	0	0	0	0	0	8.1
8.0 - 8.9	0.6	1.5	0.4	0.2	0.1	0.1	0.1	0	0	0	0	0	0	0	0	3
9.0 - 9.9	0.1	0.5	0.1	0	0	0	0	0	0	0	0	0	0	0	0	0.7
10.0 - 11.0	0	0.2	0	0	0	0	0	0	0	0	0	0	0	0	0	0.2
>11.0	0	0	0	0	0	0	0	0	0	0	0	0	0	0	0	0
Tot %	32.1	54.9	9.6	2.3	0.7	0.3	0.1	0	0	0	0	0	0	0	0	100

Figure 2.15: *Percent Frequency of Average Wave Period vs Significant Wave Height (1984-2008).*

Chapter 3

Net Panels

3.1 Theory

3.1.1 Solidity Ratio

The ratio of the projected area (A_p) (normal to the net plane) of all threads to the outline area of the complete net panel (A) is a common way to describe the solidity (Sn) of nets and its hydrodynamic performance [22], solidity can be expressed as

$$S_n = \frac{A_p}{A} \tag{3.1}$$

Where,

- A is the outline area of the entire net panel [m^2].

- A_p is the project area of the net panel, considering the twines and knots of it [m^2].

Figure 3.1 provides two visual illustrations of each of the variables used to calculate the solidity ratio.

One of the most important criteria used to define the performance of the net is the solidity ratio since an increase in the solidity ratio owing to an increase in the projected area might result in an increase in the drag force [23], and it is well known that the drag force is also affected by the drag coefficient, which is the characteristic that truly defines a net.

(a) A (b) A_p
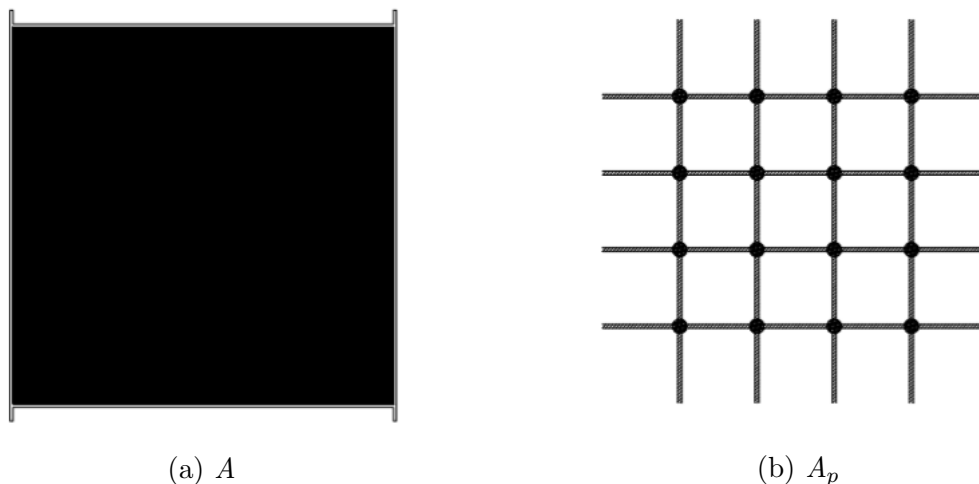
Figure 3.1: *Graphic example of areas used for calculating the solidity ratio.*

3.1.2   Reynolds Number

Unquestionably, the Reynolds number is the most well-known dimensionless parameter in fluid mechanics. It bears the name Osborne Reynolds in recognition of the British engineer who was the first to show how this set of factors may be used as a criterion to distinguish between laminar and turbulent flow. The density and viscosity of the fluid, as well as its characteristic length and velocity, will all be important factors in the majority of fluid flow issues [24].

The Reynolds number is a measure of the ratio of the inertia force on an element of fluid to the viscous force on an element. If the Reynolds number is small ($R_n < 2000$ in water), viscous effects are dominant over the inertial effects, so it may be possible to neglect them. On the other hand, if the Reynolds number is bigger than 10000 for water, this is an indication that inertial effects are big relative to viscous effects, so it may be possible to consider the problem as one involving a "no viscous" fluid. The typical Reynolds number for fish cage nettings is in the range of 100–10 000, meaning that for a net the viscous effects are going to be greater.

The Reynolds Number of a net panel can be calculated using the following expression according to [25],

$$R_n = \frac{d_w U_{rel}}{v(1 - S_n)} \tag{3.2}$$

Where,

- d_w is the diameter of the net twine [m].

- U_{rel} is the relative speed between the inlet fluid and the net (m/s).

- S_n is the solidity ratio.

- ν is the kinematic viscosity [m^2/s].

3.1.3 Drag Coefficient

The Drag Force is a net force in the direction of flow caused by pressure and shear forces on the object's surface. This net force is a sum of the flow direction components of the normal and tangential forces acting on the body [24]. The Drag Force is expressed as,

$$D = \frac{1}{2}\rho A_p V^2 C_d \qquad (3.3)$$

Where,

- ρ is the fluid density [kg/m^3].

- A$_p$ is the project area normal to the fluid [m^2].

- V is the fluid speed [m/s].

- C$_D$ is the non-dimensional drag coefficient.

The most challenging task is calculating the drag coefficient. To acquire the C$_D$ of a body, one might conduct a towing test and compute the drag coefficient based on the drag forces obtained during the test at various speeds by simply calculating the previous equation for C$_D$,

$$C_D = \frac{2D}{\rho A_p V^2} \qquad (3.4)$$

Another alternative is to employ computational fluid dynamics, or CFD (the use of computers to solve the governing equations of the flow field), which has shown promising results for more complicated forms.

The drag coefficient for a net panel depends on the Reynolds Number and the Solidity Ratio, which is why it is critical to take into account the previously mentioned values while assessing the Drag Coefficient. Once the Drag Coefficient of a Net Panel is identified, the acting forces on the Net Panel can be estimated, allowing the structure of the Fish Cage and the mooring system components to be dimensioned.

Many additional authors have presented formulae for calculating the drag coefficient. Aarsnes et al. [26] investigated net deformation caused by forces applied to fish cages in order to calculate the weights required to keep the net upright. He evaluated the following factors for his experiments: fluid velocity, net angle of attack (the angle between the net frame and the vertical axis), and solidity ratio. He presented the following expression based on his findings,

$$C_D = 0.04 + \left(-0.04 + S_n - 1.25S_n^2 + 13.75S_n^3\right)\cos\left(\alpha\right) \qquad (3.5)$$

This equation is only applicable to nets with solidity ratios less than 0.35. The attack angles ranged from 0° to 90°. It is necessary to note that his expression does not take the Reynolds Numbers or the fluid velocity into account, and there is no indication of whether the nets had knots or not.

Hao Tang et al. [27] provided the following equation for determining the drag coefficient for nets without knots,

$$C_D = 0.172 S_n^{-0.407} R_n^{-0.031} (1 + \sin \theta^{0.905})^{1.822} \tag{3.6}$$

The attack angle, Reynolds Numbers, and solidity radio are the inputs of this equation. The acceptable solidity ratio range for this equation is 0.047 to 0.217, with angles of attack ranging from 0° to 20°.

Kristiansen et al. [25] proposed an equation that incorporates a new input parameter, the drag coefficient of a circular cylinder.

$$C_D = \frac{C_D^{circ.cyl} S_n (2 - S_n)}{2(1 - S_n)^2} cos^2\theta \tag{3.7}$$

For calculating the $C_D^{circ.cyl}$, the following expression needs to be applied,

$$
\begin{aligned}
C_D^{circ.cyl} =\ & -78.46675 + 254.73873 \left(log_{10}Re\right) - 327.8864 \left(log_{10}Re\right)^2 + 223.64577 \left(log_{10}Re\right)^3 \\
& - 87.92234 \left(log_{10}Re\right)^4 + 20.00769 \left(log_{10}Re\right)^5 - 2.44894 \left(log_{10}Re\right)^6 \\
& + 0.12479 \left(log_{10}Re\right)^7
\end{aligned}
\tag{3.8}
$$

However, in order to apply the formula, the input parameters must be in the following range:

- $S_n \leq 0.5$

- $10^{3/2} \leq R_n \leq 10^4$

- $0 \leq \theta \leq \pi/2$

Many CFD analyses will be performed for this project in order to obtain the drag forces on different net panels with different solidity ratios by varying the speeds, in order to obtain the drag coefficient for each one of them, so that the results can be contrasted and the most suitable net for the fish cage can be chosen.

3.2   Aspects to consider for the net in Salmon Farming

3.2.1   Mesh Size

Net solidities currently used in Norwegian salmon farming range between 0.20 and 0.29 [28] (0.19-0.43, including biofouling [29]). The most common nets are square meshing of either 30 mm (15 mm bar length) or 50 mm (25 mm bar length) mesh size (2–3 mm polyamide twine), depending on the sizes of fish that the cage is intended to hold.

It is critical to assess the mesh size, shape, and state in connection to fish size that will be used in the fish cage since it is one of the most essential aspects to consider in the danger of smolt escape from fish farming cages.

Fish escape is a significant problem for the fish farming sector, not only because it costs fish farmers money, but also because it endangers wild salmon in the ecosystem. The issue is more serious when smolt escape rather than adult salmon since salmon smolt may more quickly adapt to circumstances in the wild and endanger wild salmon stocks.

For a variety of reasons, fish can escape from salmon cages. One potential cause is cage netting if the mesh is improperly designed for the smolt size. Therefore, it is crucial for the business to determine the optimum mesh size for various conditions (smolt minimum sizes vs. mesh attributes). While the netting used completely determines the mesh size in the cages, the mesh shape is less well defined because it is influenced by how the netting is initially mounted on the cages as well as how the netting behaves when exposed to varying sea conditions, altering the overall shape of the cage netting and the condition of the mesh bars (Figure 3.2).
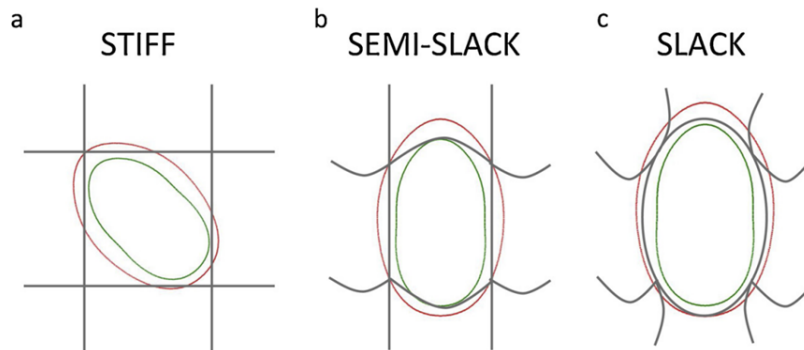
Figure 3.2: *Different behavior in which a single mesh bar shape can deform. (a) Stiff: Stable (b) Semi-Slack: Partially deformed (c) Slack: Totally Deformed.*

3.2.2   Biofouling

Biofouling blocking mesh openings (Figure 3.3) has a number of negative effects, including increasing the structure's weight, limiting the flow of water through the nets, and increasing drag forces on fish cages, though it was discovered that an increase in solidity due to hydroids caused less additional drag than an increase caused by a change in the parameters of clean nets. These influences affect the volume and quality of water in net pens, as well as how fish cages respond in waves and currents [30].
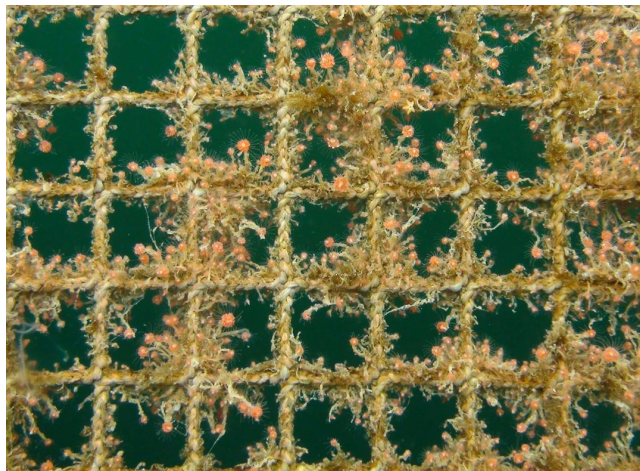
Figure 3.3: *Biofouling in a net panel.*

Regulations such as the Norwegian Standard NS9415 acknowledge the importance of biofouling when considering the forces on aquaculture constructions. This standard asks for a solidity increase with 50% to account for fouling.

3.3   Net Panels Modelled for CFD Analysis

This section describes the main dimensions of the net panels modelled for the fish cage. It was chosen to study two potential mesh designs for the fish cage based on the information provided: a square mesh and a hexagonal mesh. Three different sizes will be used for each of these meshes, giving a total of six solidity ratios.

It was deemed essential that the solidity ratio of the net panels should be within a range of 0.2 and 0.29, based on the net solidities usually used in Norway, as the fish cage will be used to farm Atlantic salmon. The solidities ratios obtained from the net panels modelled in 3D, range approximately from 0.2 to 0.27. The software Rhinoceros was used for modelling the nets.

To compare the drag coefficients of square and hexagonal meshes, the mesh sizes and thicknesses for the square and hexagonal meshes are the same, which means that

the resulting net solidities for each shape are as near as possible.

In order to lower the computing cost of the CFD study, the meshes were designed as tiny as possible. It is also worth noting that the meshes are symmetrical to the vertical axis, which means that only half of the mesh is simulated, and the other half can be reproduced by using a symmetrical condition as an input.

3.3.1 Square Mesh

The primary dimensions for each of the square meshes that were modelled are displayed in Table 3.1.

Item	L (mm)	T (mm)	Net Area (mm^2)	Frame Area (mm^2)	S$_n$
15-2	15	2	1024	4624	0.221
13-2	13	2	896	3600	0.249
17-3	17	3	1872	7056	0.265

Table 3.1: *Square Mesh main dimensions.*

Figure 3.4 depicts the projected area of the square mesh as well as a description of its primary parameters.

(a) *Projected area.* (b) *Main dimensions description.*
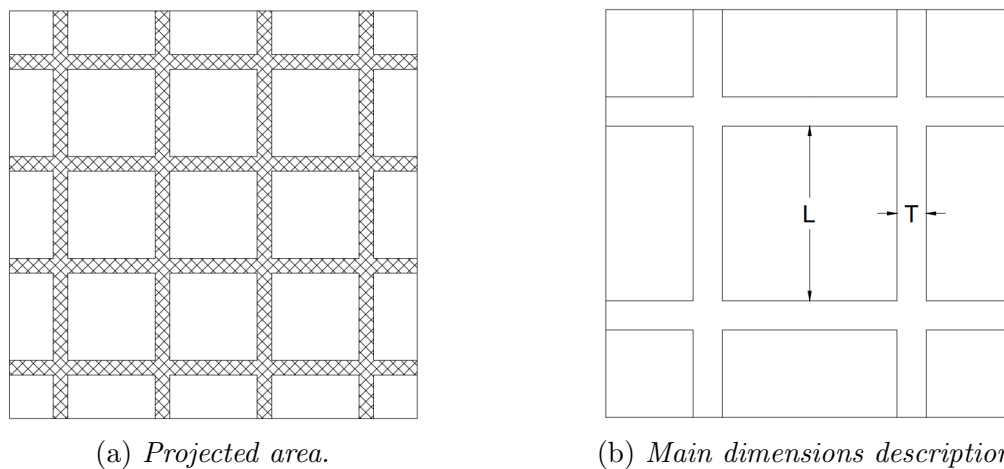
Figure 3.4: *Square Mesh*

3.3.2 Hexagonal Mesh

The primary dimensions for each of the hexagonal meshes that were modelled are displayed in Table 3.2.

Item	A (mm)	B (mm)	C (mm)	O (°)	T (mm)	Net Area (mm²)	Frame Area (mm²)	S_n
15-2	15	7.51	7.51	120	2	960.39	4624	0.208
13-2	13	8.66	8.66	120	2	841.25	3600	0.234
17-3	17	9.82	9.82	120	3	1907.07	7056	0.270

Table 3.2: *Hexagonal Mesh main dimensions.*

Figure 3.5 depicts the projected area of the square mesh as well as a description of its primary parameters.
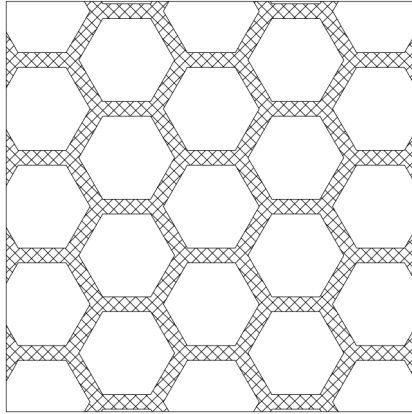
(a) *Projected area*
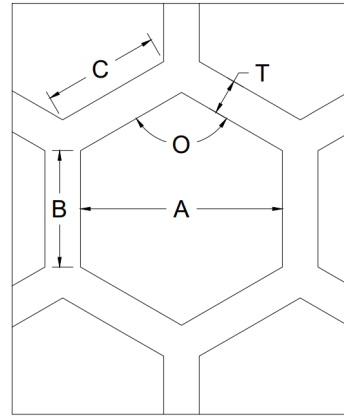
(b) *Main dimensions description.*

Figure 3.5: *Hexagonal Mesh*

Chapter 4

CFD Analysis

4.1 Validation of CFD Setup with Experimental Data

Aquaculture systems often employ flexible structures, such as nets, which exhibit a higher level of complexity compared to rigid bodies. These flexible structures possess inherent compliance that enables them to handle substantial loads by deforming and effectively mitigating both local stresses and overall burdens. Consequently, comprehending the behavior of such flexible structures across various sea load scenarios becomes crucial when determining their suitability for deployment [23].

Numerical models are crucial design tools for predicting the behavior and mechanical properties of net-based structures in specific sea conditions, enabling accurate deformation and stress predictions. However, in order to improve the accuracy of the results, these numerical techniques must be validated using experimental data.

The findings from hydrodynamic experiments conducted in 2019 on a knotted net panel, featuring a low solidity ratio and exposed to a uniform flow at acute angles, will serve as the basis for evaluating the Computational Fluid Dynamics (CFD) configuration for the current net panels developed in this research.

For these experiments, a net panel with a solidity ratio of 0.1046 was towed at nominal speeds ranging from 0.2 m/s to 1.0 m/s in 0.2 m/s steps, with angles of attack of 0°, 15°, 30°, and 45°, all at the previously specified velocities.

The trials were conducted at the Canal de Ensayos Hidrodinámicos de la Universidad Austral (CEH-UACh). The tank measures 45 meters in length, 3 meters in width, and 2 meters in depth, and it is equipped with a towing carriage (Figure 4.1).

The primary aim of this experiment was to ascertain the drag coefficient of the net panel. In pursuit of this objective, the net was systematically towed within a

Figure 4.1: *CEH-UACh Towing Tank.*

purpose-built frame, as visually depicted in Figure 4.2a. Additionally, Figure 4.2b provides comprehensive details regarding the principal dimensions of the twines and knots comprising the net, as well as the mesh size.

(a) *Net Panel.*
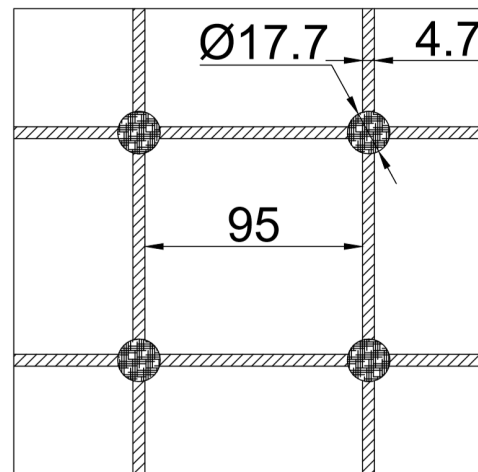
(b) *Main dimensions of the mesh.*

Figure 4.2: *Descriptive figures of the net used for the experimental test.*

To establish the validity of the CFD setup for the net panels, it is imperative to conduct a CFD simulation using the modeled experimental net (Figure 4.3). Subsequently, a thorough comparison between the simulation outcomes and the experimental data obtained from the conducted experiments must be performed. This evaluation will enable the assessment of the accuracy and suitability of the CFD setup for application to the net panels.

Although the experiments yielded results for different angles of attack, only the data obtained at a 0° angle will be used for the evaluation.
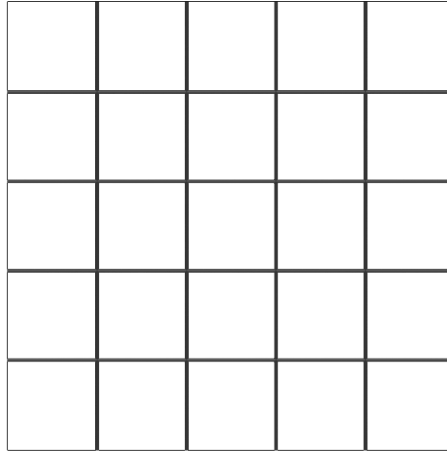
Figure 4.3: *Experimental Net Modeled.*

4.1.1 Pre-processing

The CFD simulations will be conducted using the Tdyn CFD+HT software [32], while the 3D modeling was performed utilizing the Rhinoceros software.

4.1.1.1 Domain and Subdomain Generation

Figure 4.4 shows the dimensions of the Domain and Subdomains generated in terms of the frame length (The selection of these dimensions was based on a specific recommendation provided by the professor advisor).

Figure 4.5 depicts a three-dimensional model showcasing both the net structure and the generated domain and subdomains, which are instrumental for conducting the CFD analysis.

4.1.1.2 Initial Conditions

The initial conditions define the starting state of the fluid flow simulation. They are necessary to initiate the flow and allow the CFD solver to compute the subsequent flow field. Without proper initial conditions, the simulation may fail to converge or provide inaccurate results. Overall, they have a profound influence on the accuracy, stability, and convergence of the results. Careful consideration and appropriate selection of initial conditions are essential for obtaining reliable and meaningful insights from CFD analyses.

- Velocity Field
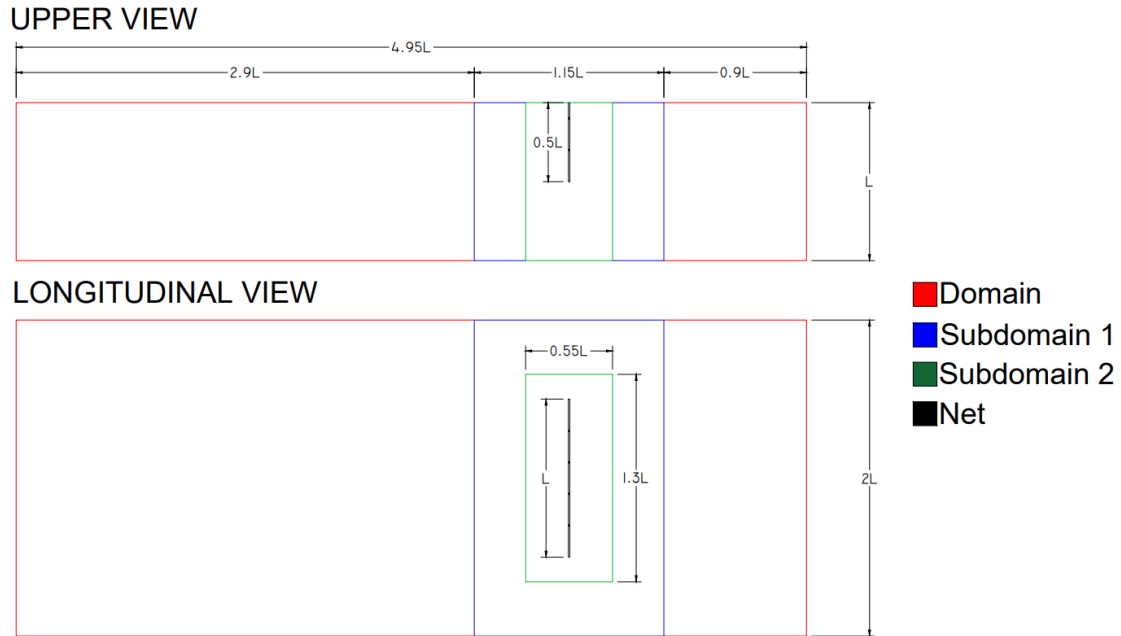
Figure 4.4: *Dimensions of the domain and subdomains in terms of frame length for CFD validation.*
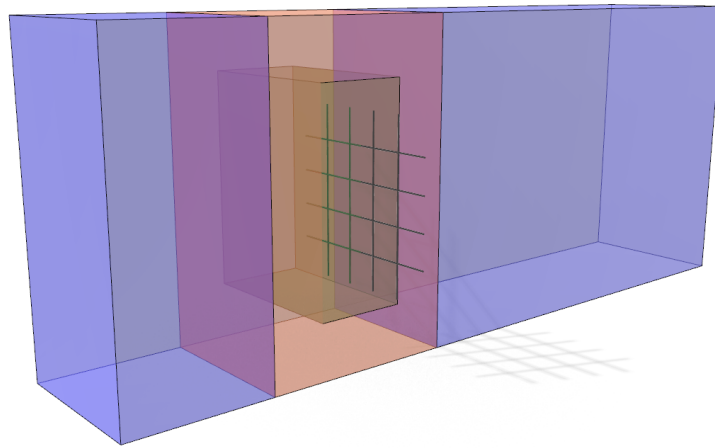
Figure 4.5: *Experimental 3D Model for CFD Validation.*

According to the data obtained from the selected buoy, velocities typically encountered at the site range from 0.35 to 0.65 m/s. Considering that the experiment encompassed a speed range of 0.2 to 1.0 m/s, with increments of 0.2 m/s, it was determined that input velocities of 0.2, 0.4, and 0.6 m/s in the x direction would be utilized.

- Turbulence Model and Parameters

Considering the limited turbulence expected within the simulation due to the range

of current speeds, the *Spalart-Allmaras* turbulence model was chosen for the purpose of this investigation [31]. The Spalart-Allmaras model is a one-equation model, which means it has a relatively simple formulation compared to more complex turbulence models like the Reynolds-averaged Navier-Stokes (RANS) models. Aquaculture nets are typically composed of porous materials that introduce anisotropic flow characteristics. The Spalart-Allmaras model has been found to handle the anisotropy of flows reasonably well, making it suitable for capturing the flow behavior around net structures accurately.

After establishing the Turbulence model, accurate simulation of turbulence in CFD models necessitates the incorporation of several parameters. Specifically, the initial turbulence intensity (TIL), eddy kinetic energy field (κ), and eddy length field (l) need to be defined. The values for these parameters were obtained from the equations documented in the *Tdyn CFD+HT Turbulence Handbook* [33]:

$$TIL = 0.16 Rn^{-\frac{1}{8}} \tag{4.1}$$

$$k = \frac{3}{2}(TIL \cdot V)^2 \tag{4.2}$$

$$l = \frac{v_r}{\rho\sqrt{k}} \tag{4.3}$$

Where,

- ν_r is the turbulent viscosity.

- Boundary Layer Thickness and Shear Stress at wall

Note: The formulation employed for the TIL is commonly applied for fluid flow within pipes. However, in the absence of a better approach, estimation or experimental data for this type of flow, the presented TIL formulation was used.

Given that the resulting Reynolds numbers fall within the laminar flow regime, the Blasius formula for boundary layer thickness will be employed [34]. The initial step involves establishing a specific point along the twine length as the assumed location of separation. Considering the twines' close resemblance to cylinders, a separation point at 50% of the perimeter of half of the twine will be considered.

$$R_{nx} = \frac{V \cdot x}{v} \tag{4.4}$$

Where,

- x denotes the specific location on the net's perimeter where boundary layer separation occurs [m].

- R_{nx} is the Reynolds number at the separation point.

$$\frac{\delta}{x} \cong \frac{5.0}{\sqrt{Rn_x}} \tag{4.5}$$

Where,

- δ is the Boundary layer thickness [m].

After determining the boundary layer thickness, the shear stress at the wall can be computed using the following formula [34]:

$$\tau_w = \frac{2\mu V}{\delta} \tag{4.6}$$

Table 4.1 summarizes the initial conditions input into the Experimental CFD setup.

Speed (m/s)	$\mathbf{R}_n$	$\mathbf{R}_{nx}$	δ (m)	τ_w (kg/(m·s²))	TIL (%)	κ (m²/s²)	l (m)
0.2	899.70	2525.742	0.00147	0.318	0.0684	0.00028	0.00070
0.4	2699.09	5051.483	0.00104	0.900	0.0596	0.0009	0.00040
0.6	2699.09	7577.225	0.00085	1.653	0.0596	0.0019	0.00027

Table 4.1: *Initial Conditions for Experimental CFD Validation.*

4.1.1.3   Meshing

The initial element size (in mm) is determined by considering a target value known as y^+. This dimensionless parameter serves as a measure of mesh quality in proximity to the wall, indicating the ratio between the distance of the first cell center from the wall (y) and the thickness of the cell's viscous sublayer (δ). The viscous sublayer represents the region near the wall where the flow is predominantly influenced by viscous effects [34]. Figure 4.6 illustrates a commonly employed plot used to evaluate the selection of y^+ based on other parameters.

The target y^+ value is typically determined based on the desired level of accuracy and the type of turbulence model employed in the simulation. Different turbulence models have different requirements for the y^+ value. For example, low-Reynolds-number turbulence models may require a smaller y^+ value compared to high-Reynolds-number models. Generally, aiming for a y^+ value of approximately 1 is commonly desired to achieve accurate results [34]. To determine the appropriate value, the following expressions need to be employed:

$$y = \frac{\mu \cdot y^+}{v_{fricc} \cdot \rho} \tag{4.7}$$

Where,

$$v_{fricc} = \sqrt{\frac{\tau_w}{v_r}} \tag{4.8}$$
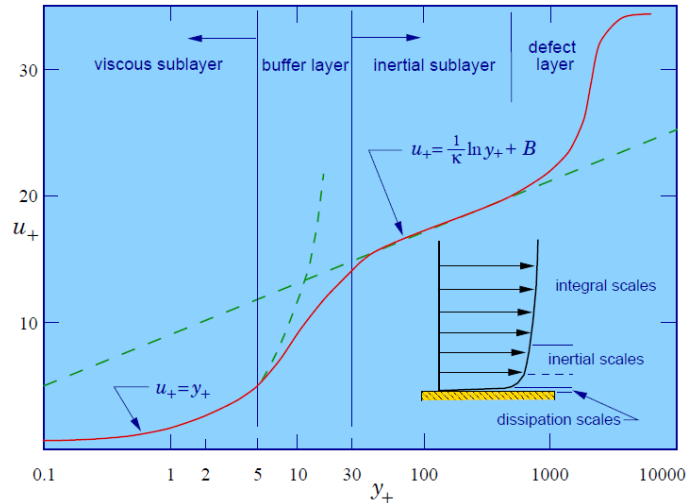
Figure 4.6: *Law of the Wall.*

Speed (m/s)	$\mathbf{V}_{fricc}$	$\mathbf{y}^+$	y (mm)
0.2	0.0178	15	0.983
0.4	0.0300	25	0.974
0.6	0.0407	34	0.977

Table 4.2: *First element size for Experimental CFD Validation.*

The first elements size and y^+ values for each speed can be found in Table 4.2.

Having determined the initial element size for each velocity, the subsequent task involved defining the dimensions of the domain and subdomains. For each velocity, a series of three distinct meshes were generated to examine convergence patterns at different sizes of the domain and subdomains. Although the sizes were selected randomly, they were chosen in such a way as to maintain a consistent ratio between the domain and subdomains. Additionally, the meshes varied significantly in terms of the number of elements employed. Table 4.3 presents the specific sizes of each mesh at a velocity of 0.4 m/s. (The remaining sets of meshes for each velocity, as well as the corresponding convergence results, can be found in Appendix: CFD Analysis Results.)

Mesh Convergence	Elements	Domain	Subdomain 1	Subdomain 2	Net
Mesh 1	292860	160	100	60	1
Mesh 2	972239	80	40	20	1
Mesh 3	1642091	70	30	15	1

Table 4.3: *Mesh number of elements for Experimental CFD Validation (0.4 m/s).*

As an illustrative example, Figure 4.7 depicts Mesh 3 corresponding to a velocity of 0.4 m/s.
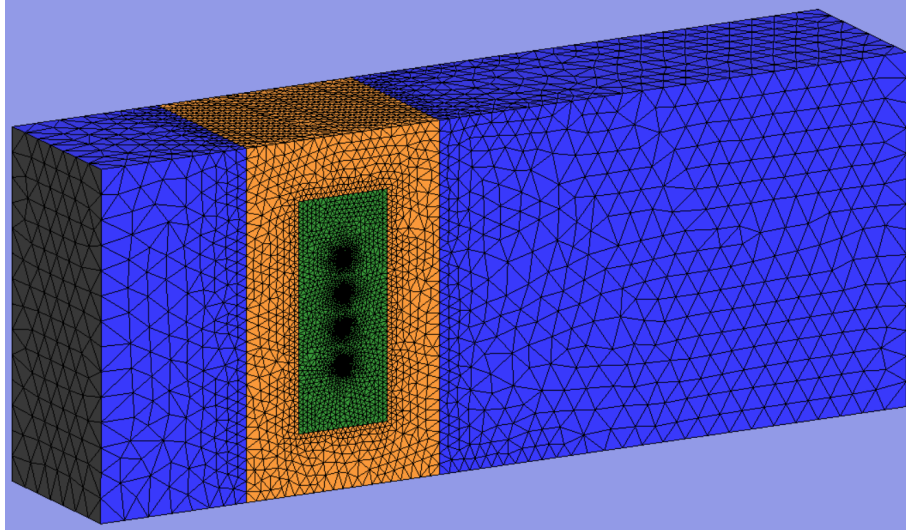
Figure 4.7: *Experimental CFD Validation - Mesh 3 (0.4 m/s).*

4.1.1.4   Boundary Conditions

The boundary conditions applied are listed as it follows,

- Outlet

- Velocity Field

    - Inlet

        * All directions constrained.

    - Symmetry Condition XZ Plane.

        * To enforce a symmetry condition, the Y direction was constrained as only half of the net was simulated.

        * Z direction

            · A Velocity Field condition with a constrained Z direction was imposed on the model.

- Fluid

    The selected fluid properties correspond to those employed during the hydrodynamic experiment conducted in the towing tank. The densities and viscosities values were obtained from *"ITTC - Fresh Water and Seawater Properties"* [35] based on the temperature of the water. These properties are as follows:

    - Fresh Water Temperature = 14 °C

    - Visc. μ (Pa·s) = 1.17E-03

    - Density (kg/m^3) = 999.247

$$- \nu = \mu/\rho \ (\text{m}^2/\text{s}) = 1.169\text{E-06}$$

- Wall Condition

  A y$^+$ wall was imposed over the net (Figure 4.8). The values applied for each simulation correspond to those specified in Table 4.2.
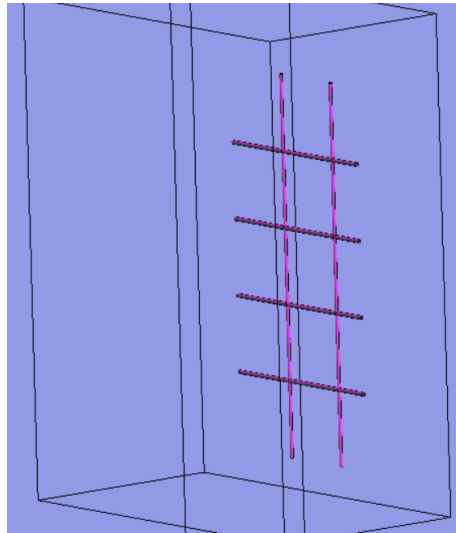
Figure 4.8: *y^+ Wall Boundary Condition.*

4.1.1.5   Timestep and Simulation Time

The timestep and the simulation time are both crucial factors that significantly impact the accuracy, stability, and efficiency of the simulation. Both of these can be calculated by the following equations:

$$Simulation \ Time \ (s) = \frac{Domain \ Length \ (m)}{Speed \ (m/s)} \tag{4.9}$$

$$Timestep \ (dt)\,(s) = \frac{dh \ (mm)}{Speed \ (m/s)} \tag{4.10}$$

Where,

- dh is the smallest element in the mesh.

Another important parameter that affects the stability and accuracy of the simulation is the Courant Number. The Courant Number is a dimensionless quantity used in numerical simulations which states that the timestep of a numerical simulation must be small enough to capture the propagation of information through the system [36]. In

the context of CFD, this means that the timestep must be small enough to ensure that disturbances or waves within the fluid do not travel a distance greater than the domain length during a single timestep. It is defined by the following expression:

$$Courant\ Number\ (C) = \frac{Speed \cdot Timestep}{Domain\ Length} \qquad (4.11)$$

In order to optimize computational efficiency, a Courant number of 1 was chosen.

Having determined the timestep and simulation time, the final step involves calculating the number of steps using the following expression:

$$Number\ of\ steps = \frac{Timestep}{Simulation\ Time} \qquad (4.12)$$

Table 4.4 summarizes the time data input into the Experimental CFD setup.

Speed (m/s)	Domain Length (m)	Simulation Time (s)	dh (mm)	dt (s)	nsteps
0.2	2.5	12.5000	1	0.0050	2500
0.4	2.5	6.2500	1	0.0025	2500
0.6	2.5	4.1667	1	0.0017	2500

Table 4.4: *Timestep and Simulation time for Experimental CFD Validation.*

4.1.2   Post-processing

After inputting all the necessary data into the software and running the simulations, the next step involves post-processing the results.

The simulation was stopped based on a specific criterion. The condition checked was whether the difference between the last calculated value during the process and the value obtained at approximately 70% of the simulation run fell within a range of 5 to 10%. To verify compliance with this criterion, the Pressure Force X plot was employed, and upon meeting the condition (pressure forces stabilized), the simulation was concluded.

Figure 4.9a presents the simulation for Mesh 3, running at a speed of 0.6 m/s, specifically at 2.601 seconds into the simulation. Figure 4.9b displays the calculation results from approximately 70% of the simulation (1.8207 seconds) up to 2.601 seconds. The error between the values obtained during this time range was approximately 0.06%, making it acceptable to conclude the simulation at that point. The same approach was employed for the rest of the simulations.

(a) *Complete Simulation Time.*

(b) *Time Range from 1.8207 to 2.601*
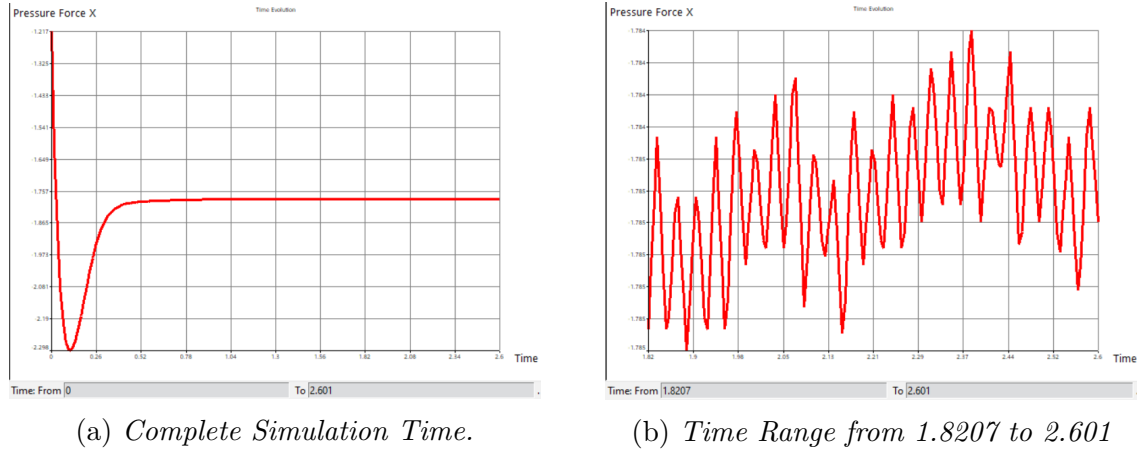
Figure 4.9: *Pressure Force X Graph for Experimental CFD Validation Mesh 3 (0.6 m/s).*

4.1.2.1 CFD Results and Mesh Convergence

The criteria employed to evaluate mesh convergence involved executing a minimum of three simulations and terminating the process when an error ranging from 10% to 5% was attained.

Table 4.5 presents the mesh convergence results for a velocity of 0.6 m/s, demonstrating that an error of 4.99% was attained. Thus, based on the adopted criteria, this value was deemed acceptable. (As previously mentioned, the convergence results and corresponding convergence charts for the remaining sets of meshes at each velocity can be found in Appendix: CFD Analysis Results).

Mesh Convergence	Elements	Drag Max (N)	ER%	Elements Difference
Mesh 1	292860	1.574		
Mesh 2	972239	1.874	16.01%	679379
Mesh 3	1641244	1.785	4.99%	669005

Table 4.5: *Mesh Convergence results for Experimental CFD Validation (0.6 m/s).*

Figure 4.10 displays the convergence chart from the results in Table 4.5 for a velocity of 0.6 m/s.

Figure 4.11a and Figure 4.11b depict the obtained CFD results illustrating the velocity field surrounding the net at a velocity of 0.6 m/s. Notably, in Figure 4.11a, higher velocities are observed compared to Figure 4.11b, indicating that at locations where the vertical and horizontal twines intersect, fluid velocity is diminished due to their interaction. Moreover, the horizontal twines exhibit relatively higher velocities. Regarding the wake field obtained, it is crucial to emphasize that the primary objective of the simulation is to derive drag results for subsequent comparison against experimental data. Thus, the obtained velocity mapping is considered sufficiently accurate
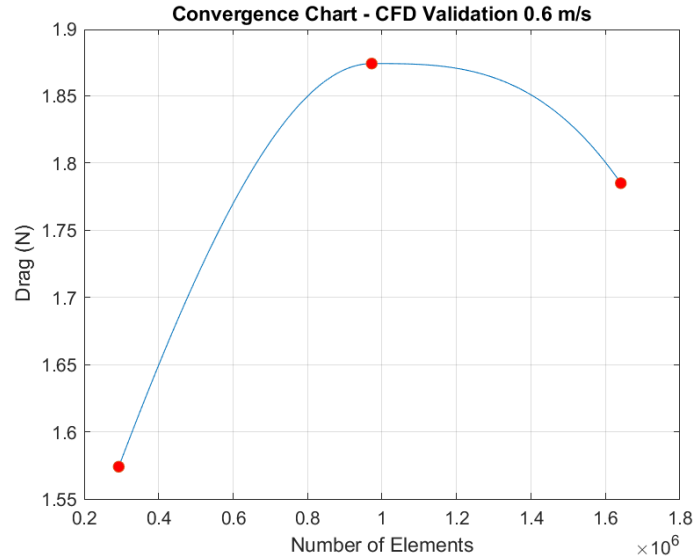
Figure 4.10: *Mesh Convergence Chart for Experimental CFD Validation (0.6 m/s).*

for this purpose.
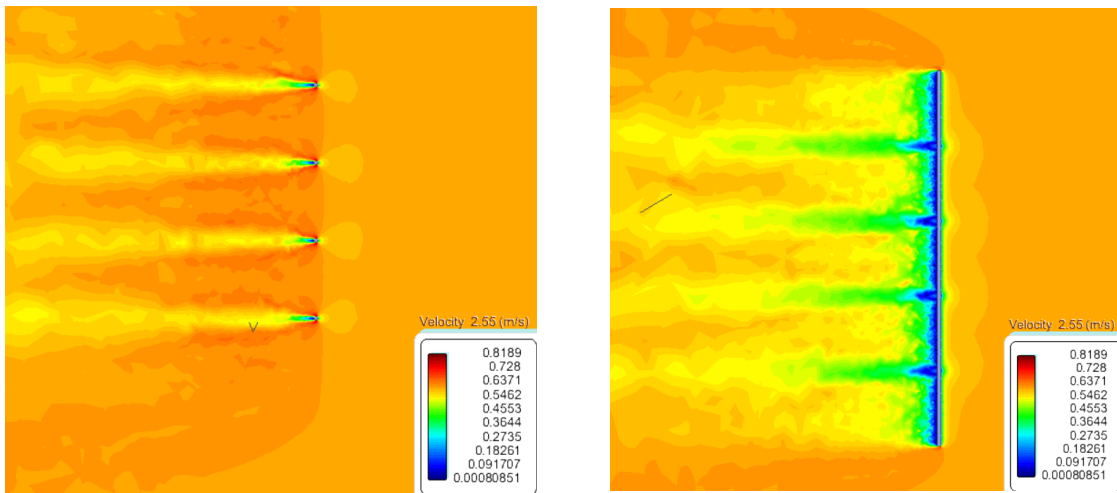
(a) *longitudinal cut on horizontal twines.*

(b) *longitudinal cut on vertical twines.*

Figure 4.11: *Velocity field results for Experimental CFD (0.6 m/s).*

Figure 4.12a and Figure 4.12b showcase the pressure results obtained for both faces of the net. It is notable that the lower pressure values on the back face of the net are primarily concentrated in the horizontal twines. This observation aligns with the previous expectation, as it was already mentioned that the fluid velocities would be higher in the horizontal twines. Conversely, the vertical twines exhibit comparatively higher pressure values.

These pressure distribution patterns offer valuable insights into the fluid dynamics surrounding the net, contributing to a deeper understanding of the net's performance

concerning drag and fluid interaction.
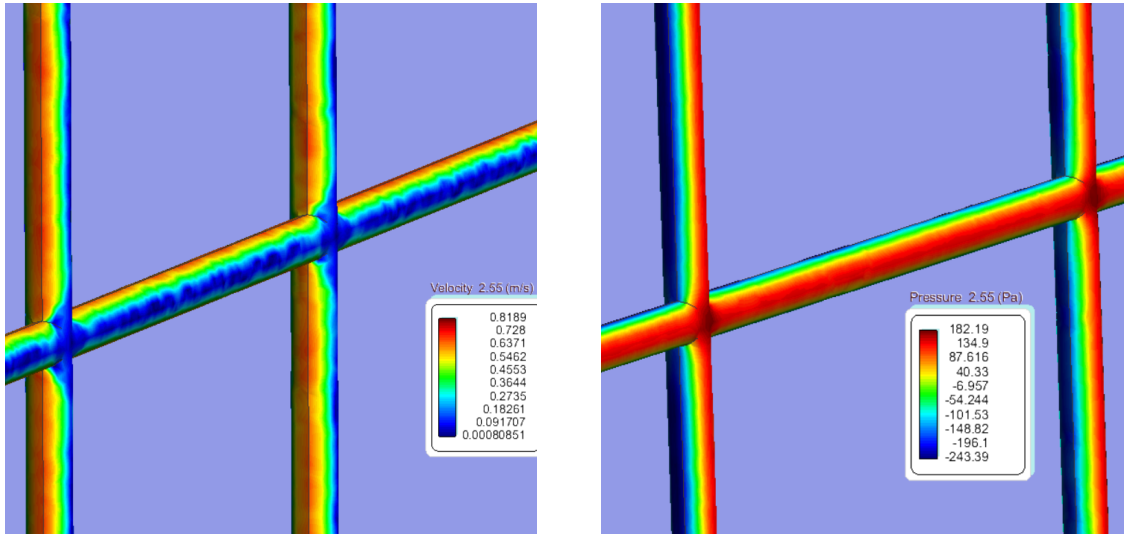
(a) *Back view (Velocity).*

(b) *Front view (Pressure).*

Figure 4.12: *Velocity and Pressure results over net for Experimental CFD.*

Figure 4.13a and Figure 4.13b depict the obtained CFD results illustrating the pressure field surrounding the net at a velocity of 0.6 m/s.
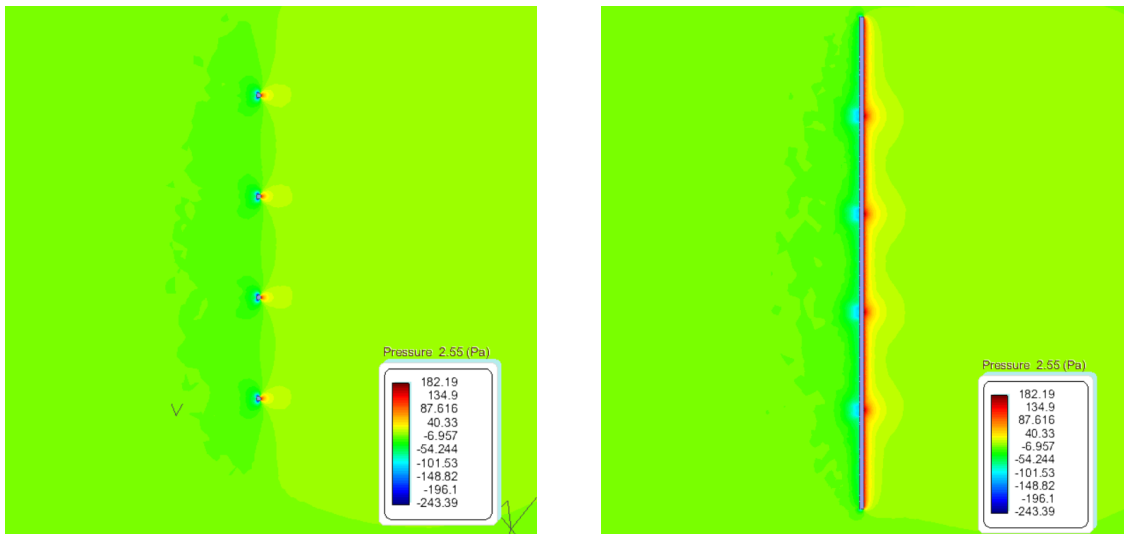
(a) *longitudinal cut on horizontal twines.*

(b) *longitudinal cut on vertical twines.*

Figure 4.13: *Pressure field results for Experimental CFD (0.6 m/s).*

Finally, the pressure and viscous force values in the X direction are extracted from the forces graphs to calculate the total drag. It is crucial to note that since only half of the net was simulated, the obtained forces must be multiplied by two. The total drag can be determined using the following expression,

$$D_{Total} = 2 \left(D_{pressure} + D_{viscous} \right) \tag{4.13}$$

Table 4.6 presents the obtained values for the total drag resulting from the CFD simulation.

Speed (m/s)	Drag CFD (N)
0.2	0.421
0.4	1.652
0.6	3.621

Table 4.6: *Experimental CFD Validation Drag results.*

4.1.2.2   CFD Validation with Experimental Data

Table 4.7 displays the drag results obtained from both the CFD simulations and the hydrodynamic experiments, along with the corresponding error values between the two datasets.

Speed (m/s)	CFD (N)	Experimental Data (N)	ER%
0.2	0.421	0.539	21.88%
0.4	1.652	1.822	9.31%
0.6	3.621	4.736	23.53%

Table 4.7: *Error Analysis of CFD Result vs. Measurement.*

Figure 4.14 showcases the comparative results between the CFD simulations and the experimental data. Despite the presence of relatively high errors between the results, it is notable that the curves exhibit a similar overall trend, except for the 0.6 m/s velocity case, where a more significant deviation in the curve shape is observed.

The reason for the high error between the experimental results and the simulation can be attributed to several factors. One significant factor is the presence of knots in the experimental net (Figure 4.2a), whereas the net modeled for the CFD simulation does not include knots (Figure 4.3). This simplification was adopted to facilitate the simulation process, as modeling the complex interaction between the knots and the twines would have been challenging.

It is important to note that the simulations were conducted using a rigid net, which means that no deformation caused by the fluid interacting with the net was considered. This decision was made to avoid higher computational costs that would have been incurred if such deformation were included, even though Tdyn CFD+HT is fully capable of performing it. Consequently, the simulations do not fully account for the real-world scenario where the net would likely experience deformation due to fluid interaction. This discrepancy could be one of the reasons for the observed differences between the results obtained from the CFD analysis and the experimental data.
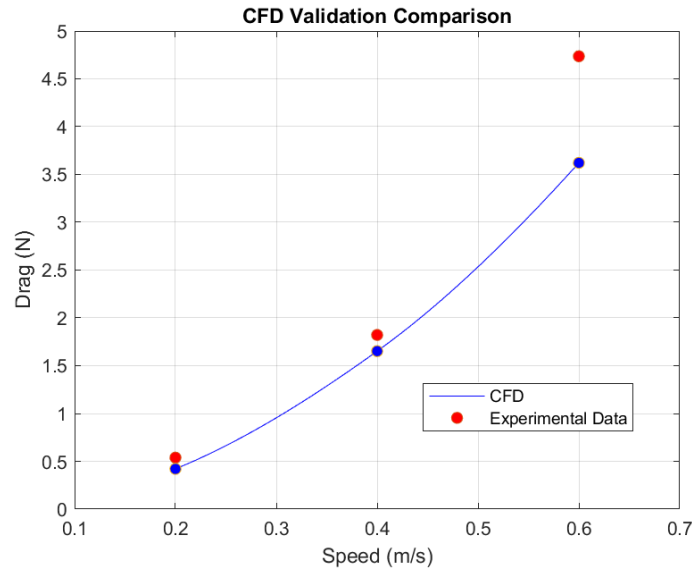
Figure 4.14: *Graphic representation of both CFD and Experimental Data.*

Another contributing factor is the presence of small sections of the net that extend beyond the frame. While these sections were not accounted for in the simulation, it should be noted that they do contribute to the overall resistance, although to a lesser degree. Additionally, the considerable error may be attributed to the deformation of the frame plates over numerous trials. These deformations could introduce additional resistance due to changes in shape, resulting in drag and potentially even lift effects.

Based on these arguments, it can be concluded that the comparison of the results is deemed acceptable. Consequently, the validation of the CFD setup is established in accordance with the experimental data.

4.2 CFD Setup of 3D Net Panels Modelled

Once the CFD setup has been validated through comparison with the experimental results, the next step involves applying the same procedures using the input values for the modeled net panels.

4.2.1 Pre-processing

4.2.1.1 Domain and Subdomain Generation

Figure 4.15 shows the dimensions of the Domain and Subdomains generated in terms of the frame length. After careful analysis of the experimental results, it was determined

that certain modifications to the dimensions were necessary in order to further optimize computational costs. These dimensions were applied to all the other net panels.
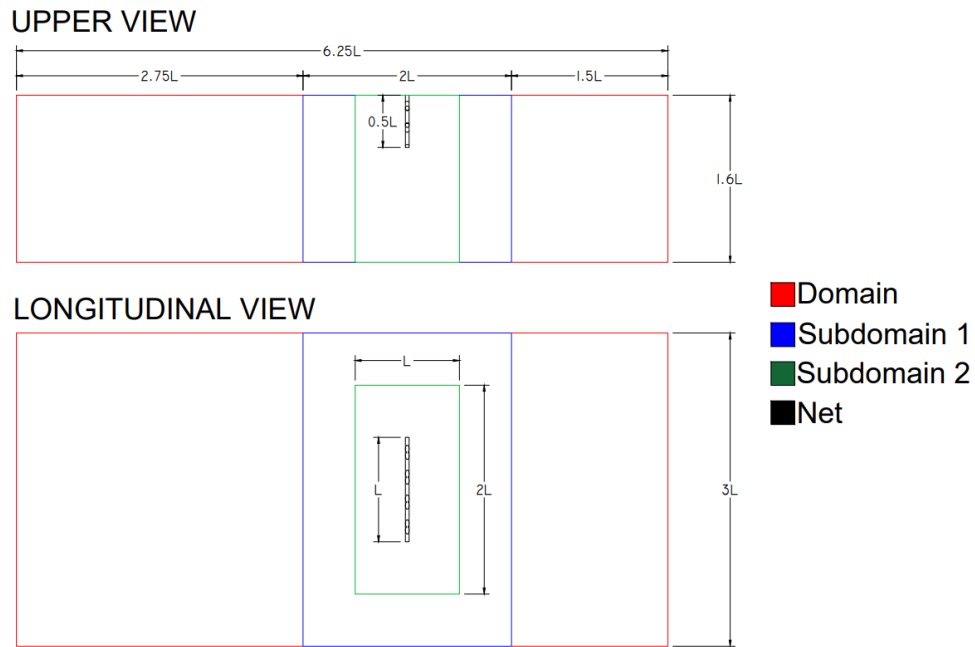
Figure 4.15: *Dimensions of the Domain and subdomains in terms of Frame Length for Net Panels.*

Figure 4.16 depicts a three-dimensional model showcasing both the net structure and the generated domain and subdomains for the Hexagonal 17-3 net panel, which are instrumental for conducting the CFD analysis.
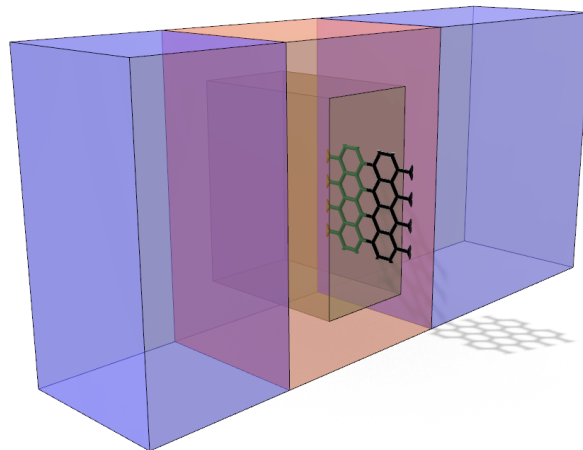
Figure 4.16: *Dimensions of the Domain and subdomains in terms of Frame Length for Net Panels.*

4.2.1.2   Initial Conditions

The identical initial conditions used in the CFD validation will be utilized for the simulations of the net panels, along with the same formulae. However, it should be noted that this time, the solidity ratios for each net panel will be considered, along with the selection of simulation speeds based on the current velocities obtained from the buoy data. Table 4.8 and Table 4.9 contain the initial conditions for set of square nets and hexagonal nets, respectively.

Net	Speed (m/s)	R_n	R_{nx}	δ (m)	τ_w (kg/(m·s^2))	TIL (%)	κ (m^2/s^2)	l (m)
	0.35	7.37E+02	900.907	0.000523	1.675	0.0701	0.00090	0.00041
Square 15-2	0.5	1.05E+03	1287.011	0.000438	2.859	0.0670	0.0017	0.00030
	0.65	1.37E+03	1673.114	0.000384	4.238	0.0649	0.0027	0.00024
	0.35	7.64E+02	900.907	0.000523	1.675	0.0698	0.00089	0.00041
Square 13-2	0.5	1.09E+03	1287.011	0.000438	2.859	0.0667	0.0017	0.00030
	0.65	1.42E+03	1673.114	0.000384	4.238	0.0646	0.0026	0.00024
	0.35	1.17E+03	1351.361	0.000641	1.367	0.0662	0.0008	0.00043
Square 17-3	0.5	1.67E+03	1930.516	0.000536	2.335	0.0633	0.0015	0.00031
	0.65	2.17E+03	2509.670	0.000470	3.461	0.0612	0.0024	0.00025

Table 4.8: *Initial Conditions for Square Nets CFD.*

Net	Speed (m/s)	R_n	R_{nx}	δ (m)	τ_w (kg/(m·s^2))	TIL (%)	κ (m^2/s^2)	l (m)
	0.35	7.24E+02	900.907	0.000523	1.675	0.0703	0.00091	0.00040
Hexagonal 15-2	0.5	1.03E+03	1287.011	0.000438	2.859	0.0672	0.0017	0.00030
	0.65	1.34E+03	1673.114	0.000384	4.238	0.0650	0.0027	0.00024
	0.35	7.48E+02	900.907	0.000523	1.675	0.0700	0.00090	0.00041
Hexagonal 13-2	0.5	1.07E+03	1287.011	0.000438	2.859	0.0669	0.0017	0.00030
	0.65	1.39E+03	1673.114	0.000384	4.238	0.0648	0.0027	0.00024
	0.35	1.18E+03	1351.361	0.000641	1.367	0.0661	0.0008	0.00043
Hexagonal 17-3	0.5	1.68E+03	1930.516	0.000536	2.335	0.0632	0.0015	0.00032
	0.65	2.19E+03	2509.670	0.000470	3.461	0.0612	0.0024	0.00025

Table 4.9: *Initial Conditions for Hexagonal Nets CFD.*

4.2.1.3   Meshing

The identical formulas and criteria employed in the CFD validation for determining the size of the first mesh element were subsequently applied to size the meshes of each net panel. Table 4.10 presents the first element sizes and corresponding y$^+$ values for each speed in relation to the square nets, while Table 4.11 provides the corresponding values for the hexagonal nets.

Similar to the approach adopted for the mesh convergence of the CFD validation, three sets of meshes were generated for each speed pertaining to every net panel. Appendix: CFD Analysis Results contains these meshes and their respective convergence results. As an illustrative example, Figure 4.17 depicts Hexagonal Net 17-3 Mesh 3 corresponding to a velocity of 0.65 m/s.

Net	Speed (m/s)	V_{fricc}	y^+	y (mm)
Square 15-2	0.35	0.0404	12	0.362
	0.5	0.0528	16	0.370
	0.65	0.0643	19	0.361
Square 13-2	0.35	0.0404	12	0.362
	0.5	0.0528	16	0.370
	0.65	0.0643	19	0.361
Square 17-3	0.35	0.0365	13	0.434
	0.5	0.0477	18	0.460
	0.65	0.0581	21	0.441

Table 4.10: *First element size for Square Nets CFD.*

Net	Speed (m/s)	V_{fricc}	y^+	y (mm)
Hexagonal 15-2	0.35	0.0404	12	0.362
	0.5	0.0528	16	0.370
	0.65	0.0643	19	0.361
Hexagonal 13-2	0.35	0.0404	12	0.362
	0.5	0.0528	16	0.370
	0.65	0.0643	19	0.361
Hexagonal 17-3	0.35	0.0365	13	0.434
	0.5	0.0477	18	0.460
	0.65	0.0581	21	0.441

Table 4.11: *First element size for Hexagonal Nets CFD.*
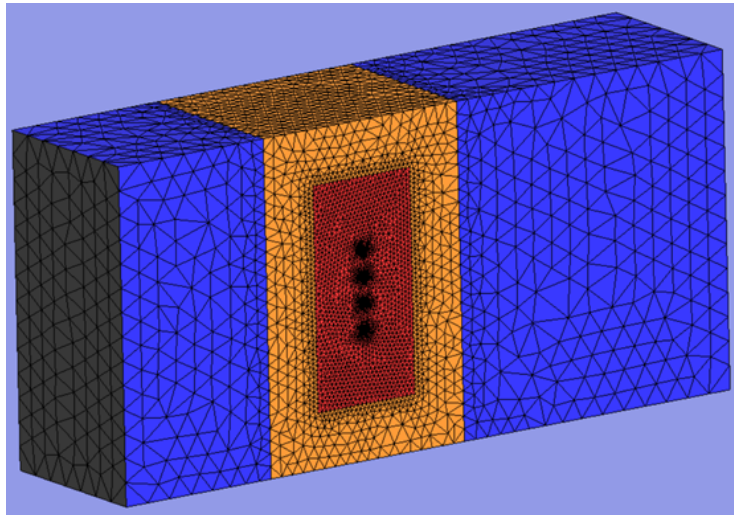
Figure 4.17: *Hexagonal Net 17-3 - Mesh 3.*

4.2.1.4 Boundary Conditions

The only variation in the boundary conditions is the fluid type, as the offshore structure is located in the sea. The densities and viscosities values were obtained from "*ITTC - Fresh Water and Seawater Properties*" [35] based on the temperature of the water. These properties are as follows:

- Seawater Temperature = 14 °C (This value was determined based on the data buoy).

- Visc. μ (Pa·s) = 1.252E-03

- Density (kg/m^3) = 1026.236

- $\nu = \mu/\rho$ (m^2/s) = 1.22E-06

4.2.1.5 Timestep and Simulation Time

The identical formulas and criteria employed for determining the time data in the CFD validation were subsequently applied to each speed of every net panel. Table 4.12 presents the time data corresponding to each speed for square and hexagonal nets 15-2 (the timestep and simulation time for the rest can be found in Appendix: CFD Analysis Results).

Speed (m/s)	Domain Length (m)	Simulation Time (s)	dh (mm)	dt (s)	nsteps
0.35	0.425	1.2143	0.37	0.0011	1500
0.5	0.425	0.8500	0.37	0.0007	1500
0.65	0.425	0.6538	0.37	0.0006	1500

Table 4.12: *Timestep and Simulation time for Square and Hexagonal Nets 15-2.*

4.2.2 Post-processing

After inputting all the necessary data into the software and running the simulations, the next step involves post-processing the results.

4.2.2.1 CFD Results and Mesh Convergence

Table 4.13 presents the mesh convergence results for a velocity of 0.65 m/s for Hexagonal Net Panel 15-2, demonstrating that an error of 0.56% was attained. Thus, based on the same adopted criteria from the CFD validation, this value was deemed acceptable. (As

previously mentioned, the convergence results and corresponding convergence charts for the remaining sets of meshes at each velocity for every net panel can be found in Appendix: CFD Analysis Results).

Mesh Convergence	Elements	Drag Max (N)	ER%	Elements Difference
Mesh 1	109899	0.08225		
Mesh 2	357403	0.09288	11.44%	247504
Mesh 3	832171	0.09236	0.56%	474768

Table 4.13: *Mesh convergence results for Hexagonal Net Panel 15-2 (0.65 m/s).*

Figure 4.18 displays the convergence chart from the results in Table 4.13 for a velocity of 0.6 m/s for Hexagonal Net Panel 15-2.
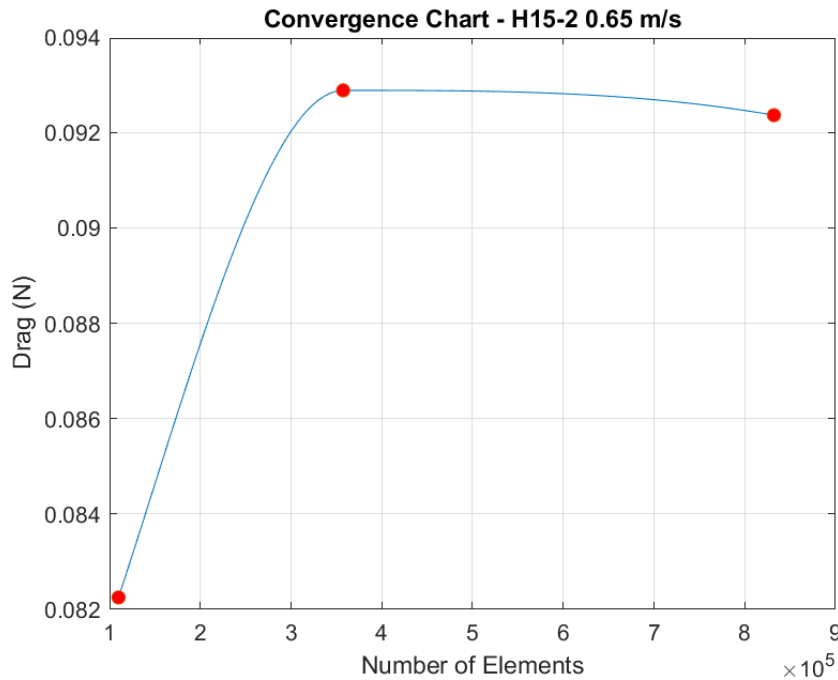
Figure 4.18: *Mesh Convergence Chart for Hexagonal Net Panel 15-2 (0.65 m/s).*

Figure 4.19a and Figure 4.19b depict the obtained CFD results illustrating the velocity field surrounding the Hexagonal Net Panel and the Square Net Panel 15-2, respectively, at a velocity of 0.5 m/s. Considering the observations made in the previous CFD validation results, a cut plane was strategically positioned at the midpoint of the horizontal twines, where the highest velocity values were observed. The resulting images clearly indicate that the net configuration directly influences the fluid velocity, as evident from the distinct velocity field mappings. In the Hexagonal Net Panel, lower velocity values are observed in the orange-colored zone, where boundary layer separation is expected to occur. Conversely, the Square Net Panel exhibits higher velocity values in the corresponding region.

Figure 4.20a and Figure 4.20b showcase the pressure results obtained for the same

(a) *Hexagonal Net Panel 15-2*   (b) *Square Net Panel 15-2*
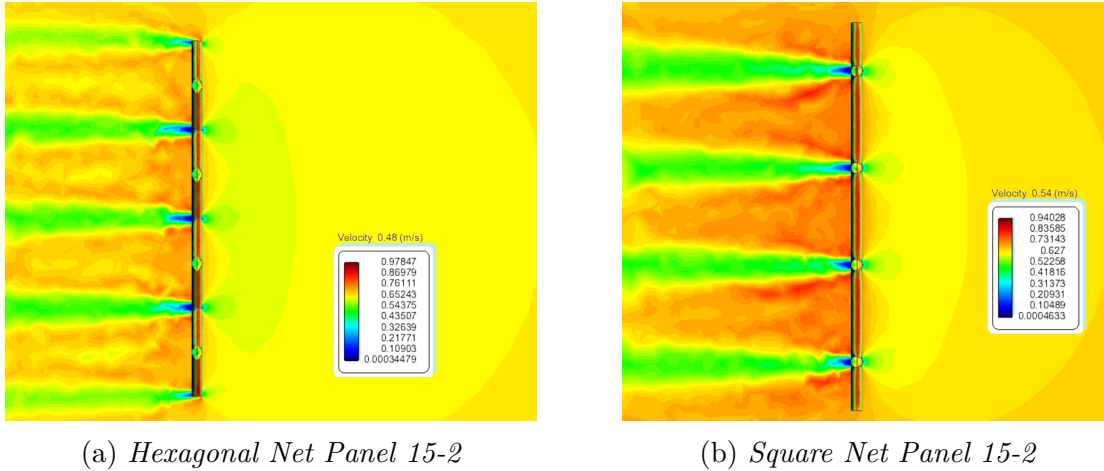
Figure 4.19: *Velocity field results for Net Panels (0.5 m/s).*

Net Panels that were examined in Figure 4.19. It can be observed that there is relatively little variation between the two Net Panels, with the exception of the minimum pressure values. The Hexagonal Panel exhibits a minimum pressure value of approximately -785.85 Pa, while the Square Net Panel yields a minimum pressure value of -376.53 Pa. This difference in pressure values suggests that the Hexagonal Net Panel, with its interconnected hexagonal mesh structure, may create more complex flow paths and generate different pressure gradients compared to the Square Net Panel.

(a) *Hexagonal Net Panel 15-2*   (b) *Square Net Panel 15-2*
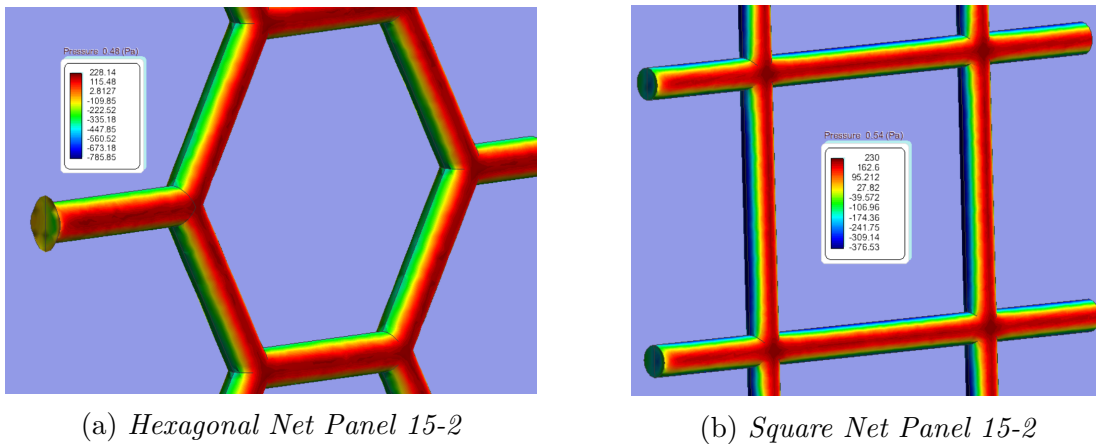
Figure 4.20: *Pressure results over Net Panels (0.5 m/s).*

Figure 4.21a and Figure 4.21b depict the obtained CFD results illustrating the pressure field surrounding the Hexagonal Net Panel and the Square Net Panel 15-2, respectively, at a velocity of 0.5 m/s.

Finally, the pressure and viscous force values in the X direction are extracted from the forces graphs to calculate the total drag. Subsequently, after determining the total drag, the drag coefficient needs to be computed. The drag coefficients for the Square Net Panels and Hexagonal Net Panel from the CFD simulations are provided in Table
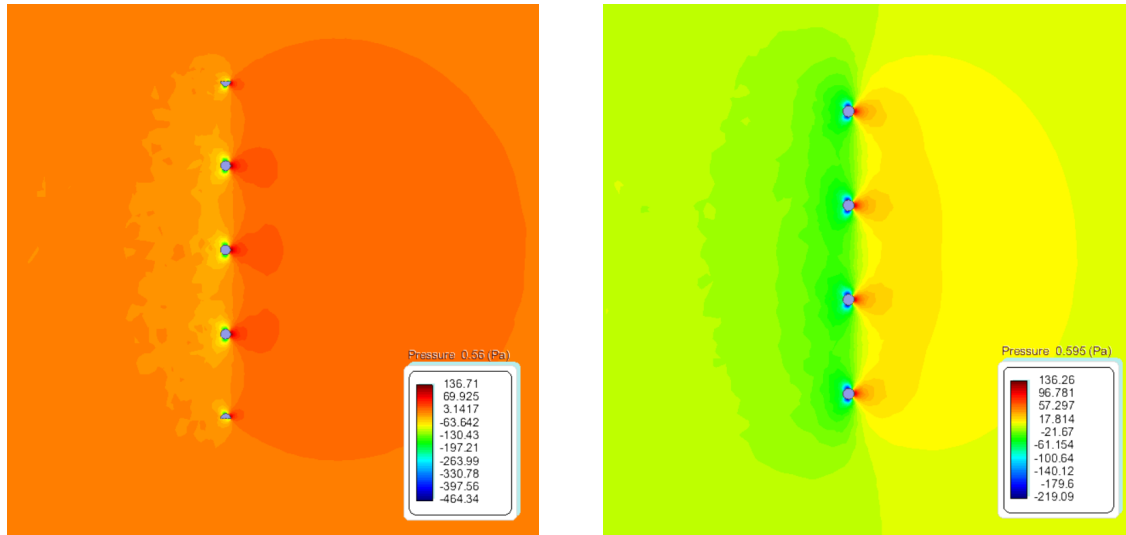
(a) *Hexagonal Net Panel 15-2*

(b) *Square Net Panel 15-2*

Figure 4.21: *Pressure field results for Net Panels (0.5 m/s).*

4.14 and Table 4.15, respectively.

Net	Speed (m/s)	Rn	Pressure Force (N)	Viscous Force (N)	Drag (N)	C_D
	0.35	7.37E+02	0.067	0.002	0.069	1.073
Square 15-2	0.5	1.05E+03	0.135	0.004	0.139	1.059
	0.65	1.37E+03	0.226	0.006	0.232	1.046
	0.35	7.64E+02	0.061	0.002	0.063	1.126
Square 13-2	0.5	1.09E+03	0.120	0.003	0.124	1.076
	0.65	1.42E+03	0.202	0.005	0.207	1.064
	0.35	1.17E+03	0.120	0.004	0.124	1.051
Square 17-3	0.5	1.67E+03	0.234	0.007	0.240	1.001
	0.65	2.17E+03	0.389	0.011	0.399	0.984

Table 4.14: *Square Net Panels CFD drag coefficient results.*

Net	Speed (m/s)	Rn	Pressure Force (N)	Viscous Force (N)	Drag (N)	C_D
	0.35	7.24E+02	0.058	0.002	0.060	0.991
Hexagonal 15-2	0.5	1.03E+03	0.110	0.004	0.113	0.920
	0.65	1.34E+03	0.185	0.006	0.190	0.914
	0.35	7.48E+02	0.056	0.002	0.058	1.092
Hexagonal 13-2	0.5	1.07E+03	0.109	0.003	0.113	1.043
	0.65	1.39E+03	0.183	0.005	0.188	1.031
	0.35	1.18E+03	0.122	0.004	1.367	1.055
Hexagonal 17-3	0.5	1.68E+03	0.239	0.007	2.335	1.007
	0.65	2.19E+03	0.398	0.011	3.461	0.989

Table 4.15: *Hexagonal Net Panels CFD drag coefficient results.*

4.2.2.2 Net Panels Comparison

Figure 4.22 presents the relationship between the drag coefficients and the speed for each modeled net panel.
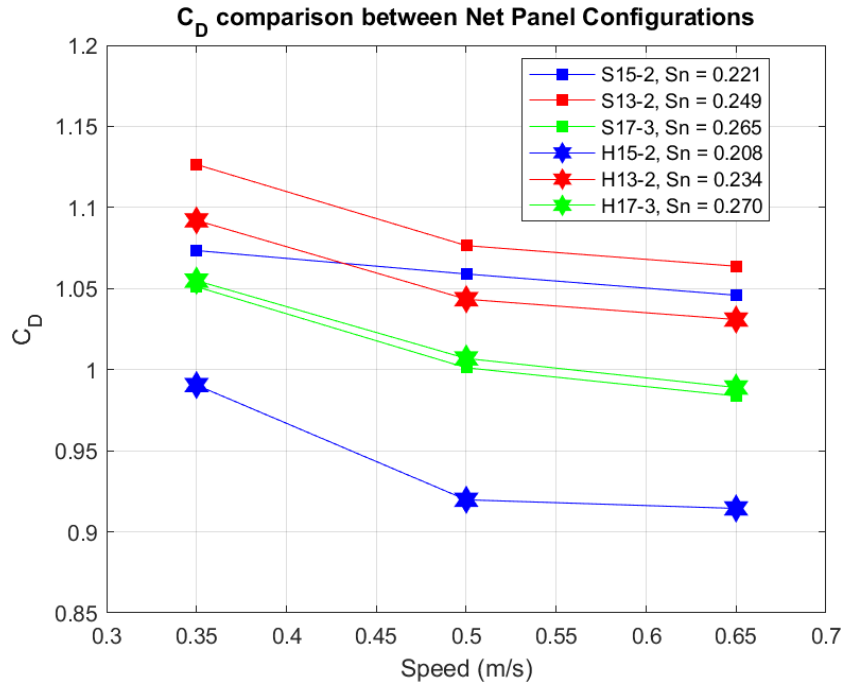
Figure 4.22: *Plot of drag coefficient vs. current velocity for different net types.*

Upon examining Figure 4.22, some key observations can be made. As anticipated from previous research, there is a clear inverse relationship between the speed and the drag coefficient. In other words, as the speed increases, the drag coefficient decreases. This trend aligns with the expectations and adds validity to the obtained results.

The relationship between the drag coefficient and the solidity ratio for a specific net panel configuration remains inconclusive. In both net panel configurations, the drag coefficient increases as the solidity ratio increases except for the last net panel for each configuration. Further investigation with a larger dataset is required to determine the precise behavior of the drag coefficient in relation to the solidity ratio. However, the primary objective of this study is to select the most suitable net panel configuration for the design of an offshore fish cage.

The key conclusion drawn from Figure 4.22 is that the drag coefficients of hexagonal configurations are lower than those of square configurations. This suggests that the hexagonal shape effectively reduces drag forces induced by water flow. The reduced drag can be attributed to the hexagonal net panels having fewer corners and edges, which in turn reduces the exposed surface area to water currents. This decrease in surface area leads to lower resistance, facilitating smoother water flow through the cage and reducing the load on the structure.

An additional disadvantage of a square mesh configuration is that, in a suspended square mesh net panel in a marine environment, the horizontal bars experience minimal tension and are prone to deformation. Conversely, the vertical bars bear the majority of the load due to gravitational forces, this creates semi-slack meshes that allow salmon smolt to potentially deform the horizontal bars and escape. Strong sea conditions and water currents further increase the slackness of the meshes, making them deformable in all directions. This higher slackness poses a greater risk of escape for salmon smolt as the mesh adjusts to their shape while they try to squeeze through [28].

Hexagons have inherent structural stability compared to squares. The triangular shape formed by the hexagonal netting creates stronger connections at the edges, which helps distribute forces more evenly. This can make the overall net panel more resistant to deformation and damage caused by water currents, waves, or fish activity within the cage.

However, it is worth mentioning that hexagonal net panels have higher costs and may be more challenging to obtain compared to square configurations, despite their numerous advantages.

After considering the options, it has been determined that the Hexagonal Panel 17-3 is the most suitable choice among the three hexagonal net panels. This decision is based on the fact that Hexagonal Panel 13-2 has a higher drag coefficient, and Hexagonal Panel 15-2 has a lower solidity ratio that could increase the risk of fish escapes.

Chapter 5

Fish Cage

5.1 Fish Cage Structure

Until this point, the selection of the offshore cage site has been completed, and an extensive study has been conducted to determine the optimal net panel type, resulting in the selection of the most suitable option. The subsequent step entails choosing a fish farming structure and estimating its weight and center of gravity based on the primary dimensions and structural arrangement. Following this, the conditions under which the fish cage will be examined will be defined, ultimately leading to the establishment of the design load cases.

5.1.1 Selection of Structural Type

There are two main types of fish farming cultures: cage culture and pen culture. Both involve confining organisms within an enclosed space while ensuring water circulation. However, they have distinct differences. Cage culture utilizes mesh or netting to enclose all or most sides of the structure, while pen culture relies on the natural lake or sea bed for the enclosure's bottom [37].

A net pen (Figure 5.1) consists of a framework made of floating materials, such as PVC pipes or metal, with a netting material attached to enclose the fish. The netting allows water to freely flow through, enabling natural exchange with the surrounding environment. These are typically located in nearshore or coastal areas, such as bays, fjords, or sheltered waters. They allow for relatively high water exchange due to the open-net structure. This allows natural water circulation, which can help maintain water quality, oxygen levels, and waste assimilation. However, it also means that there is a greater potential for environmental impacts as waste and nutrients disperse into the surrounding waters.
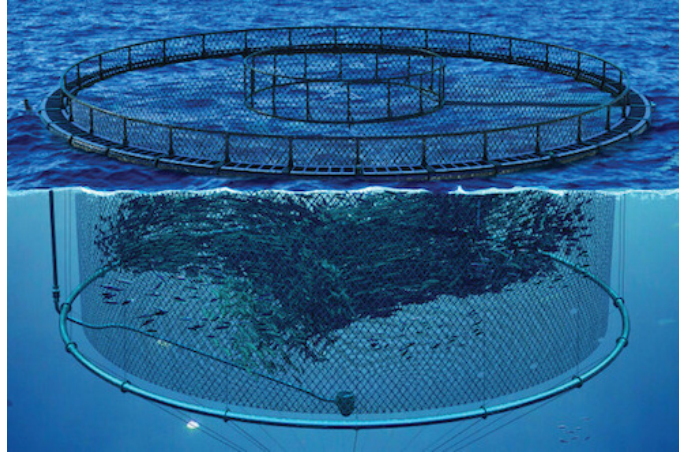
Figure 5.1: *Net-based cages.*

On the other hand, a sea cage, also known as offshore rigid structure or offshore fish farm, is a more solid and enclosed system compared to net pens. It typically consists of large, fixed or semi-submersible structures made of metal or concrete. The cages are placed within these structures, providing a more protected and contained environment for fish farming. They are is a more solid and enclosed system compared to net pens. It typically consists of large, fixed or semi-submersible structures made of metal or concrete. The cages are placed within these structures, providing a more protected and contained environment for fish farming. However, they have lower water exchange compared to net pens due to their more enclosed design, but they have the potential to reduce the environmental impact of fish farming compared to net pens. Figure 5.2 illustrates an offshore sea cage known as "Shenlan 1", which is China's inaugural deep-sea fish farming facility located in the Yellow Sea. This facility specializes in the breeding of Atlantic salmon and has the capacity to cultivate 300,000 salmon during a growth cycle [38].

Figure 5.2: *Offshore Rigid Structure - Shenlan.*

In the context of this project, the preferred option for the fish farming structure

is a fish cage. More specifically, the design of the Shenlan 1 has been selected. The decision is based on the fact that all of its main dimensions can be referenced from [39].

5.1.2 Main Characteristics

Utilizing the software Rhinoceros, a 3D model of the Shenlan fish cage was generated to aid in the project. Figure 5.3 showcases the primary dimensions of the cage in meters. The fish cage possesses an octagonal design and has a volumetric capacity of approximately 56,500 m^3.
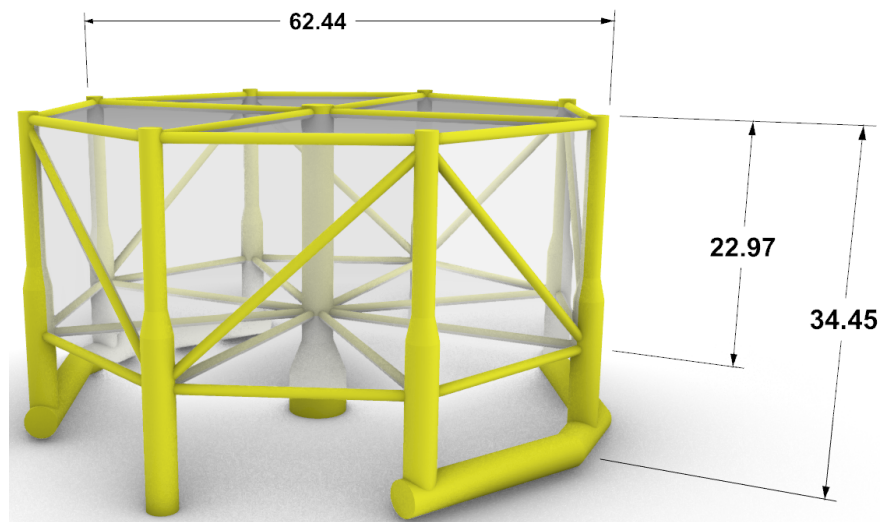
Figure 5.3: *Fish Cage Main dimensions.*

Regarding the structural arrangement, the principal elements primarily consist of columns positioned along the perimeter of the structure (Figure 5.4a). Additionally, there are outer and inner bracing components that facilitate the connection of all columns and ensure structural continuity (Figure 5.4b). It is worth noting that each column exhibits distinct zones, including a thicker (T), thinner (t), and conic (c) section. This distinction is important for assigning unique identifiers to each component, as indicated in Table 5.1. Apart from the central column, the outer columns have been divided into three different groups based on their lengths and the number of connected bracing elements. Similarly, the inner and outer bracing components have been categorized into upper and lower levels.

To enhance the structural stiffness, diagonal bracing elements (as shown in Figure 5.5) have been implemented. These bracings serve the purpose of providing additional resistance to the structure and increasing its load-bearing capacity.

Finally, the lower part of the structure features two tanks (as depicted in Figure 5.6) which serve dual purposes. Firstly, they contribute to the stability of the structure during transportation. Secondly, these tanks are utilized for ballasting the structure.

(a) *Columns.*

(b) *Outer and Inner Bracing.*
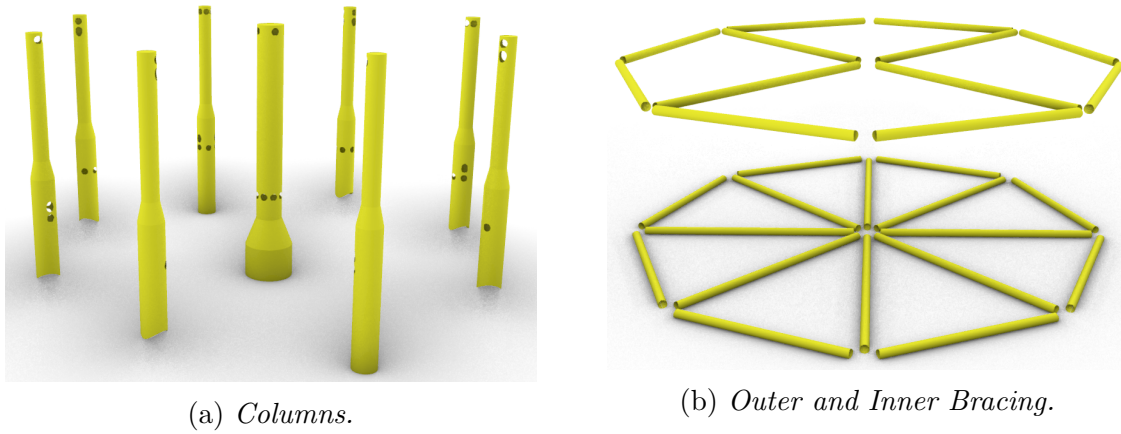
Figure 5.4: *Main Structure.*
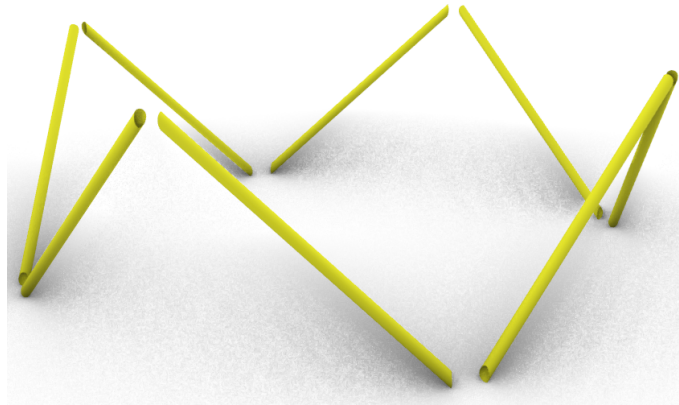
Figure 5.5: *Diagonally oriented Bracing.*

It is noteworthy, however, that the rest of the structural members can also be employed for ballasting purposes.
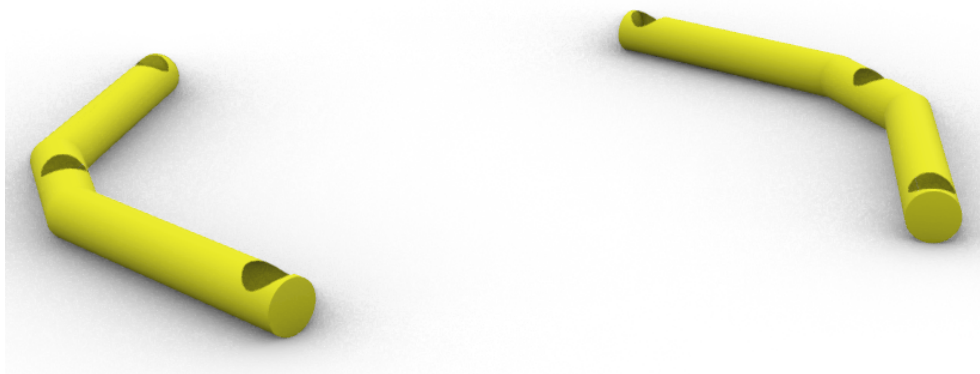
Figure 5.6: *Tanks.*

Table 5.1 summarizes the dimensions of the structural components associated with

the fish cage. As a preliminary design consideration based on [39], a thickness of 8 mm has been assigned for the entire structure. It is important to note that, although a detailed structural analysis is not the primary objective of this project, determining an appropriate thickness remains significant for obtaining the weight and center of gravity measurements.

Item	Unit	Length(m)	Diameter (m)	Area (m^2)	Thickness (mm)
Outer Column	**8**				
CO_T1_3	2	16.40	3.00	157.05	8
CO_T2_3	2	13.12	3.00	114.77	8
CO_T3_3	4	13.12	3.00	116.95	8
CO_t1_2	4	15.72	2.00	99.49	8
CO_t2_2	4	15.72	2.00	98.08	8
CO_c	8	2.36	3-2	18.72	8
Central Column	**1**				
CE_T_65	1	4.48	6.5	124.73	8
CE_t_35	1	3.77	3.5	288.12	8
CE_c	1	26.19	3.5-6.5	63.78	8
Outer Bracing	**16**				
UBO_1	8	21.40	1	66.79	8
LBO_1	8	21.40	1	66.79	8
Inner Bracing	**12**				
UBI_1	4	27.47	1	86.62	8
LBI_1	8	26.97	1	84.98	8
Diagonal Bracing	**8**	**29.07**	**1**	**88.91**	**8**
Float	**2**	**52.78**		**556.07**	**8**

Table 5.1: *Dimensions of Structural Arrangement.*

5.1.3 Material

The structural steel considered corresponds to high-strength ASTM A618 with a minimum yield strength of 345 MPa. This material was extracted from the specifications of API 2A-WSD [40]. The mechanical properties for the steel can be found in Table 5.2.

Mechanical Properties	
Yield Strength (MPa)	345
Young Modulus (MPa)	207000
Poisson Ratio	0.30
Tensile Strength (MPa)	485 MPa (min)
Density (Kg/m^3)	7850

Table 5.2: *ASTM A618 Steel Mechanical Properties.*

5.2   Net

In the previous chapter, a hexagonal net panel was selected, and its main dimensions were determined (Table 5.3). The following task involves selecting a suitable material for the net and extrapolating the size of the net. This extrapolation will be achieved by utilizing the solidity ratio to calculate the total surface area of the net. Furthermore, the weight and center of gravity of the complete net need to be calculated and taken into account for the overall design of the structure.

Net Choosen	
Shape	**Hexagonal**
$\mathbf{S}_n$	0.27
T (mm)	3
A (mm)	17
D (mm)	17
C (mm)	19.63
B (mm)	20

Table 5.3: *Net Panel Main Dimensions.*

Figure 5.7 is presented as a point of reference for comprehending the dimensions outlined in Table 5.3 regarding the net panel.
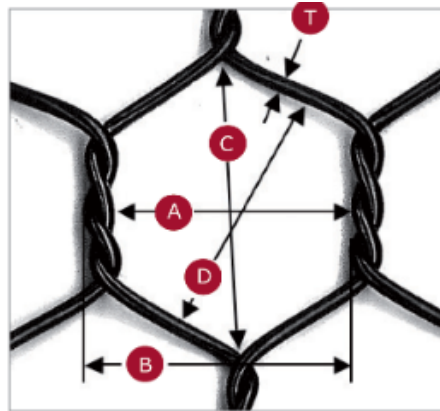
Figure 5.7: *Net Panel Main Dimensions Reference.*

5.2.1   Material

The selected material for the net is High-Performance Polyethylene (HPPE), which is highly suitable for a hexagonal mesh and has gained significant popularity in aquaculture, particularly for net production.

Among the advantages of this specific type of net material are as follows [40]:

- HPPE nets have good strength and at the same time are relatively low in weight.

- HPPE netting is more resistant than other fibres to fish bites, breaches and other damage.

- Since the net is rather stiff, the mesh size and opening keep generally retains its original shape allowing a good water flow through the net cage.

- HPPE net has twice the longevity of nylon nets.

Despite the numerous advantages offered by HPPE nets compared to traditional ones, it is worth noting that the cost of HPPE nets can be two to three times higher than that of traditional nylon nets.

Table 5.4 provides an overview of the mechanical properties associated to the selected HPPE net.

Mechanical Properties	
Density (kg/m^3)	950
Buoyance Factor	-0.08
Young's Modulus (MPa)	1000
Shear Modulus (MPa)	750
Tensile Strength (MPa)	26
Elongation (%)	590
Fatigue (MPa)	19
Bending Strength (MPa)	32.5
Hardness (Shore)	63.5

Table 5.4: *HPPE Net Mechanical Properties.*

5.2.2   Net Extrapolation

Once the net material and density are determined, it is necessary to calculate the total volume of the entire net to estimate its weight. To accomplish this, the net shall be extrapolated, taking into consideration its solidity ratio and the designated area it is expected to occupy within the fish cage.

Figure 5.8 illustrates the different areas occupied by the net, divided into upper, lower, and lateral zones. It should be noted that since the structure is octagonal, the total area of the lateral zones is eight times the value of a single zone.

Table 5.5 presents the findings regarding the total net area and volume. The areas of the net panels in each zone were directly obtained from the model's measurements. To calculate the volume, the thickness of the net material (as indicated in Table 5.3)

(a) *Upper Zone.*   (b) *Lateral Zone.*   (c) *Lower Zone.*
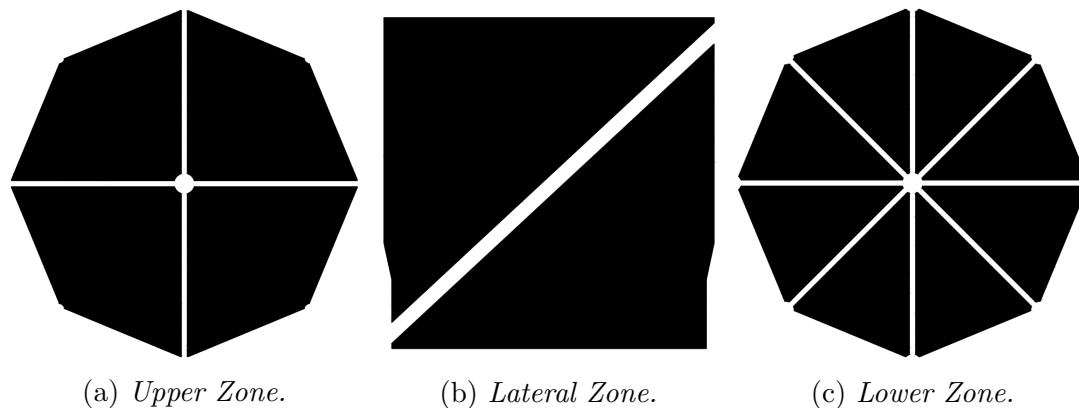
Figure 5.8: *Net panels assigned to each zone of the fish cage.*

was multiplied by the corresponding net area for each panel. However, it is important to note that assuming a square shape for the net section is incorrect. To address this, the resulting product of thickness and area was further adjusted by multiplying it with the ratio representing the proportion of space occupied by a circle within a square. This constant has an approximate value of 0.785.

Zone	Net Panel surface (m^2)	S_n	Net Area (m^2)	Volume (m^3)
Upper Zone	2369.00	0.27	639.63	1.507
Lower Zone	2255.31	0.27	608.93	1.435
Lateral Zone	3313.55	0.27	894.66	2.108
		Total	2143.22	5.050

Table 5.5: *Estimation of the total net area and volume.*

5.3   Weights and CG

In the seakeeping analysis, two conditions will be taken into account, requiring the assessment of the weights and centers of gravity associated with these conditions. The conditions under study include the transportation of the fish cage to the selected site and the operational condition.

5.3.1   Transport Condition

In the transport condition, the structure will not be ballasted. As a result, the total weight for this condition will be the sum of the dry weight of the structure and the net.

Table 5.6 presents the total weight and vertical center of gravity (Z_{cg}) for each structural member. Importantly, the reference point for the center of gravity is the

lowest point of the structure.

Item	Unit	Weight (Ton)	Total Weight (Ton)	Z_{cg} (m)	Moment-Z_{cg} (Ton-m)
Outer Column	8				
CO_T1_3	2	9.86	19.73	7.71	152.16
CO_T2_3	2	7.21	14.42	9.98	143.85
CO_T3_3	4	7.34	29.38	10.03	294.78
CO_t1_2	4	6.25	24.99	26.66	666.38
CO_t2_2	4	6.16	24.64	26.60	655.32
CO_c	8	1.18	9.40	17.49	164.42
Central Column	1				
CE_T_65	1	7.83	7.83	1.65	12.89
CE_t_35	1	18.09	18.09	21.87	395.75
CE_c_1	1	4.01	4.01	6.18	24.76
Outer Bracing	16				
UBO_1	8	4.19	33.56	33.64	1128.92
LBO_1	8	4.19	33.56	11.48	385.35
Internal Bracing	12				
UBI_1	4	5.44	21.76	33.64	732.02
LBI_1	8	5.34	42.69	11.48	490.25
Diagonal Bracing	8	5.584	44.67	22.57	1008.34
Floater	2	34.92	69.84	2.31	161.29
Net	3	4.7974	4.7974	22.67	108.74
		Total (Ton)	403.36	**Total (Ton-m)**	6525.21
		Final Z_{cg} (m)	16.18		

Table 5.6: *Total Weight and final Z_{cg} for Transport Condition.*

After calculating the lightweight of the structure based on the weights of each structural member, the displaced volume can be easily determined using Archimedes' principle. Considering only the weight of the structure and the buoyant force, the obtained volume is 393.05 m^3.

Using the calculated displaced volume as a guide, several iterations were performed on the 3D model of the fish cage. The draft was varied and the volume was calculated for each iteration until a match was found with the previously obtained result. Ultimately, a draft of 1.849 m was determined for the corresponding calculated volume. Figure 5.9 provides a point of reference for both the draft associated with the transport condition and Z_{cg} of the structure.

5.3.1.1 Radius of Gyration

In the seakeeping analysis, one of the key parameters to consider is the body data, which comprises the weight, center of gravity, and radius of gyration of the structure. To determine the radius of gyration, a tool from the Tdyn RamSeries software [41] can be employed. This tool enables the calculation of the radius of gyration by configuring the load case within the structure's properties. By utilizing this approach, accurate assessment of the structure's dynamic response and rotational behavior during seakeeping simulations can be achieved. To commence, the structure was input into RamSeries,
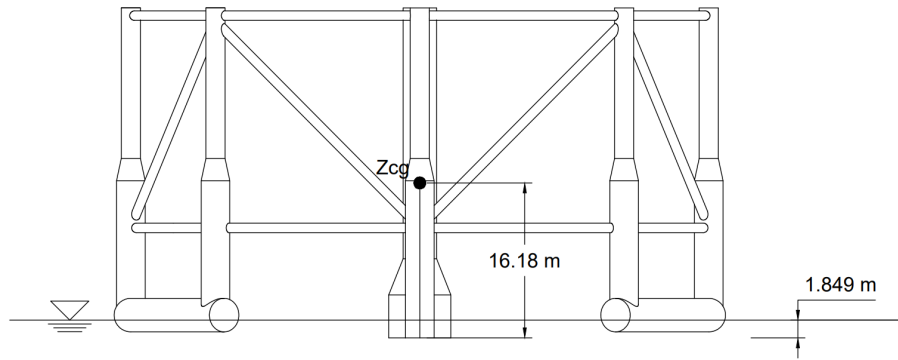
Figure 5.9: *Reference values for the Zcg and draft measurements pertaining to the transport condition.*

wherein a fixed constraint was applied to the bottom. Moreover, the material and thickness of each structural member were specified within the software.

For modelling and considering the weight of the net for the calculation, a fictitious disk was generated at the height of the Z_{cg} of the net, as can be seen in Figure 5.10.
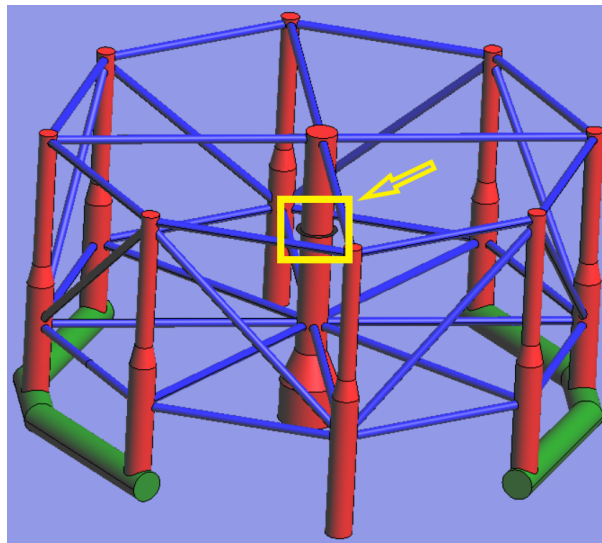
Figure 5.10: *Fictitious disk generated for modeling the net.*

The objective was to create a geometry with the same volume as the net. To achieve this, a disk was modeled with inner (d) and outer (D) diameters (see Table 5.7). The thickness of the disk was then calculated to ensure that the resulting cylinder had the same volume as the total net (shown in Table 5.5). Since the cylinder and the net possess identical volumes, their densities are also equal, resulting in equivalent masses. Thus, the specific gravity to be inputted into RamSeries should be the specific gravity of the net material.

Once all the aforementioned parameters were entered into RamSeries, a mesh with

d (m)	3.50
D (m)	4.50
V (m^3)	5.05
Thickness (m)	0.804
Density (Ton/m^3)	0.950
Specific Gravity (N/m^3)	9319.50

Table 5.7: *Main characteristics of the fictitious disk utilized for modeling the net.*

a size of 0.250 m was generated for the entire structure. Subsequently, the calculation was executed, resulting in the following values for the radius of gyration with respect to the orthogonal axes passing through the center of gravity,

- R_{xg} (m) = 20.9045

- R_{yg} (m) = 22.6605

- R_{zg} (m) = 26.5113

5.3.1.2 Stability Check

An initial stability check was performed, even though it was known that the structure has substantial inertia in both coordinate axes. However, it was considered important to assess its stability. For this purpose, the analysis was conducted using the Plug-In Orca3D with the Rhinoceros software. Table 5.8 presents the metacentric heights for small tilting angles, clearly indicating that the structure is highly stable. The obtained values are significantly greater than zero.

Static Stability Parameters			
I (m^4)	74781.93	I_L (m^4)	239688.44
BM_T (m)	191.16	BM_L (m)	612.70
GM_T (m)	190.56	GM_L (m)	612.10

Table 5.8: *Static Stability Parameters for Small Heel Angles.*

Moreover, Orca3D offers the option to generate the Righting Moment Curve, as illustrated in Figure 5.11. Apart from this, the wind force based on the wind speed for a Beaufort scale of 3 (10 knots) was calculated to estimate the righting force acting on the structure during transport conditions. The calculation employed the formula used for drag force, with consideration for the air density (1.29 kg/m^3). Notably, a drag coefficient of 1.2 was assumed, given its common application to cylindrical shapes, simplifying the overall calculation. It was further presumed that all parts of the structure and net share the shape of a cylinder.

To calculate the projected surface area of the structure, the wind direction (based on the Data Buoy) was initially considered, followed by estimating the surface area affected by the wind using the 3D Model. Subsequently, the heeling moment was computed based on the wind force and the distance from the Z_{cg} to the top part of the structure (32.6 m). The resulting heeling moment was then plotted alongside the righting moment in Figure 5.11, demonstrating the structure's evident capability to withstand the heeling moment produced by the wind force without any risk.
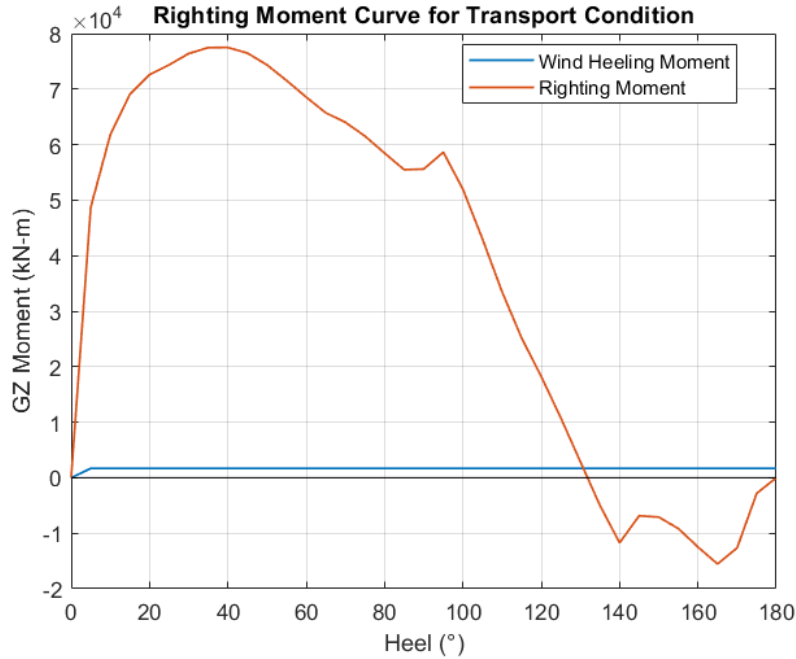
Figure 5.11: *Righting and Heeling Moment Curve for Transport Condition.*

5.3.2   Operational Condition

In the operational condition, a draft of 30 m was chosen. Unlike the transport condition, the methodology was approached in reverse since the draft value was already known. Based on the imposed draft for the operational condition, the total volume of the structure was obtained from the model. Next, the necessary ballast weight was calculated to achieve the desired draft. For this calculation, the following weights were taken into account,

- Buoyant Force (B)

- Ballast (W_b)

- Lightweight of the Cage (W_c)

- Mooring (W_m)

After conducting iterations, a mooring system comprising eight lines, each measuring 298.1 meters in length and weighing 107 kg/m, was chosen. As a result, the total weight of the mooring system is 255.17 tons. Further details regarding this selection will be covered in the seakeeping chapter. However, it is important to note the total weight of the mooring system for now.

- Net Buoyancy (B_n)

Considering that a significant portion of the net will be submerged underwater and given that the density of the net is lower than that of seawater, the net will experience a buoyancy force. This force can be determined by multiplying the buoyancy factor (as provided in Table 5.4) with the weight of the submerged section of the net. The weight of the underwater portion can be calculated by evaluating the net volume from the model, considering the draft condition.

The calculated net volume, representing the submerged portion, amounts to 3.22 m^3. By considering the density of the net material and applying the buoyancy factor, the resultant buoyant force contributed by the net is determined to be 2.40 N.

Archimedes' principle was employed to determine the volume of ballast, as demonstrated by the following equations,

$$B_n + B = W_c + W_b + W_m \tag{5.1}$$

$$B_n + \rho_w \cdot V_{disp} \cdot g = W_c + \rho_w \cdot V_b \cdot g + W_m \tag{5.2}$$

Where,

- $V_{disp} = V_{draft=30m} + V_{net\ draft=30} + V_{net\ fouling}$

- $V_{draft=30m} = 3005.60$ m^3

- $V_{net\ draft=30} = 3.22$ m^3

- $V_{net\ fouling} = 2.525$ m^3 . A fouling factor of 50% was taken into account when calculating the total weight of the net, as previously defined in Chapter 3.

Finally,
$$V_b = \frac{B_n + \rho_w \cdot V_{disp} \cdot g - W_c - W_m}{\rho_w \cdot g} = 2364.78\ m^3 \tag{5.3}$$

Considering that the ballast water consists of seawater, the total weight of the ballast water is determined to be 2426.83 metric tons. This implies that when accounting for the weight of the structure, including the net, mooring system, lightweight components, and ballast, the overall weight reaches **2832.58 tons**.

Once the ballast volume was determined, a process of iteration was conducted, similar to that used for the transport condition, until a match was found between the volume obtained from Archimedes' principle and the volume of the Fish Cage. The resulting draft was then utilized to determine the point at which the ballast water would be needed to achieve the desired draft condition. Figure 5.12 provides a reference for ballast water required to fulfill the operational condition draft.
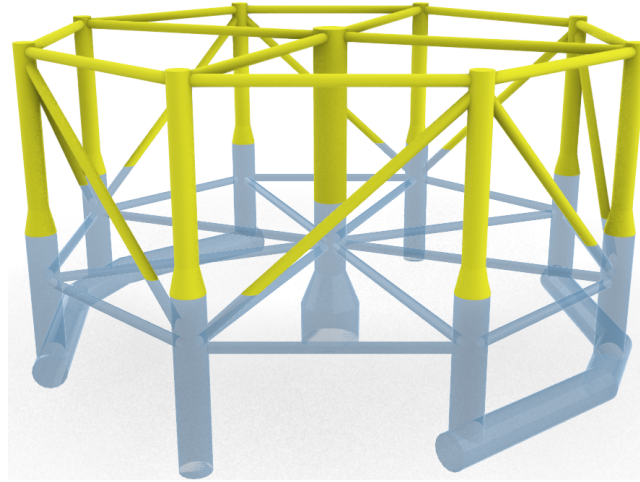
Figure 5.12: *Volume of Ballast Water for the structure reaching the operational condition.*

Using the 3D model, the ballast volume within each structural member and its corresponding center of gravity were easily determined. Table 5.9 presents the total weight and Z_{cg} for each ballasted structural member. To aid in identification, an additional row marked with a "B" has been added below the respective member.

To confirm the accuracy of the total weight presented in Table 5.9, a simple comparison was made with the weight obtained from Archimedes' principle calculation. This helped ensure the correctness of the calculated weight for the structure.

Figure 5.13 provides a point of reference for both the draft associated with the transport condition and Z_{cg} of the structure.

5.3.2.1   Radius of Gyration

The procedure employed to calculate the radius of gyration, which involved considering the net, was also applied to the ballast. However, in this particular instance, two disks were modeled (as depicted in Figure 5.14) to simplify the modelling. This approach facilitated the determination of the radius of gyration for the ballast component.

It is worth mentioning that when considering the weight change resulting from fouling, it is necessary to adjust the dimensions input in the software accordingly, so

Item	Unit	Volume (m^3)	Weight (Ton)	Total Weight (Ton)	Z$_{cg}$ (m)	Moment-Z$_{cg}$ (Ton-m)
Outer Column	8					
CO_T1_3	2		9.86	19.73	7.71	152.16
CO_T1_B	2	115.13	118.15	236.30	8.14	1924.34
CO_T2_3	2		7.21	14.42	9.98	143.85
CO_T2_B	2	87.24	89.53	179.06	10.11	1811.16
CO_T3_3	4		7.34	29.38	10.03	294.78
CO_T3_B	4	87.24	89.53	358.12	10.11	3622.31
CO_t1_2	4		6.25	24.99	26.66	666.38
CO_t2_2	4		6.16	24.64	26.60	655.32
CO_c	8		1.18	9.40	17.49	164.42
Central Column	1					
CE_T_65	1		7.83	7.83	1.65	12.89
CE_T_B	1	148.76	152.66	152.66	2.24	342.19
CE_t_35	1		18.09	18.09	21.87	395.75
CE_t_B	1	91.65	94.05	94.05	13.02	1224.45
CE_c	1		4.01	4.01	6.18	24.76
CE_c_B	1	76.31	78.31	78.31	6.00	470.09
Outer Bracing	16					
UBO_1	8		4.19	33.56	33.64	1128.92
LBO_1	8		4.19	33.56	11.48	385.35
LBO_B	8	15.84	16.26	130.07	11.48	1493.62
Inner Bracing	12					
UBI_1	4		5.44	21.76	33.64	732.02
LBI_1	8		5.34	42.69	11.48	490.25
LBI_B	8	21.21	21.77	174.16	11.48	1999.90
Diagonal Bracing	8		5.584	44.67	22.57	1008.34
BD_B	8	5.56	5.71	45.65	15.36	701.24
Floater	2		34.92	69.84	2.31	161.29
F_B	2	490.81	503.68	1007.37	2.38	2393.50
Net	3		4.7974	7.1960	22.67	163.11
			Total (Ton)	2832.59	**Total (Ton-m)**	22069.86
			Final Z$_{cg}$ (m)	7.79		

Table 5.9: *Total Weight and final Z$_{cg}$ for Operational Condition.*
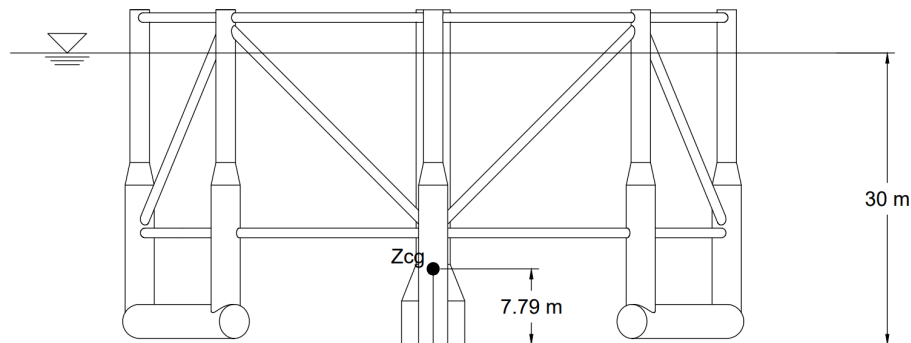
Figure 5.13: *Reference values for the Z$_{cg}$ and draft measurements pertaining to the operation condition.*

the final net volume can be achieved. Table 5.10 displays the values entered into the software for accurately modeling the Ballast and the net with fouling.

The following values for the radius of gyration with respect to the orthogonal axes passing through the center of gravity were obtained based on the inputs in the software,

- R$_{xg}$ (m) = 8.48744

	Ballast	Net
d(m)	3.00	3.50
D (m)	4.00	4.50
H (m)	1.00	1.21
V (m^3)	5.50	7.58
Densidad (Ton/m^3)	459.75	0.95
Specific Gravity (N/m^3)	4510159.54	9319.21
Specific Gravity per side (N/m^3)	2255079.77	-

Table 5.10: *Main characteristics of the fictitious disks utilized for modeling the net with fouling and the ballast.*
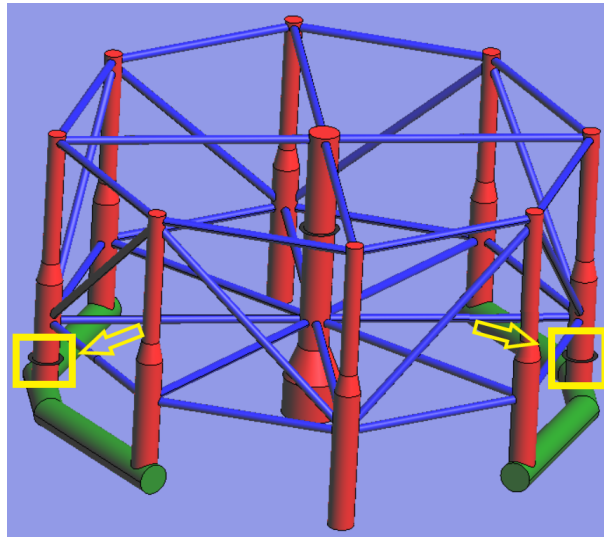

Figure 5.14: *Fictitious disks generated for modeling the ballast.*

- R_{yg} (m) = 29.4907

- R_{zg} (m) = 29.773

Chapter 6

Seakeeping Analysis

After carefully selecting the site, conducting a deep study of various types and sizes of nets, and finalizing the design and determination of total weight, draft, and center of gravity under different conditions, the concluding chapter of this project focuses on the investigation of the structure's seakeeping performance, involving all the aforementioned characteristics and conditions.

This chapter describes a seakeeping analysis, which involved defining design load cases and examining the motions of the fish cage. Additionally, a proposed mooring system was studied to enhance the seakeeping capabilities. The seakeeping analysis was performed utilizing the Tdyn SeaFEM software [42], a specialized tool for analyzing marine structures in dynamic sea conditions.

6.1   DLC

Design load cases (DLCs) help ensure the safety and structural integrity of the fish cage. By analyzing different load scenarios, it can be determine the maximum loads that the structure may experience during its lifespan and design it to withstand those loads. This minimizes the risk of structural failure, collapses, and accidents.

The fish cage will be examined in two different scenarios: one during its transportation from the shore to the desired location, and the other when it is in its operational draft. In compliance with the transportation scenario, it has been determined that the sea state classification shall be restricted to Beaufort 3 or below. It is essential to ensure that the structure is transported exclusively during sea conditions categorized as Beaufort 3 or less, while avoiding transportation in sea states exceeding Beaufort 3. This means that the maximum expected wave height during transportation would be around 3 feet (0.91 m) [43]. In the operational draft scenario, two cases will be taken into account: one for typical environmental conditions and another for extreme condi-

tions. The environmental conditions for the operational draft scenario were determined using the Weibull Distribution and Buoy Data discussed in Chapter 2.

Table 6.1 provides a summary of the environmental conditions for the three DLCs selected for simulation in the SeaFem software, specifically customized for the Fish Cage.

DLC	H_s (m)	T_m(s)	$V_{current}$ (m/s)
DLC I: Extreme Design	3.1	6.5	0.65
DLC II: Operational Condition	1.72	5.5	0.65
DLC III: Transport Condition	0.91	3.5	-

Table 6.1: *Combination of DLCs simulated.*

6.2   Mooring System

The mooring lines of a fish cage serve two important functions: to withstand and transmit forces. In order to fulfill these functions effectively, it is crucial for the mooring lines to possess certain characteristics. Since the loads imposed on a cage mooring system are usually dynamic, the mooring lines need to have a high breaking strength to withstand these forces. Additionally, they should be able to absorb and dissipate the kinetic energy generated by rapidly changing forces. These qualities ensure that the mooring lines contribute to the stability and durability of the fish cage, allowing it to withstand different environmental conditions and maintain its structural integrity [12].

In this study, a complete mooring system is developed for a fish cage array using link elements in SeaFem. To achieve this, it is necessary to define the seabed, mooring arrangement, and catenary material.

6.2.1   Seabed

The type of seabed in the ocean near Boston can vary depending on the specific location and depth. However, the general region around Boston is characterized by a mixture of sediment types, including sand, gravel, and clay, as can be seen in Figure 6.1.

The continental shelf off the coast of Massachusetts, which includes the area near Boston, tends to have a relatively flat seabed covered by a layer of sediments. Nearshore areas often have sandy or muddy bottoms, while offshore areas may have a greater presence of gravel or rocky substrate [44].

Based on the data found in the Massachusetts Office of Coastal Zone Management (CZM), it was decided to use mud/clay as the type of seabed for the SeaFem simulation.
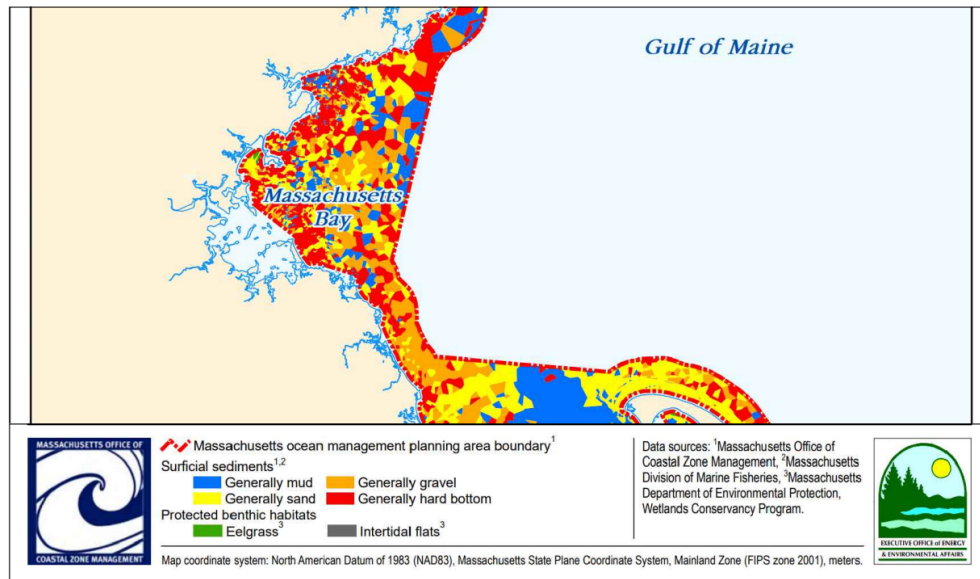
Figure 6.1: *Massachusetts Bay seabed sediment mapping provided by Massachusetts Office of Coastal Zone Management (CZM).*

6.2.2 Arrangement

The mooring system for the fish cage was built using link elements. Dr. José Gutierrez, in a personal communication, indicated that based on the environmental conditions at the specific sites, a catenary with a length of approximately 300 meters would be suitable.

Once the length of the catenary was determined, a proposed mooring system was developed, as shown in Figure 6.2.
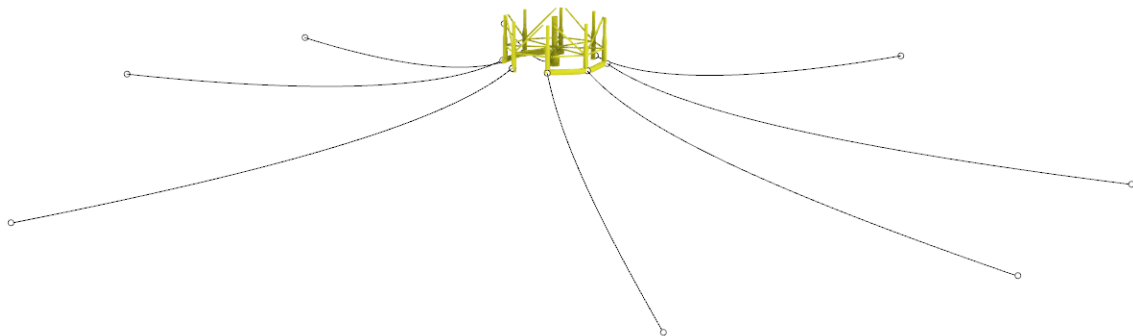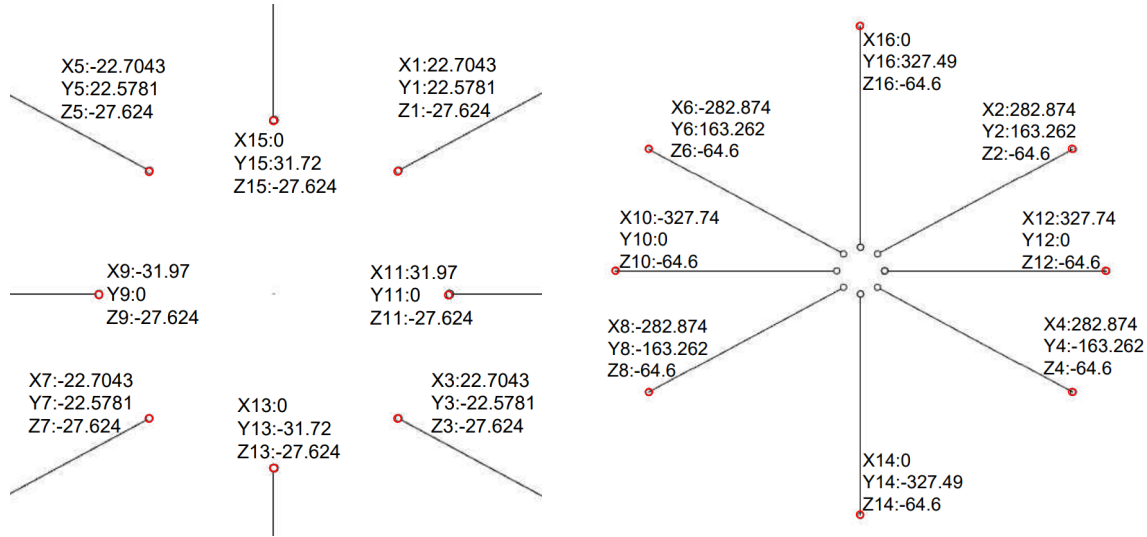

Figure 6.2: *3D Model of Mooring System proposed.*

Figure 6.3 provides the coordinates for each link element, including those attached to the fish cage and those moored to the seabed. The link elements connected to the fish cage were designated with the Fairlead point, while the ones anchored to the seafloor were equipped with an Anchor point along with a Chain.

(a) *Link Element Coordinates attached to the* (b) *Link Element Coordinates attached to the*
Fish Cage.   *Seabed.*

Figure 6.3: *Mooring System Link Coordinates.*

6.2.3 Catenary

Once a mooring system arrangement was proposed and the seabed of the site was investigated, the next step involved selecting the type of catenary to be used, along with its mechanical properties and weight. To make this decision, the team referred to the catalogue from Dai Han Anchor Chain [45], a renowned leader in chain manufacturing known for their exceptional quality and extensive knowledge of DNV and ABS requirements for mooring systems.

The initial choice for the mooring chain was a Stud Link Mooring Chain with a diameter of 54 mm and a weight of 64 kg/m. However, when the results of the first simulation under extreme conditions were obtained, it became evident that the chosen Mooring Chain would not be able to withstand the environmental loads. As a result, it was decided to make another iteration by modifying the dimensions to a mooring chain with a diameter of 70 mm and a weight of 107 kg/m. Table 6.2 provides the mechanical properties for the selected mooring chain, including the proof load (Yield Strength), which represents the maximum load or force that the mooring line or cable can withstand without suffering permanent deformation or damage.

Grade	Tensile Test			
	Yield Strength N/mm^2 (min.)	Tensile Strength N/mm^2 (min.)	Proof Load (kN)	Breaking Load (kN)
R4S	700	960	4516	5720

Table 6.2: *Mechanical properties of the mooring chain chosen.*

Once the mooring chain was selected, the next step involved inputting the mooring data into SeaFem, including the chain's cross-sectional area (m^2) and its effective weight

(N/m). Calculating the effective weight was simply a matter of multiplying the chain's weight by the force of gravity. To determine the chain's cross-sectional area, it was necessary to decide which specific area to consider. Since the chosen chain was a Stud Link Mooring Chain, it was decided to use the cross-sectional area at the center, represented by the red line in Figure 6.4 for visual reference. As an approximation, it was assumed that the stud had the same length and diameter as the chain link's diameter.
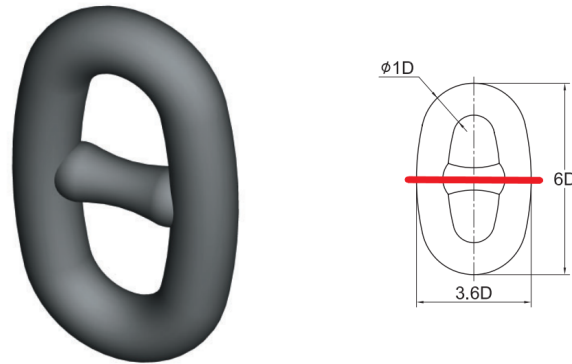

Figure 6.4: *Stud Link dimensions.*

Under the given conditions, the input data for the mooring chain's mechanical properties in SeaFem are as follows,

- Area (m^2) = 0.01015

- Effective Weight (N/m) = 1049.67

- Young Modulus (Pa) = 2.11 E+11

6.3 Pre-processing: DLC I & II

After defining the DLCs and proposing the mooring system, the subsequent step involves the definition of the remaining input parameters in SeaFem to facilitate the seakeeping analysis of the structure. This section will provide a description of DLC I and DLC II, as both DLCs will be executed using an identical draft.

6.3.1 Problem Setup and Description

In order to gain a more accurate understanding of the fish cage's movements, loads, and performance, and ensure the safety, functionality, and structural integrity of the platform, it was decided to run simulations that take into account 2nd order diffraction

radiation. It's important to note that by doing so in SeaFem, the software automatically calculates both 2nd order and 1st order diffraction radiation, saving time and effort by obtaining both results in a single simulation. This approach not only aids in optimizing the design but also provides valuable insights for informed decision-making processes.

A constant depth was used as input, derived from the NOAA database, with a value of 64.6 meters. Additionally, the beach input was set to 49.7 meters, representing the radius of the generated subdomain, as a suggestion from the SeaFEM Reference Manual [44].

6.3.2   Domain and Subdomain Generation

The initial step in determining the size of the domain involves the calculation of the length of the longest anticipated wave. To accomplish this, it is imperative to acquire the longest period, as outlined in the SeaFEM manual [46], which is obtained using the following expression,

$$T_{max} = 2.2 \cdot T_m \tag{6.1}$$

Where,

- The value of T_m represents the average period derived from the NOAA database, dependent on the designated DLC. In this specific scenario, despite the average period for the Operational Condition being lower than that of the Extreme Condition, the value associated with the Extreme Condition will be considered. This choice is made due to the utilization of the same Domain and Subdomain for both simulations.

Based on the information provided, the longest period obtained is 14.30 seconds. Once this maximum period is determined, the next step involves calculating the wavelength associated with that period. This calculation is performed using the dispersion relation for deep water,

$$w^2 = k \cdot g \tag{6.2}$$

Where,

$$w = \frac{2\pi}{T} \tag{6.3}$$

Once the number of waves has been obtained based on the wave period, the length of the wave can be easily calculated using the following expression,

$$k = \frac{2\pi}{\lambda} \Longleftrightarrow \lambda = \frac{2\pi}{k} \tag{6.4}$$

According to the previous equation, the longest wavelength obtained is 319.27 m. Therefore, in order to capture the full range of wave effects in the simulation, it is necessary to set the minimum diameter of the Domain equal to this value.

When it comes to the subdomain, the process is similar, but with a slight variation. Instead of calculating the longest period, the emphasis is on determining the shortest period, as indicated in the manual, which is given by,

$$T_{min} = \frac{T_m}{2.2} \tag{6.5}$$

By employing the same methodology utilized to obtain the longest wavelength, the shortest wavelength is determined to be 13.63 meters.

Figure 6.5 showcases the dimensions chosen for the domain and subdomain. Considering the possibility of tight mooring with the minimum domain size, it was decided to expand it by at least twice to ensure the absence of any potential issues. As for the subdomain, since the minimum diameter obtained is smaller than the actual diameter of the fish cage, there was no specific criteria followed in selecting its size. Instead, the size was primarily chosen to encompass a portion of the area around the fish cage, capturing enough detailed information.
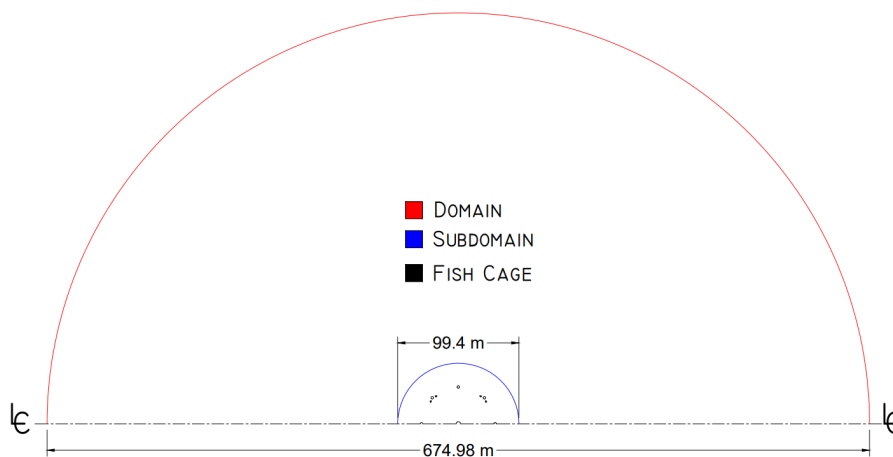

Figure 6.5: *Domain and Subdomain dimensions for DLC I & DLC II.*

Figure 6.6 provides a visual representation of the domain and subdomain modeled for the seakeeping simulation for both DLC I and II.

6.3.3 Environment Data

To describe the ocean wave spectra in the environmental data, a Pierson Moskowitz Wave Spectrum was selected. Table 6.3 provides a concise overview of the wave parameters utilized in the environmental data. In order to obtain the T_{min} and T_{max} values for the DLC II, the same procedure employed for the DLC I was followed.

The mean wave heading input was set to 0, as indicated by the buoy data, which suggests that the primary direction of wave propagation is north. It was assumed that
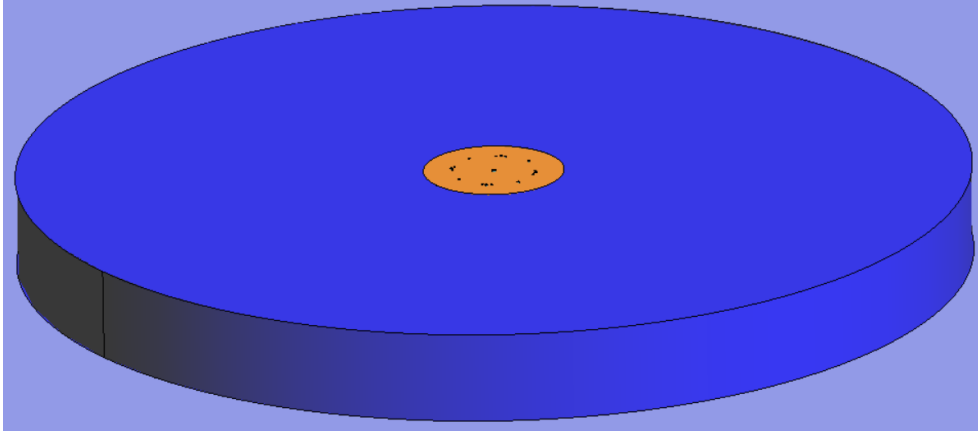
Figure 6.6: *3D representation of domain and subdomain for DLC I & II in SeaFEM.*

Parameter	DLC I	DLC II
H_s (m)	3.10	1.72
T_m(s)	6.50	5.50
T_{min} (s)	2.95	2.50
T_{max} (s)	14.30	12.10

Table 6.3: *Waves parameters input for both DLC I and DLC II.*

the positive X-axis aligns with the north direction. Additionally, a spreading angle of 20° was incorporated, based on the data obtained from the buoy records. To account for wave periods, a count of 5 was specified, along with an equal number of wave headings, resulting in a total of 25 distinct waves for each DLC simulation.

6.3.4   Body Data

Regarding the body data, the weights and center of gravity results for the operational condition were utilized. Additionally, the radius of gyration obtained from the Ram-Series results was incorporated. To comprehensively study the behavior of the sea structure, all degrees of freedom were selected.

6.3.5   Numerical Data and Boundary Conditions

The boundary conditions utilized in the simulation included the typical settings of a free surface, outlet, and a wall condition applied as the bottom boundary. However, several adjustments had to be made to the numerical data in order to resolve stability issues that arose during the simulation. The following changes were implemented to address these concerns,

- Solver: Direct

- Preconditioner: None

- Free surface stability factor: 0.3

- Damping Factor: 0.5

- Free surface scheme: FEM SUPG

- Flow linearization: Slow Double body

6.3.6   Net: Morison Elements

To model the net in the simulation, the Morison elements were utilized. The first step involved estimating the total forces acting on different zones within the net. This estimation considered the respective area of each zone and incorporated the drag coefficient obtained from the CFD analysis, which depended on the current speed specified in the DLCs.

Based on the 3D model, the underwater portions of the net were identified to determine the surfaces involved in the calculation. As the draft remains consistent for both DLCs studied in this section, the same surfaces, namely the lower zone and the lateral zones, are utilized. To facilitate analysis, the lateral zones were divided into two sections, as depicted in Figure 6.7.
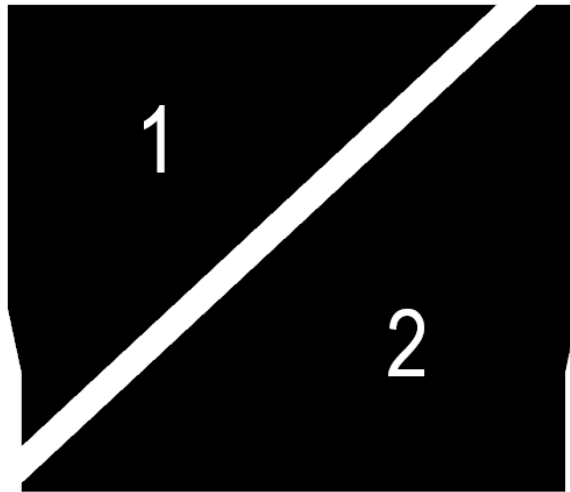

Figure 6.7: *Reference for Division of Net Lateral Zones.*

After acquiring the surface area from the model, the net area was determined using the same method as in the previous chapter's net extrapolation. By incorporating the net area and the C_D obtained from the CFD analysis, the net force for each zone was

easily calculated using the drag force formula. The resulting forces within the net, following the aforementioned procedure, are summarized in Table 6.4.

Zone	Net Panel Surface (m²)	S_n	Net Area (m²)	C_D Net	Net Force (kN)
Lower Zone	2255.31	0.27	913.40	0.989	195.84
Upper Lateral Zone (1)	1200.78	0.27	486.32	0.989	104.27
Lower Lateral Zone (2)	1605.07	0.27	650.05	0.989	139.37

Table 6.4: *Net Areas and Forces for Modeled Morison Elements in Each Zone.*

Once the total force for each zone was determined, the next step involved dividing these forces equally. Firstly, the force of the lower zone was split in half and evenly distributed to both lateral zones. Then, the forces of each lateral zone were divided by eight (8). This ensured that all upper and lower Morison elements experienced their respective forces. It was also considered The following expressions provide a detailed explanation of the procedure,

$$Lateral/Upper\ (1) \;=\; \frac{\left(F_{Lateral\ (1)} + \frac{F_{Lower}}{2}\right)}{8} = 25.27\ kN \tag{6.6}$$

$$Lateral/Lower\ (2) \;=\; \frac{\left(F_{Lateral\ (2)} + \frac{F_{Lower}}{2}\right)}{8} = 29.66\ kN \tag{6.7}$$

Figure 6.8 provides a visual representation of the Morison elements that were modeled. The figure showcases the arrangement and positioning of these elements in relation to the simulated structure. For the specific coordinates corresponding to each Morison element, please refer to the Appendix: Seakeeping Analysis Results
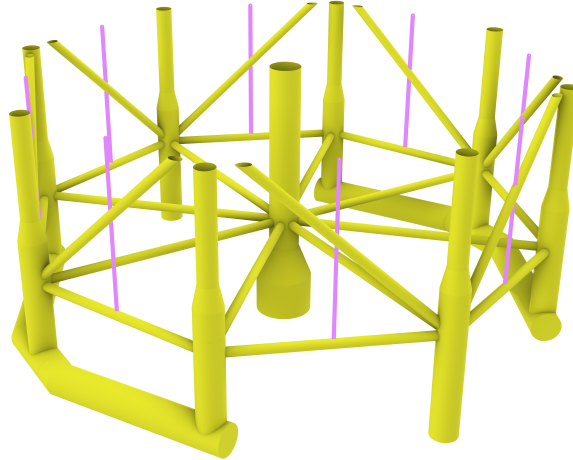

Figure 6.8: *Representation of 3D Morison Elements Modeled with Purple Lines.*

Having calculated the forces acting on each element, it is now necessary to apply the Morison equations to achieve an equilibrium of forces. This involves adjusting the drag and inertia forces incorporated in the Morison equations,

$$F\prime = \frac{dF}{dz} = F_{Drag} + F_{Inertia} \tag{6.8}$$

Where the drag and inertia forces are represented as follows [47],

$$F\prime = \frac{dF}{dz} = C_d \frac{1}{2} \rho u \left| u \right| D + C_i \rho \frac{\partial u}{\partial t} \pi \frac{D^2}{4} \tag{6.9}$$

- Wave-Induced Drag Forces

In the wave-induced drag forces, the variable u denotes the horizontal wave particle velocity, which is described by the following expression (this expression considers deep waters),

$$u = \frac{H \cdot w \cdot \cosh\left[k(z+h)\right]}{2 \cdot \sinh(kh)} \cos(kx - wt) \tag{6.10}$$

To estimate this value, a MATLAB code was created to calculate the horizontal and vertical wave particle velocities at a given depth. The code generated a plot showing the velocity vectors for each particle's position, as depicted in Figure 6.9. The maximum horizontal velocity obtained from the plot was used to calculate the drag forces. It is important to note that this value needs to be combined with the current speed obtained from the site data. Table 6.5 provides the horizontal velocities obtained for both conditions, including the corresponding current speed.

(a) *Operational Condition.*   (b) *Extreme Condition.*
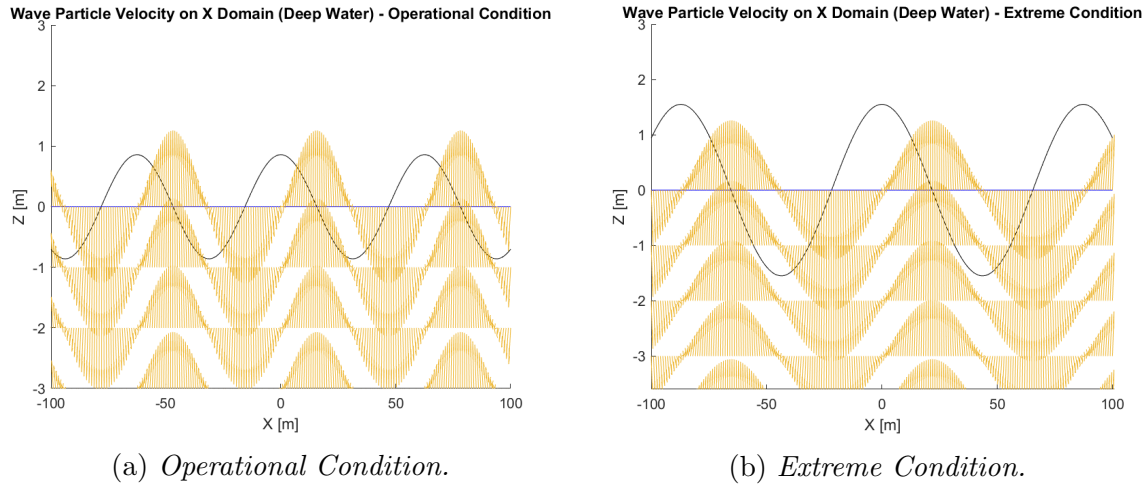
Figure 6.9: *Wave Particle Velocity on X Domain (Deep Water).*

- Wave-Induced Inertia Forces

In the wave-induced inertia forces, the variable $\partial u/\partial t$ denotes the horizontal wave particle acceleration, which is described by the following expression (this expression considers deep waters),

$$\frac{\partial u}{\partial t} = \frac{H \cdot w^2 \cdot \cosh\left[k(z+h)\right]}{2 \cdot \sinh(kh)} \sin(kx - wt) \tag{6.11}$$

The same MATLAB code that was used to calculate the horizontal velocity was also employed to determine the horizontal acceleration. By adjusting the input equation, the code generated a plot depicting the acceleration vectors for each particle's position, as shown in Figure 6.10. Additionally, the maximum horizontal acceleration was obtained. Table 6.5 provides the horizontal accelerations obtained for both conditions.
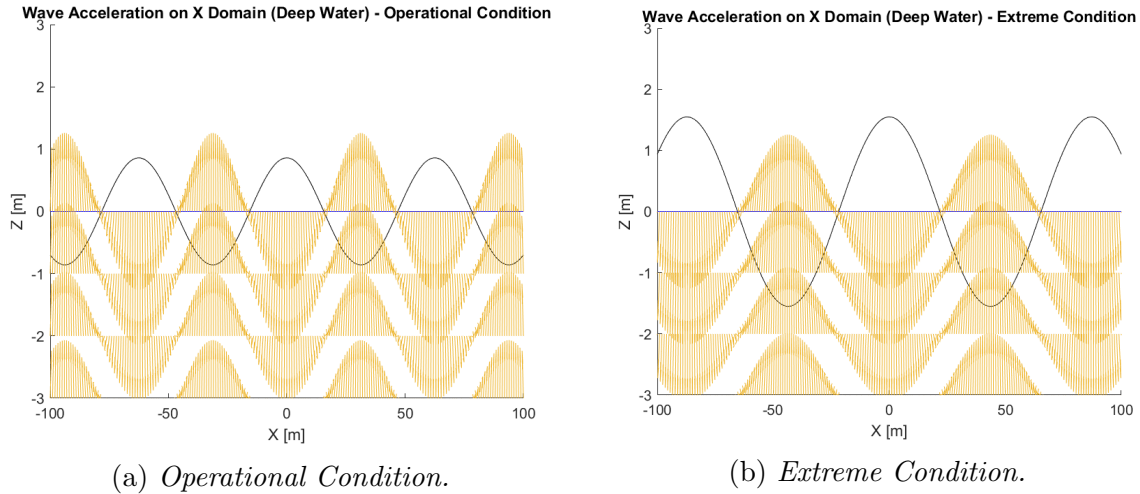

(a) *Operational Condition.*   (b) *Extreme Condition.*

Figure 6.10: *Wave Particle Acceleration on X Domain (Deep Water).*

Once the horizontal particle velocities and accelerations were determined for the upper and lower elements in both conditions, the next step was to find a suitable diameter and select appropriate drag and inertia coefficients. This was done to ensure that the Morison elements could effectively represent the entire net by generating the same forces as observed in the actual net structure.

The C_d and C_i were obtained using the plots shown in Figure 6.11a and Figure 6.11b. These plots, extracted from reference [47], provide empirical information on the behavior of a smooth circular cylinder and the corresponding drag and inertia coefficients based on the KC number.

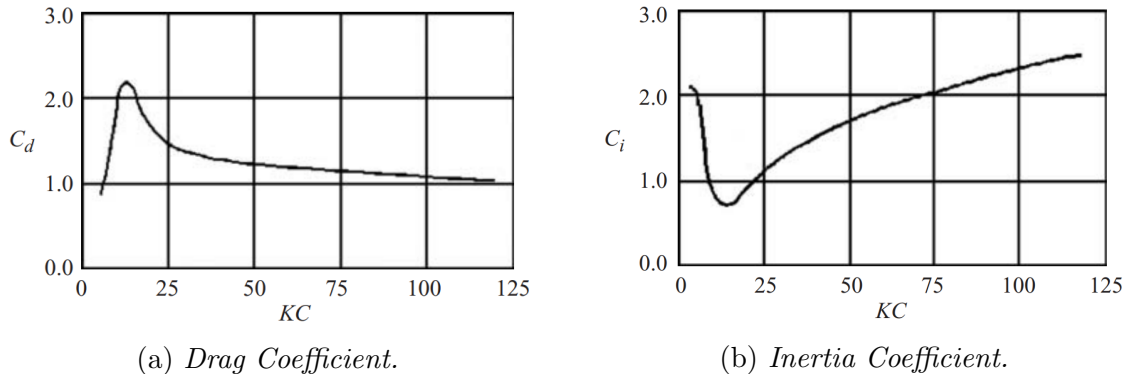(a) *Drag Coefficient.*   (b) *Inertia Coefficient.*

Figure 6.11: *Behavior of a Smooth Circular Cylinder in an Oscillatory Flow as a Function of the Keulegan-Carpenter Number.*

KC represents the Keulegan-Carpenter Number, which is a dimensionless parameter used in fluid dynamics to characterize the flow around objects in a fluid medium [47]. It helps in predicting the occurrence of phenomena like vortex shedding, drag coefficient variations, and flow separation. The KC number for a circular cylinder considering deep waters is represented by the following formula,

$$KC|_{deep} = \frac{\pi \cdot H_s}{D} \tag{6.12}$$

By utilizing the KC formula, referring to Figure 6.11a and Figure 6.11b, and conducting iterative adjustments to the diameter of the elements, an agreement was established between the forces obtained from the Morison equation and the forces observed in the net structure. The obtained results and the input parameters for computing the forces using the Morison equations are summarized in Table 6.5. It is evident that the wave-induced inertia forces exhibit greater significance when compared to the drag forces.

Item	Upper		Lower	
	Extreme	Operational	Extreme	Operational
Density	1026.24	1026.24	1026.24	1026.24
Diameter (m)	0.1146	0.1666	0.1287	0.1878
H_s (m)	3.10	1.72	3.10	1.72
Current Speed (m/s)	0.65	0.65	0.65	0.65
Wave Particle Velocity (Horizontal) (m/s)	1.30	0.85	1.30	0.85
Wave Particle Acceleration (Horizontal) (m/s^2)	1.10	0.85	1.10	0.85
Total Speed (m/s)	1.95	1.50	1.95	1.50
KC	85.00	32.43	75.68	28.78
C_i	2.16	1.32	2.01	1.22
C_d	1.11	1.34	1.15	1.37
Wave Inertia Force (kN)	25.03	25.02	29.38	29.37
Wave Drag Force (kN)	0.24	0.25	0.28	0.29
Total Force (kN)	25.28	25.28	29.66	29.66

Table 6.5: *Morison wave-induced drag and inertia forces obtained for both conditions based on coefficient and inputs parameters.*

Once the calculations for the Morison elements were finalized, the next step involved inputting the obtained results into SeaFEM. In SeaFEM, the Morison elements are incorporated using the "Slender Elements" parameter. Each Morison element is defined by its respective coordinates (as listed in Appendix: Seakeeping Analysis Results), along with the values presented in Table 6.6. It is important to specify the section area, which corresponds to the cross-sectional area of the cylinders. The option "Virtual Element" was selected so it was not necessary to 3D model each one of the elements.

Item	Extreme		Operational	
	Upper	**Lower**	**Upper**	**Lower**
Diameter	0.1146	0.1287	0.1666	0.18776
Section Area (m^2)	0.01031	0.01301	0.02180	0.02769
C$_d$	1.11	1.15	1.34	1.37
C$_i$	2.16	2.01	1.32	1.22

Table 6.6: *Slender elements input parameters into SeaFEM.*

6.3.7   Simulation Time

According to the guidelines, the recommended simulation time for replicating a storm scenario was set at 3 hours. However, considering the significant computational cost and the anticipated extensive duration for completion on the available machine, it was deemed more practical to reduce the simulation time to 30 minutes (1800 seg).

The determination of output times was based on the criterion of capturing a minimum of 4 data points of the wave with the shortest period. Consequently, the following output times were specified for both DLC,

- DLC I = 0.74 s

- DLC II = 0.63 s

The initialization time was set to 5 seconds, while the recording time was selected as 300 seconds. These values were determined after several iterations and evaluations of the model. It was observed that significant results were not expected to appear before the 300-second mark during the recording period.

6.3.8   Meshing

To create a mesh for the Fish Cage in SeaFEM, a mix of structured and unstructured triangular elements was employed. The goal was to achieve a detailed representation of the cage structure and its surroundings.

In order to facilitate the meshing process, specific cuts were made in the model to accommodate different types of elements with varying sizes, as can be seen in Figure 6.12. These cuts were strategically placed in areas where finer mesh resolution was needed to capture important features and structural details accurately.

Structured elements, known for their regular shape, were used in regions where a controlled and efficient meshing was desired. They were suitable for capturing the overall geometry and primary structural components of the cage.
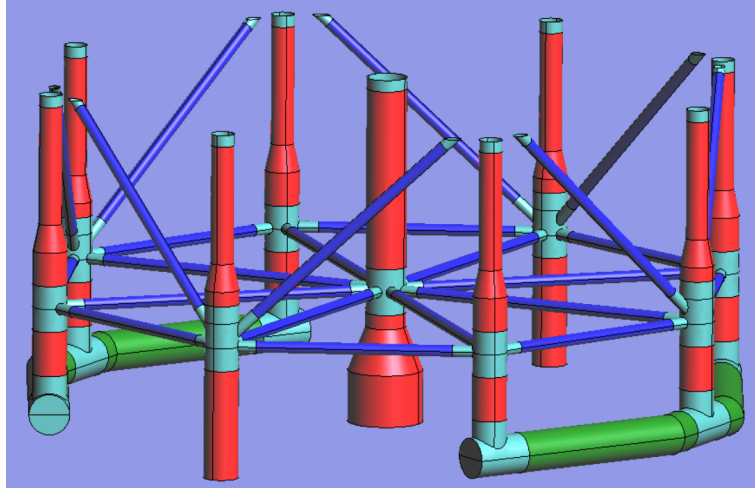
Figure 6.12: *Division of Fish Cage input in SeaFEM into multiple sections to accommodate the application of different types of elements.*

Unstructured elements, on the other hand, were employed in areas with irregular shapes or complex geometries (joints). They provided more flexibility and adaptability, allowing for a more accurate mesh representation of details and local variations in the cage structure.

Figure 6.13 visually illustrates the resulting mesh, showcasing the combination of structured and unstructured elements in the Fish Cage model. This approach ensured a comprehensive and accurate representation of the cage, encompassing both the overall structure and finer details necessary for the simulation analysis.
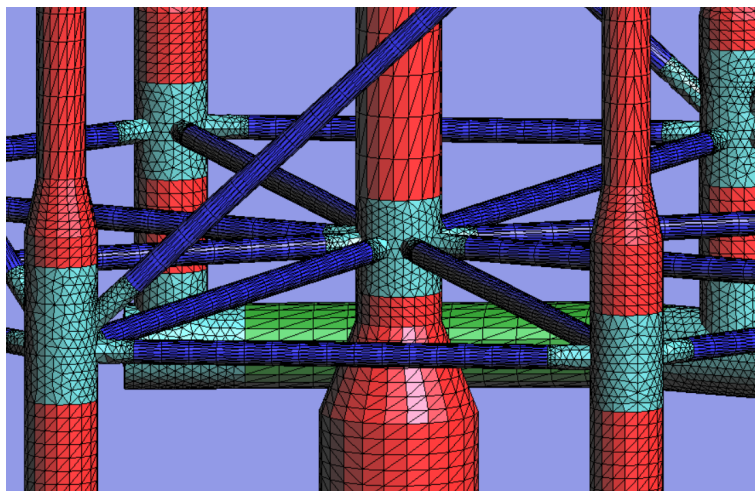
Figure 6.13: *Combination of structured and unstructured elements in Fish Cage.*

After completing the cage meshing, the next step was to mesh the domain and subdomain. To do this, it was necessary to determine the desired number of elements per wave, which in this case was chosen as 5 elements per wave. This meant that the

minimum size required for each element would be obtained by dividing the wave length by five (5). To determine the element size for the domain, the longest wave in both DLCs was identified. These wave values were obtained during the generation of the domain and subdomain. Once the longest wave values were obtained, the minimum element size required could be determined. The same process was applied to calculate the element size for the subdomain, using the shortest wave length this time. The results for the minimum sizes per element are presented in Table 6.7.

Item	Extreme		Operational	
	Longest Wave	**Shortest Wave**	**Longest Wave**	**Shortest Wave**
Length (m)	319.272	13.629	228.591	9.758
Length / 5	53.2	2.95	38.1	2.0

Table 6.7: *Minimum sizes per element for domain and subdomain for both DLCs.*

Figure 6.14 illustrates the generated domain mesh for both DLCs. A size of 30 m was chosen for the domain, mainly because the minimum sizes obtained were perceived as somewhat larger than desired.
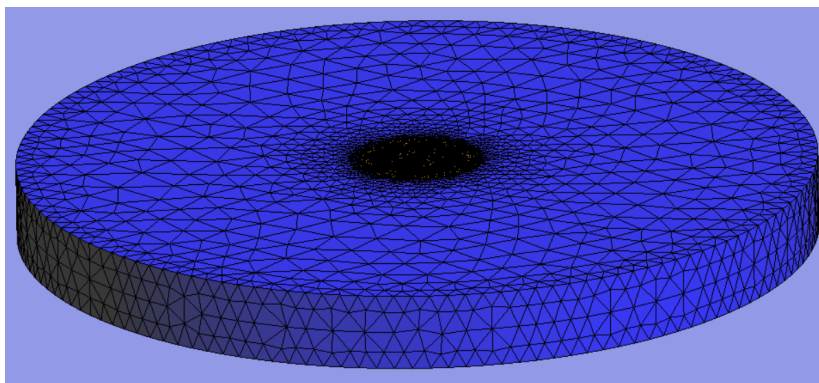
Figure 6.14: *Domain Mesh for DLCs I and II.*

Regarding the subdomain, the minimum required element size was exclusively applied to the free surface since it is the part of the subdomain that effectively captures the impact of the waves. In contrast, for the remaining portions of the subdomain, an element size of 5 m was employed for the volume, while a size of 10 m was utilized for the surrounding area. Figure 6.15 depicts the subdomain mesh generated for DLC I, which bears resemblance to the subdomain mesh for DLC II.

Significant consideration was given to the areas where the free surface intersects with the fish cage in order to ensure a seamless transition. To achieve this, a refined mesh was applied to the fish cage, aiming to create a smoother connection between the free surface and the cage. This approach proved beneficial in optimizing the stability factor within the numerical data and mitigating potential errors. Figure 6.16 offers a detailed view of the surface transition, highlighting the implemented refinements.

The number of elements generated for each simulation is listed as follows,
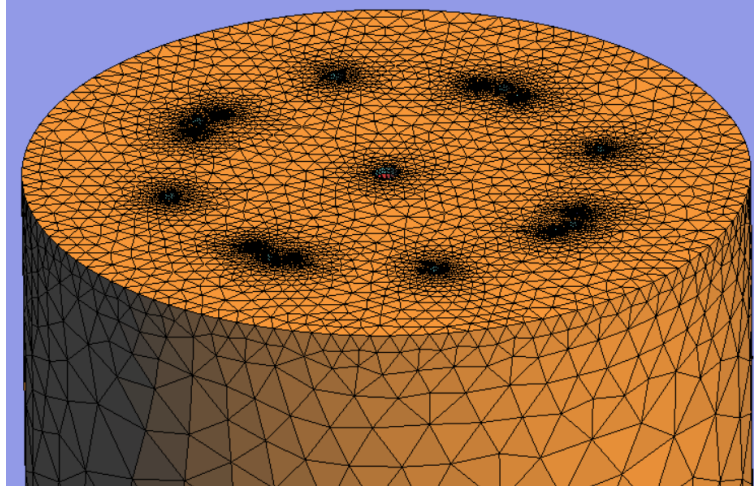
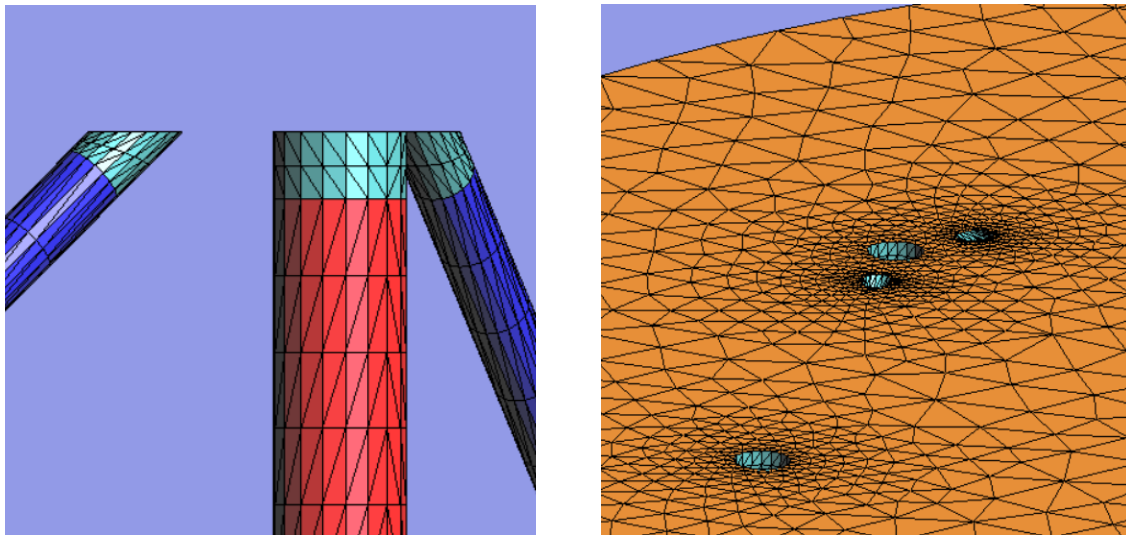Figure 6.15: *Subdomain Mesh for DLC I.*

Figure 6.16: *Detailed Examination of Mesh Refinement for Improved Surface Transition.*

- DLC I = 344,546 elements

- DLC II = 334,352 elements

6.4   Post-processing: DLC I & II.

After completing the initial setup and executing the simulations, the subsequent stage involved post-processing the obtained results. This phase aimed to assess the motions of the structure and identify any critical degrees of freedom that exhibited significant offsets. The positioning for mooring systems requirements from ABS [48] were followed.

In addition, the tensions observed in the mooring lines underwent an assessment during the post-processing phase. The objective was to verify the ability of the mooring system to withstand the environmental loads it encountered. By analyzing the tensions, it was possible to determine if the mooring lines were subjected to excessive stress and to consider any necessary adjustments on their mechanical properties.

Figure 6.17 shows the contour fill of the free surface obtained from the DLC I, along with the fish cage and the mooring lines generated.
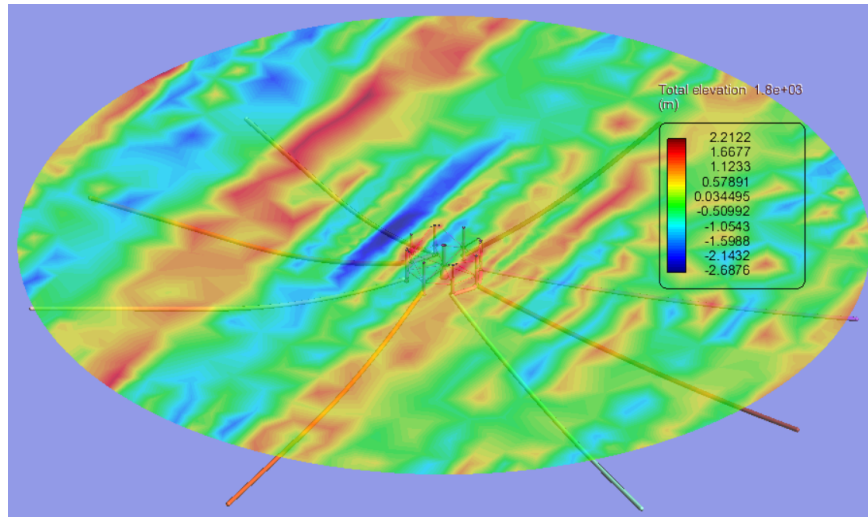
Figure 6.17: *Free Surface Contour Fill Results from the Extreme Design simulation of the results from the Extreme Design simulation, along with the fish cage and the catenary input.*

6.4.1   Seakeeping Response

6.4.1.1   Motion Results

In the seakeeping response study, the primary motion under investigation for both conditions was Surge, as it tends to exhibit the most significant offsets for offshore structures. A criterion was established to ensure that the structure did not exceed a maximum offset of 5 meters. This criterion was driven by two main reasons. Firstly, the location of the fish cage is a key factor, considering the high vessel traffic in the Massachusetts Bay area, as indicated by the traffic density map depicted in Figure 6.18.

Another reason for setting a maximum permitted value of 5 meters for surge offset was to minimize the impact on the fish. Significant offsets in the structure can easily stress the fish, leading to poor quality and increased mortality rates. By keeping the surge offset within this limit, it was intended to minimize the negative consequences on the fish population, ensuring their well-being and reducing any potential harm.
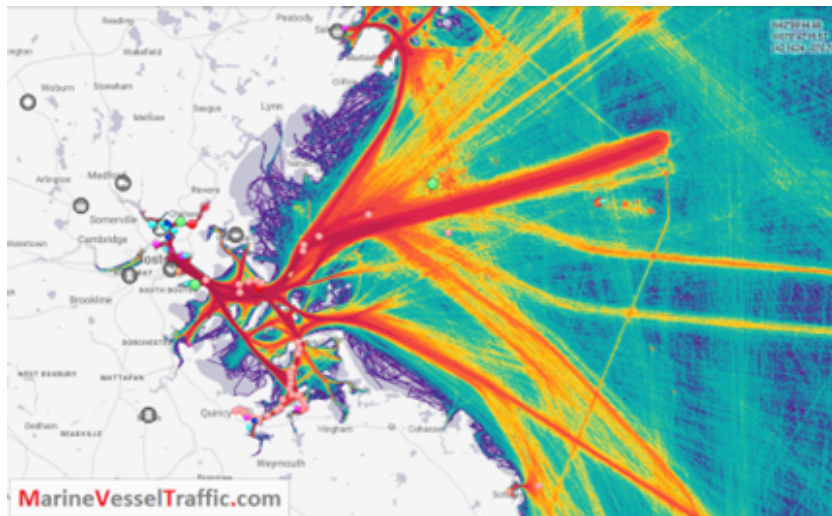
Figure 6.18: *Massachusetts Bay Traffic Density Map [49].*

The obtained results for surge 1st order diffraction radiations in the extreme condition are presented in Figure 6.19a as a time-domain signal. The maximum value recorded was 2.67 meters. Based on this observation, it can be concluded that, at least for the 1st order results, the obtained value satisfies the set criteria of allowing a maximum surge offset of 5 meters.

The obtained results for surge 2nd order diffraction radiations in the extreme condition are presented in Figure 6.19b as a time-domain signal. The maximum value recorded was 2.66 meters. Based on this observation, it can be concluded that for both orders of diffraction radiation the criteria was satisfied.

(a) *1st Order Diffraction Radiation*

(b) *2nd Order Diffraction Radiation*
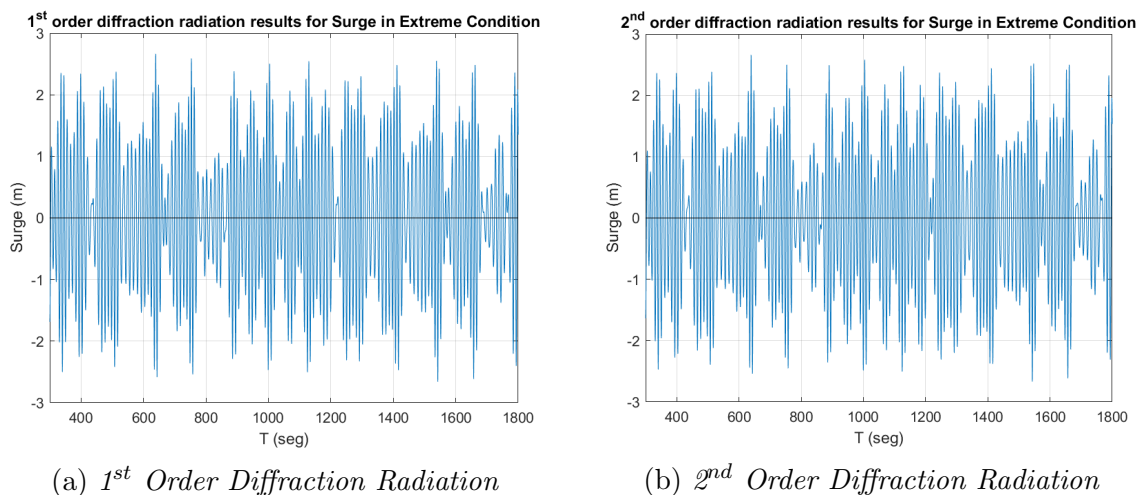
Figure 6.19: *Surge Results for Extreme Conditions in a Time-Domain Signal.*

To compare the results obtained for the 1st and 2nd order analyses, Figure 6.20 shows the difference between them. The absolute error value obtained was approximately 1.16%, indicating a very small difference. This suggests that the 1st order

results are sufficient for evaluating the seakeeping response of the structure, and the 2nd order results have minimal impact on the analysis.
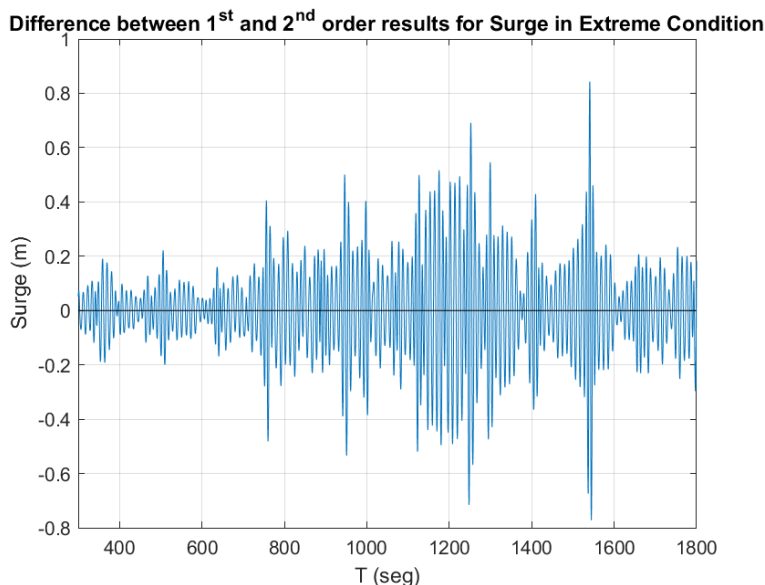
Figure 6.20: *Difference between 1st and 2nd Order Diffraction Radiation results for Extreme Condition in a Time-Domain Signal.*

In order to provide a more comprehensive assessment of the results for the main motions with offsets (surge, sway, and heave) obtained from the seakeeping analysis for both DLCs, additional metrics beyond the maximum values were considered. The absolute mean and significant values were also determined. The significant values were obtained by sorting the results in descending order and selecting the highest third values for each motion, similar to how significant wave height is calculated. Table 6.8 presents the results obtained for each motion, considering both conditions (extreme and operational) and accounting for both 1st and 2nd order analyses.

Motion	Measurement	1st Order		2nd Order	
		Extreme	Operational	Extreme	Operational
Surge (m)	Max	2.67	2.53	2.66	2.46
	Significant	1.23	1.33	1.22	1.41
	ABS Mean	0.92	0.93	0.91	1.06
Sway (m)	Max	1.11	0.05	1.41	0.04
	Significant	0.44	0.02	0.47	0.02
	ABS Mean	0.33	0.01	0.35	0.01
Heave (m)	Max	0.47	0.46	0.49	0.44
	Significant	0.37	0.36	0.37	0.33
	ABS Mean	0.26	0.25	0.26	0.21

Table 6.8: *Maximum, Significant and Absolute mean values obtained for Surge, Sway and Heave Motions in 1st and 2nd Order for both Extreme and Operational Conditions.*

The remaining plots for all other motions are available in Appendix: Seakeeping Analysis Results.

6.4.1.2 Low and Wave Frequency Motions

To further characterize the offset of a moored floating structure in compliance with ABS rules, wave and low-frequency motions were calculated for both extreme and operational conditions. It is important to note that the following plots only depict the extreme condition, while the corresponding plots for the operational condition can be found in the Annex section.

To achieve this, the time-domain signals obtained for the surge motion were transformed into frequency-domain signals using a MATLAB code with the Fourier transform. The signals were first normalized to ensure consistent amplitudes across different signals and to prevent distortions in the frequency spectrum. Figure 6.21a and Figure 6.21b illustrate the frequency-domain signal plots for the extreme conditions, considering both 1st and 2nd order analyses.

(a) *1st Order Diffraction Radiation*   (b) *2nd Order Diffraction Radiation*
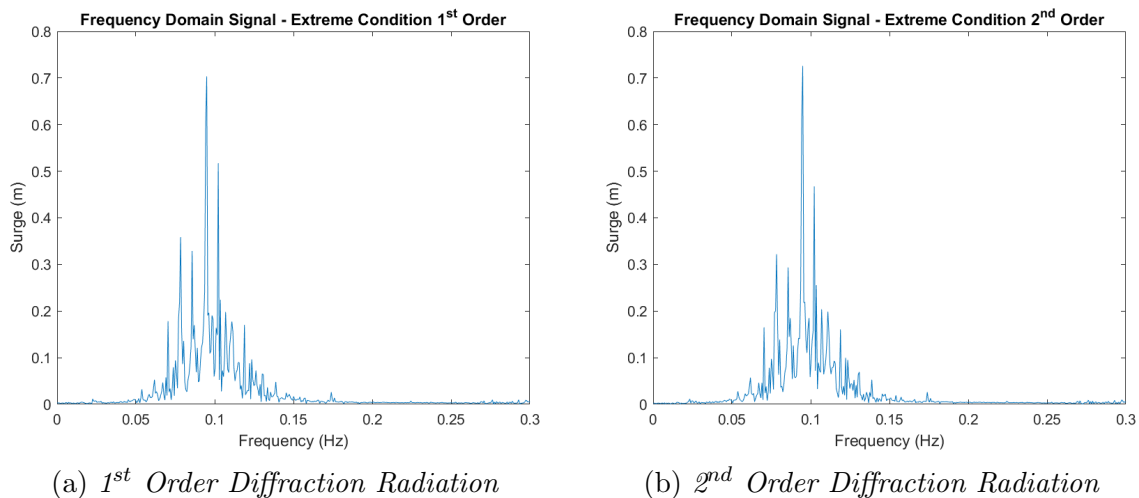
Figure 6.21: *Surge Results for Extreme Conditions in a Frequency-Domain Signal.*

Using the same MATLAB code, the frequency domain signals were further processed to obtain the energy spectrum for both of them. The energy spectra can be observed in Figure 6.22a and Figure 6.22b.

Once the energy spectrum plots have been obtained, it is possible to calculate statistical moments such as m_0 and m_2 using the following equations,

$$m_0 = \int_0^\infty S_{\eta\eta}(w) \, dw \tag{6.13}$$

$$m_2 = \int_0^\infty w^2 \cdot S_{\eta\eta}(w) \, dw \tag{6.14}$$

(a) *1st Order Diffraction Radiation*   (b) *2nd Order Diffraction Radiation*
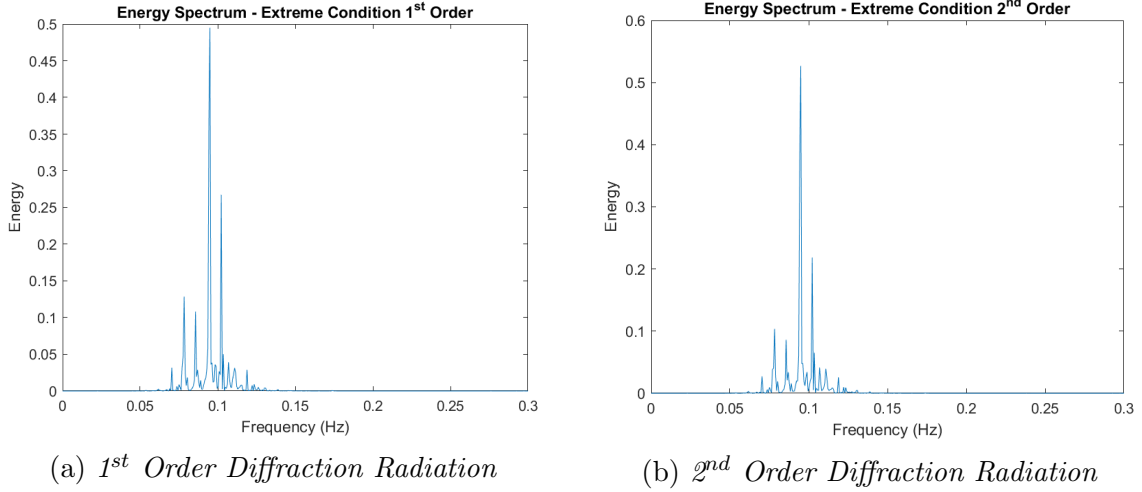
Figure 6.22: *Surge Energy Spectrum for Extreme Conditions.*

Using these statistical moments, it is possible to calculate the variance and the average response zero up-crossing period with the following equations,

$$\sigma = \sqrt{m_0} \tag{6.15}$$

$$T_a = 2\pi \sqrt{\frac{m_0}{m_2}} \tag{6.16}$$

Finally, for obtaining the maximum (S_{max}) and significant (S_{sig}) single amplitude values for both conditions, according to ABS [48], the following equations must be employed,

$$S_{sig} = 2 \cdot \sigma \tag{6.17}$$

$$S_{max} = \sigma \sqrt{2 \cdot lnN} \tag{6.18}$$

Where,

- N=T/T_a.

- T = Specified storm duration (seconds), minimum of 10,800 seconds (i.e., 3 hours).

Table 6.9 displays the results for all the mentioned equations for both DLCs and for both wave and low-frequency components.

6.4.2   Mooring Tensions

In order to examine the mooring tensions obtained, the results for each individual catenary line were analyzed. Figure 6.23 serves as a reference, providing an ID for each

Variable	1st Order (Wave Frequency)		2nd Order (Low Frequency)	
	Extreme	Operational	Extreme	Operational
m_0	0.022	0.019	0.022	0.018
σ sigma	0.147	0.138	0.147	0.134
S_{sig} (m)	0.294	0.276	0.295	0.268
m_2	0.058	0.078	0.060	0.050
T_a (s)	3.851	3.103	3.772	3.774
N	2804.471	3480.231	2862.940	2861.923
S_{max} (m)	0.586	0.558	0.588	0.535

Table 6.9: *Significant single amplitude low and wave frequency Motion values obtained for Surge in 1_{st} and 2nd Order for both Extreme and Operational Conditions.*

catenary line along with an image of the time step at which the maximum tension of 5291 m was recorded for mooring line H1. The plots depicting the tensions obtained for all the mooring lines can be found in Appendix: Seakeeping Analysis Results.
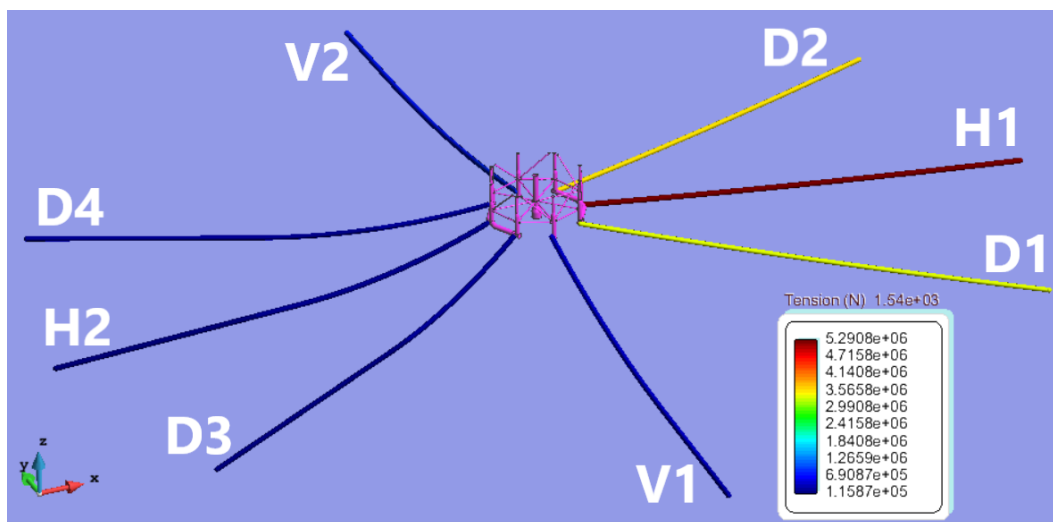
Figure 6.23: *Mooring Tension Results with ID Reference for Each Catenary Line.*

To better understand the loads on the mooring lines, similar to the seakeeping analysis, the maximum, significant, and absolute mean values for each mooring line were obtained for both conditions. These values are presented in Table 6.10.

Overall, it is evident that the H and D mooring lines experience greater loads compared to the V lines. This outcome was anticipated considering the mean heading input in the wave data, which was set to 0° with a spread angle of 20°, based on data obtained from the site buoy. Consequently, most of the waves travel parallel to the H and D lines (X-axis), while the V lines (Y-axis) experience waves perpendicular to them. As a result, the H and D lines are subjected to higher tension as they bear the primary impact of wave forces, whereas the V lines are relatively less affected.

Measurement	Extreme			Operational		
	Max	Significant	ABS Mean	Max	Significant	ABS Mean
Tension H1 (kN)	5291.00	1386.77	835.17	4179.00	1528.29	872.93
Tension D1 (kN)	3729.00	1243.27	791.36	2754.00	1307.02	805.11
Tension D2 (kN)	3896.00	1231.66	788.70	2809.00	1308.99	805.72
Tension V1 (kN)	1319.00	837.22	689.94	688.50	678.11	669.95
Tension H2 (kN)	5167.00	1392.83	836.74	3965.00	1535.79	875.52
Tension D3 (kN)	4078.00	1236.72	789.98	2671.00	1313.45	807.19
Tension D4 (kN)	4560.00	1249.05	793.36	2650.00	1312.45	807.01
Tension V2 (kN)	1387.00	834.86	689.46	688.80	677.98	670.25

Table 6.10: *Maximum, Significant, and Absolute Mean Values of Mooring Tensions for both Extreme and Operational Conditions.*

It is important to note that maintaining the proper mooring system installation configuration is crucial to ensure the catenary lines can withstand the loads. Therefore, it is recommended to align the H1 and H2 lines parallel to the north and south directions, while the V1 and V2 lines should be perpendicular to the west and east directions.

For obtaining a more global result for all the mooring lines to check if in fact the type of catenary selected can withstand the loads, the maximum value for each measurement from Table 6.10 were obtained and summarized in Table 6.11.

The maximum value obtained is below the breaking load (Ultimate Stress), but it surpasses the permitted proof load (Table 6.2) for the selected catenary. However, the proof load is exceeded only four (4) times in all the results. It is evident that the maximum absolute mean and significant global values obtained are significantly lower than the proof load. Based on these findings, it can be concluded that the chosen catenary is fully capable of withstanding all the tensions without any concerns.

Global Tension Results		
Max (kN)	5291.00	Tension H1 – Extreme
ABS Mean (kN)	875.52	Tension H2 – Operational
Significant (kN)	1535.79	Tension H2 - Operational

Table 6.11: *Global Mooring Tension Results.*

6.5   Pre-processing: DLC III

The pre-processing of DLC III followed the exact same procedure as DLC I and II for the calculation, measurement, and definition of all input parameters for the simulation. Table 6.12 provides a summary of the main inputs into SeaFEM, while the remaining parameters not mentioned were set to their default values in SeaFEM. In this case, currents, mooring elements, and slender elements were not considered, and there were no modifications made to the numerical data.

Problem Setup	1_{st} Order Diffraction Radiation	
Problem Description	Depth	64.6 m
	Beach	35.35 m
Environment Data: Wave	Wave Spectrum Type	Pierson Moskowitz
	Mean Wave Period	3.5 s
	Significant Wave Height	0.91 m
	Shortest Period	1.59 s
	Longest Period	7.70 s
	Number of Waves Periods	5
	Mean Wave Heading	0.0 deg
	Spreading Angle	20 deg
	Number of Waves Headings	5
Time Data	Simulation Time	300 s
	Output Step	0.4 s
	Start Time Recording	5 s
	Initialization Time	5 s

Table 6.12: *Transport Condition Main Input Parameters.*

Figure 6.24 illustrates the domain and subdomain dimensions for DLC III, which were determined based on the environmental data obtained from the site and the recommendations provided in the SeaFEM manual. The objective was to capture the longest and shortest waves in the simulation accurately.
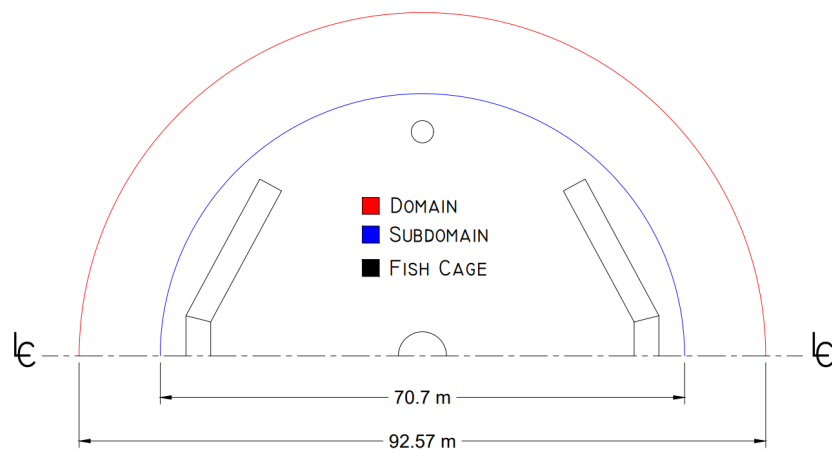
Figure 6.24: *Domain and Subdomain dimensions for DLC III.*

6.5.1   Meshing

Similar to the procedures followed for the extreme and operational conditions, the initial step in determining the minimum sizes per element for the domain and subdomain in DLC III involved obtaining the lengths of the shortest and longest waves and dividing

them by five (5). Table 6.13 provides an overview of the minimum sizes per element for the transport condition.

Wave	Length (m)	Length / 5
Shortest Wave	3.95	0.8
Longest Wave	92.570	30.9

Table 6.13: *Minimum sizes per element for domain and subdomain for both DLC III.*

Figure 6.25 shows the 3D domain and subdomain model, along with the fish cage at the transport condition draft cut, which were input into SeaFEM. The element size chosen for the domain was 30 m, resulting in a total of 186,682 elements generated.

(a) *Domain and Subdomain.*   (b) *Domain Mesh.*
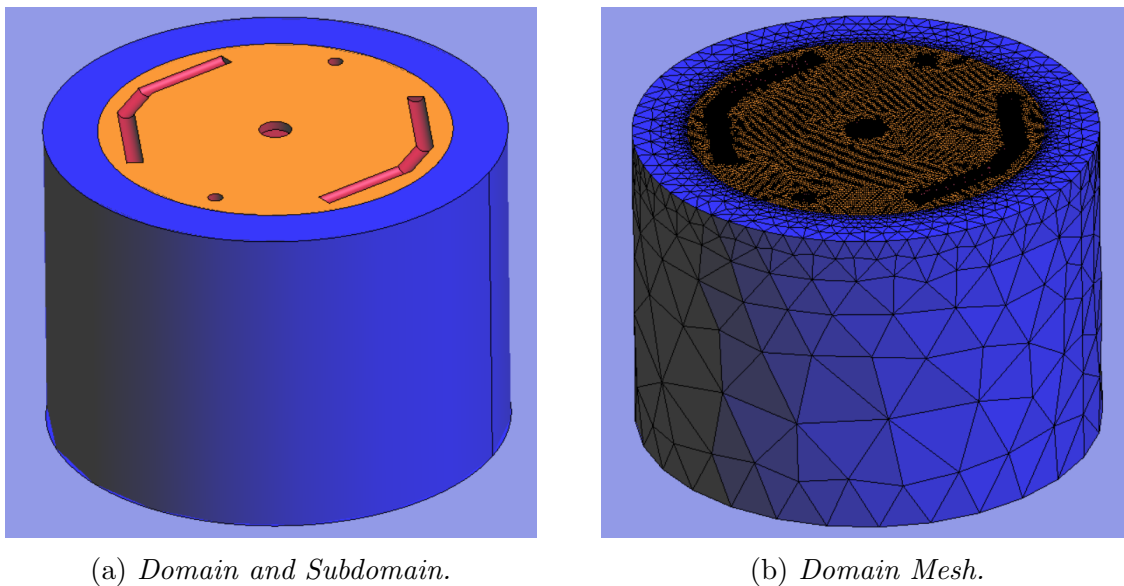
Figure 6.25: *DLC III SeaFEM Model*

In this case, as shown in Figure 6.26, only unstructured elements were used to model the fish cage because most of the shapes were irregular.

6.6   Post-processing: DLC III

In the post-processing stage of the transport condition, considering that the structure is being towed into position, it is not necessary to analyze motions such as surge and sway. Therefore, the study focused on the heave, roll, and pitch motions. Figure 6.27 displays the simulation results for the free surface contour.

Similar to the seakeeping analysis post-process for the previous DLCs, the maximum, significant, and absolute mean values for each motion were obtained. These values are presented in Table 6.14.
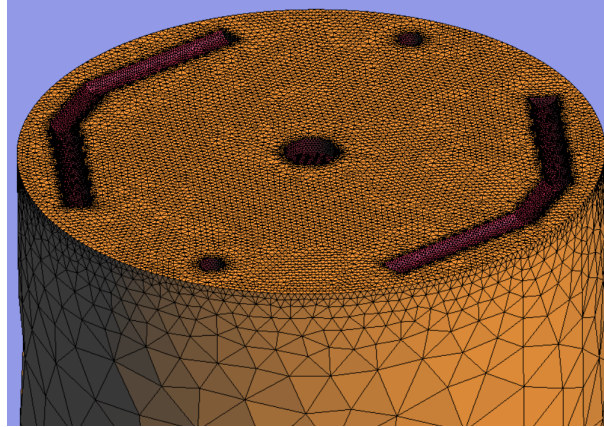
Figure 6.26: *DLC III Subdomain Mesh.*
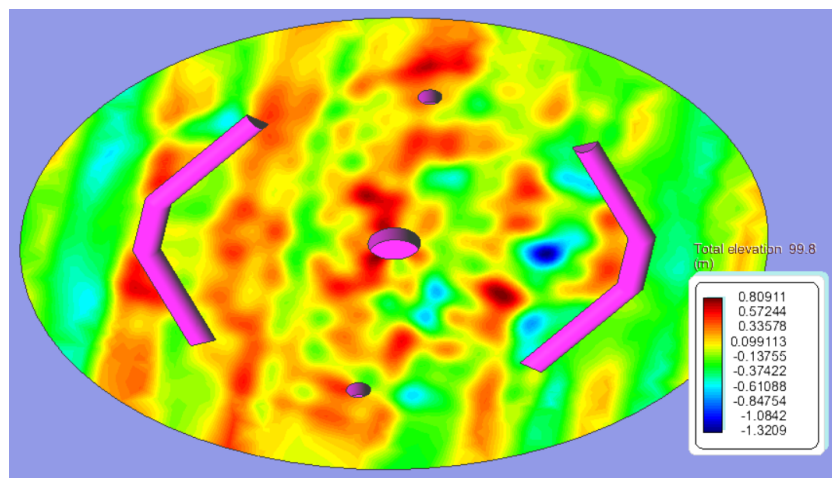
Figure 6.27: *Free Surface Contour Fill Results from the Transport Condition Simulation.*

Measurement	Heave (m)	Roll (°)	Pitch (°)
Max	0.20	0.0054	0.0085
Significant	0.08	0.0030	0.0042
ABS Mean	0.06	0.0023	0.0032

Table 6.14: *Maximum, Significant and Absolute mean values obtained for Heave, Roll and Pitch Motions.*

Based on the results obtained, it is clear that the structure will have no issues with its seakeeping performance in the transport condition. The roll and pitch motions do not exceed 0.01°, ensuring stability and minimal tilting. As for the heave motion, the maximum offset observed is only 20 cm, which is quite low. It is important to consider that these values were obtained under Beaufort Scale 3 conditions to ensure a safe transportation and installation process, minimizing the risk of any major accidents.

Chapter 7

Conclusions

In summary, the conclusions of this project are primarily drawn from the optimization of the net design, the comparison between square and hexagonal meshes, and the comprehensive seakeeping analysis. These findings provide valuable insights into the effectiveness of different design choices and their impact on seakeeping responses and the mooring system.

Furthermore, an additional section has been included that provides recommendations and suggestions for future work. This section presents personal insights and proposed ideas for optimizing the design of the offshore fish cage, next steps, and further research.

7.1 CFD Optimization of the Net Design

- The relationship between the drag coefficient and the solidity ratio for a specific net panel configuration remains inconclusive. It was observed that, within a certain range (0.208 to 0.249), an increase in the solidity ratio corresponded to an increase in the drag coefficient for both the square and hexagonal mesh configurations. However, interestingly, for a square mesh with a solidity ratio of 0.265 and a hexagonal mesh with a solidity ratio of 0.27, the drag coefficient exhibited a decrease compared to the previous net panel. This suggests that the relationship between the solidity ratio and drag coefficient is not consistently linear and may be influenced by other factors.

- By comparing the drag coefficients of the 15-2, 13-2, and 17-3 net panels between the square and hexagonal mesh configurations, the average errors obtained were 11.15%, 3.07%, and 0.49%, respectively. These results suggest that the drag coefficients of the hexagonal configurations are generally lower than those of the square configurations. However, it is noteworthy that the difference between the

drag coefficients decreases as the solidity ratio increases. In fact, there is a point at which the drag coefficient of a square configuration becomes lower than the drag coefficient of a hexagonal configuration, although the difference is minimal within the studied range of solidity ratios. This suggests that the hexagonal shape effectively reduces drag forces induced by water flow.

7.2   Seakeeping Analysis

- The maximum value recorded for the surge motion considering both 1st and 2nd order diffraction radiation was 2.67 meters. Based on this observation, it can be concluded that the obtained value satisfies the set criteria of allowing a maximum surge offset of 5 meters.

- A comparison between the 1st and 2nd order results indicated that the average error between them was approximately 1.16%, so for this simulation case, the 2nd order didn't have much of an impact on the behavior of the structure.

- The mooring system is fully capable of withstanding all the tensions without any concerns, despite four (4) instances where the obtained tensions exceeded the Yield Strength of the selected catenary.

- In terms of the structure's transport condition, it was found to easily meet all stability criteria across a wide range of heel angles. This was expected given the structure's significant inertia in both the longitudinal and transverse axes. As for the seakeeping analysis results, it was concluded that the structure can be safely transported to its destination as long as the sea state is no higher than 3 on the Beaufort scale.

7.3   Recommendations and Future Work

- Despite conducting a CFD analysis to optimize the net design and compare two distinct net configurations in terms of the drag coefficient, it would be equally compelling to assess the same net configurations in the context of seakeeping analysis. This comparative evaluation aims to determine whether these configurations exert a notable influence on the motions of the fish cage and the tensions of the mooring system.

- It is advisable to perform another seakeeping analysis iteration without the V mooring lines. The results indicate that these lines were not significantly affected by environmental forces. Hence, it would be worthwhile to assess the tension distribution in the remaining catenaries and evaluate the overall behavior of the structure if these lines were eliminated. If minimal changes are observed, it would

be wise to consider their removal, as it would help reduce costs and the overall weight of the structure.

- An important aspect that remains to be addressed in the study of the fish cage is the structural analysis, which includes evaluating both static and dynamic loads. The key objectives are to optimize the thickness of the structure and assess its ability to withstand the pressure forces exerted by environmental loads, as well as the potential loads generated by the movements of the fish within the fish cage.

Bibliography

[1] *"Fisheries and Aquaculture."* [Online]. Available: https://www.fao.org/fishery/en/aquaculture. [Accessed: 22-Feb-2023].

[2] FAO, *"In Brief to The State of World Fisheries and Aquaculture 2022."* 2022.

[3] DNV, *"Oceans' Future to 2050 - Marine Aquaculture Forecast."* p. 47, 2021.

[4] M. Føre et al., *"Precision fish farming: A new framework to improve production in aquaculture."* Biosyst. Eng., vol. 173, pp. 176–193, 2018.

[5] B. Morro et al., *"Offshore aquaculture of finfish: Big expectations at sea."* Rev. Aquac., vol. 14, no. 2, pp. 791–815, 2022.

[6] FAO, *In Brief to The State of World Fisheries and Aquaculture 2022.* 2022.

[7] *"10 Pros and Cons of Aquaculture."* [Online]. Available: https://www.resonanceglobal.com/blog/pros-and-cons-of-aquaculture. [Accessed: 21-Feb-2023].

[8] *"Could offshore aquaculture make fish farming more sustainable?"* [Online]. Available: https://qz.com/could-offshore-aquaculture-make-fish-farming-more-susta-1849366981. [Accessed: 21-Feb-2023].

[9] C. Sanz-Lazaro, N. Casado-Coy, E. M. Calderero, and U. A. Villamar, *"The environmental effect on the seabed of an offshore marine fish farm in the tropical Pacific."* J. Environ. Manage., vol. 300, no. September, 2021.

[10] I. El-Thalji, *"Context analysis of Offshore Fish Farming."* IOP Conf. Ser. Mater. Sci. Eng., vol. 700, no. 1, 2019.

[11] *"Cage culture in Aquaculture — Vikaspedia."* [Online]. Available: https://vikaspedia.in/agriculture/fisheries/fish-production/culture-fisheries/types-of-aquaculture/cage-culture-in-aquaculture. [Accessed: 23-Feb-2023].

[12] Z. Liu, S. Wang, and C. G. Soares, *"Numerical Study on the Mooring Force in an Offshore Fish Cage Array."* J. Mar. Sci. Eng., vol. 10, no. 3, 2022.

[13] M. Sievers et al., *"Submerged cage aquaculture of marine fish: A review of the biological challenges and opportunities."* Rev. Aquac., vol. 14, no. 1, pp. 106–119, 2022.

[14] I. Christensen, *"Nets for offshore mariculture."* Options Méditerranéennes Série B. Etudes Rech. n. 30, vol. 178, pp. 173–178, 2000.

[15] C. Farming et al., *"Comparision of Copper Alloy Mesh with Conventional Nylon Nets in Offshore Comparision of Copper Alloy Mesh with Conventional Nylon Nets in Offshore Cage Farming of Gilthead Seabream (Sparus aurata)."* no. July, 2018.

[16] *"Salmon - ASC International."* [Online]. Available: https://asc-aqua.org/learn-about-seafood-farming/farmed-salmon/. [Accessed: 26-May-2023].

[17] *"How salmon is raised: know its benefits and harms."* [Online]. Available: https://agrotendencia.tv/agropedia/acuicultura/el-cultivo-del-salmon/. [Accessed: 27-May-2023].

[18] M. Jones, *"FAO Culture Aquatic Species Fact Sheets: Salmo Salar."* 2009.

[19] *"Division of Marine Fisheries — Mass.gov."* [Online]. Available: https://www.mass.gov/orgs/division-of-marine-fisheries. [Accessed: 27-May-2023].

[20] *"CO-OPS Map - NOAA Tides & Currents."* [Online]. Available: https://tidesandcurrents.noaa.gov/map/index.html. [Accessed: 26-May-2023].

[21] Y. Il Chu et al., *"Offshore Fish Farms: A Review of Standards and Guidelines for Design and Analysis."* J. Mar. Sci. Eng., vol. 11, no. 4, 2023.

[22] I. Tsukrov, A. Drach, J. Decew, M. R. Swift, and B. Celikkol, *"Characterization of geometry and normal drag coefficients of copper nets."* Ocean Eng., vol. 38, no. 17–18, pp. 1979–1988, 2011.

[23] P. Lader, B. Enerhaug, A. Fredheim, P. Klebert, and B. Pettersen, "Forces on a cruciform/sphere structure in uniform current." Ocean Eng., vol. 82, pp. 180–190, 2014.

[24] B. R. Munson, D. F. Young, T. H. Okiishi, and W. W. Huebsch, *"Fundamentals of Fluid Mechanics."* Sixth Edit. Don Fowley.

[25] T. Kristiansen and O. M. Faltinsen, *"Modelling of current loads on aquaculture net cages."* J. Fluids Struct., vol. 34, pp. 218–235, 2012.

[26] A. J. V., R. H., and L. G., *"Current forces on cage, net deflection."* MARINTEK, pp. 137–152, 1990.

[27] H. Tang, F. Hu, L. Xu, and S. Dong, *"Variations in hydrodynamic characteristics of netting panels with various twine materials , knot types , and weave patterns at small attack angles."* no. February, 2019.

[28] M. Sistiaga, B. Herrmann, E. Forås, K. Frank, and L. M. Sunde, *"Prediction of size-dependent risk of salmon smolt (Salmo salar) escape through fish farm nets."* Aquac. Eng., vol. 89, no. April 2019, p. 102061, 2020.

[29] M. A. Mjåtveit, H. Cheng, M. C. Ong, and J. Lee, *"Comparative study of circular and square gravity-based fish cages with different dimensions under pure current conditions."* Aquac. Eng., vol. 96, no. December 2021, p. 102223, 2022.

[30] L. C. Gansel et al., *"Drag of Clean and Fouled Net Panels–Measurements and Parameterization of Fouling."* PLoS One, vol. 10, no. 7, p. e0131051, 2015.

[31] P. R. Spalart, and S. R. Allmaras, *"One-equation turbulence model for aerodynamic flows."* Rech. Aerosp., no. 1, pp. 5–21, 1994.

[32] "Fluid dynamics Tdyn CFD+HT - Consultancy for design in engineering." [Online]. Available: https://www.compassis.com/en/software/fluid-dynamics-tdyn-cfdht/. [Accessed: 20-Jul-2023].

[33] Compass, *"Turbulence Handbook for Tdyn."* p. 42, 2017.

[34] Y. Cengel, and J. Cimbala, *"Fluid Mechanics Fundamentals and Applications."* 2014.

[35] International Towing Tank Conference, *"ITTC - Recommended Procedures. Fresh Water and Seawater Properties."* 2011.

[36] *"Courant number in CFD - IdealSimulations."* [Online]. Available: https://www.idealsimulations.com/resources/courant-number-cfd/. [Accessed: 04-Jun-2023].

[37] *"Cage and Pen fish farming."* [Online]. Available: https://www.fao.org/3/AD021E/AD021E01.htm. [Accessed: 10-Jun-2023].

[38] *"China's first deep-sea fish farming facility, Shenlan 1 - CGTN."* [Online]. Available: https://news.cgtn.com/news/3d3d674d7a55544e78457a6333566d54/index.html. [Accessed: 10-Jun-2023].

[39] G. Wang, T. Martin, L. Huang, and H. Bihs, *"A Numerical Study of the Hydrodynamics of an Offshore Fish Farm Using REEF3D."* J. Offshore Mech. Arct. Eng., vol. 144, no. 2, pp. 1–10, 2022.

[40] MSL Engineering Limited, *"Appraisal of API RP 2FPS (Recommended practice for planning, designing and constructing floating production systems)."* Uk Hse Offshore Technol. Rep. 2001/006, no. March, 2001.

[41] "Structural analysis - Tdyn RamSeries - Consultancy for design in engineering." [Online]. Available: https://www.compassis.com/en/software/structural-analysis-tdyn-ramseries/. [Accessed: 20-Jul-2023].

[42] "TDYN SEAFEM Seakeeping - Consultancy for design in engineering." [Online]. Available: https://www.compassis.com/en/software/seakeeping-tdyn-seafem/. [Accessed: 20-Jul-2023].

[43] N. N. W. S. US Department of Commerce, *"Beaufort Scale."*

[44] *"CZM Seafloor and Habitat Mapping - Sediment Mapping — Mass.gov."* [Online]. Available: https://www.mass.gov/service-details/czm-seafloor-and-habitat-mapping-sediment-mapping. [Accessed: 19-Jun-2023].

[45] H.-J. Cho, *"Offshore Mooring Chain and Achor Chain Catalogue."* p. 20, 2013.

[46] Compass, *"SeaFEM Reference Manual."*

[47] M. McCormick, *"Ocean Engineering Mechanics."* 1st Edition. Cambridge University Press, 2010.

[48] A. Bureau, *Requirements for Position Mooring Systems."* no. February, 2023.

[49] *"Massachusetts Bay Ships Marine Traffic Live Map — ShipTraffic.net."* [Online]. Available: http://www.shiptraffic.net/marine-traffic/bays/Massachusetts-Bay. [Accessed: 01-Jul-2023].

Chapter 8

Appendix: CFD Analysis Results

Speed (m/s)	Domain Length (m)	Simulation Time (s)	dh (mm)	dt (s)	nsteps
0.35	0.375	1.0714	0.37	0.0011	1500
0.5	0.375	0.7500	0.37	0.0007	1500
0.65	0.375	0.5769	0.37	0.0006	1500

Table 8.1: *Timestep and Simulation time for Square and Hexagonal Nets 13-2.*

Speed (m/s)	Domain Length (m)	Simulation Time (s)	dh (mm)	dt (s)	nsteps
0.35	0.525	1.5000	0.46	0.0013	1500
0.5	0.525	1.0500	0.46	0.0009	1500
0.65	0.525	0.8077	0.46	0.0007	1500

Table 8.2: *Timestep and Simulation time for Square and Hexagonal Nets 17-3.*

Mesh Convergence	Elements	Domain	Subdomain1	Subdomain2	Net	Drag Max (N)	ER%
Mesh 1	343729	160	100	60	1	0.1771	
Mesh 2	979665	80	40	20	1	0.2117	16.34%
Mesh 3	1641244	70	30	15	1	0.2037	3.93%

Table 8.3: *Mesh Convergence results for Experimental CFD Validation (0.2 m/s).*

Mesh Convergence	Elements	Domain	Subdomain1	Subdomain2	Net	Drag Max (N)	ER%
Mesh 1	292860	160	100	60	1	0.545	
Mesh 2	972239	80	40	20	1	0.8173	33.32%
Mesh 3	1642091	70	30	15	1	0.8133	0.49%

Table 8.4: *Mesh Convergence results for Experimental CFD Validation (0.4 m/s).*

Mesh Convergence	Elements	Domain	Subdomain1	Subdomain2	Net	Drag Max (N)	ER%
Mesh 1	116081	65	45	30	0.37	0.0324	
Mesh 2	335900	30	15	8	0.37	0.0347	6.63%
Mesh 3	592110	15	10	5	0.37	0.03339	3.92%

Table 8.5: *Mesh Convergence results for Square Net Panel 15-2 (0.35 m/s).*

Mesh Convergence	Elements	Domain	Subdomain1	Subdomain2	Net	Drag Max (N)	ER%
Mesh 1	116081	65	45	30	0.37	0.0649	
Mesh 2	335900	30	15	8	0.37	0.06791	4.43%
Mesh 3	790745	15	8	3	0.37	0.06763	0.41%

Table 8.6: *Mesh Convergence results for Square Net Panel 15-2 (0.50 m/s).*

Mesh Convergence	Elements	Domain	Subdomain1	Subdomain2	Net	Drag Max (N)	ER%
Mesh 1	116081	65	45	30	0.37	0.1101	
Mesh 2	335900	30	15	8	0.37	0.1138	3.25%
Mesh 3	790745	15	8	3	0.37	0.1132	0.53%

Table 8.7: *Mesh Convergence results for Square Net Panel 15-2 (0.65 m/s).*

Mesh Convergence	Elements	Domain	Subdomain1	Subdomain2	Net	Drag Max (N)	ER%
Mesh 1	109899	65	45	30	0.37	0.02451	
Mesh 2	357403	30	15	8	0.37	0.02887	15.10%
Mesh 3	832171	15	8	3	0.37	0.02876	0.38%

Table 8.8: *Mesh Convergence results for Hexagonal Net Panel 15-2 (0.35 m/s).*

Mesh Convergence	Elements	Domain	Subdomain1	Subdomain2	Net	Drag Max (N)	ER%
Mesh 1	109899	65	45	30	0.37	0.04784	
Mesh 2	357403	30	15	8	0.37	0.05503	13.07%
Mesh 3	832171	15	8	3	0.37	0.05476	0.49%

Table 8.9: *Mesh Convergence results for Hexagonal Net Panel 15-2 (0.50 m/s).*

Mesh Convergence	Elements	Domain	Subdomain1	Subdomain2	Net	Drag Max (N)	ER%
Mesh 1	102878	57	40	26.5	0.37	0.02937	
Mesh 2	305493	26.5	13	7	0.37	0.03102	5.32%
Mesh 3	908664	13	7	2.5	0.37	0.03072	0.98%

Table 8.10: *Mesh Convergence results for Square Net Panel 13-2 (0.35 m/s).*

Mesh Convergence	Elements	Domain	Subdomain1	Subdomain2	Net	Drag Max (N)	ER%
Mesh 1	102878	57	40	26.5	0.37	0.05875	
Mesh 2	305493	26.5	13	7	0.37	0.06087	3.48%
Mesh 3	908664	13	7	2.5	0.37	0.06019	1.13%

Table 8.11: *Mesh Convergence results for Square Net Panel 13-2 (0.50 m/s).*

Mesh Convergence	Elements	Domain	Subdomain1	Subdomain2	Net	Drag Max (N)	ER%
Mesh 1	102878	57	40	26.5	0.37	0.09962	
Mesh 2	305493	26.5	13	7	0.37	0.102	2.33%
Mesh 3	908664	13	7	2.5	0.37	0.1008	1.19%

Table 8.12: *Mesh Convergence results for Square Net Panel 13-2 (0.65 m/s).*

Mesh Convergence	Elements	Domain	Subdomain1	Subdomain2	Net	Drag Max (N)	ER%
Mesh 1	92054	57	40	26.5	0.37	0.02551	
Mesh 2	287233	26.5	13	7	0.37	0.02803	8.99%
Mesh 3	891449	13	7	2.5	0.37	0.02789	0.50%

Table 8.13: *Mesh Convergence results for Hexagonal Net Panel 13-2 (0.35 m/s).*

Mesh Convergence	Elements	Domain	Subdomain1	Subdomain2	Net	Drag Max (N)	ER%
Mesh 1	92054	57	40	26.5	0.37	0.05089	
Mesh 2	287233	26.5	13	7	0.37	0.05475	7.05%
Mesh 3	891449	13	7	2.5	0.37	0.05466	0.16%

Table 8.14: *Mesh Convergence results for Hexagonal Net Panel 13-2 (0.50 m/s).*

Mesh Convergence	Elements	Domain	Subdomain1	Subdomain2	Net	Drag Max (N)	ER%
Mesh 1	92054	57	40	26.5	0.37	0.08644	
Mesh 2	287233	26.5	13	7	0.37	0.09175	5.79%
Mesh 3	891449	13	7	2.5	0.37	0.09155	0.22%

Table 8.15: *Mesh Convergence results for Hexagonal Net Panel 13-2 (0.65 m/s).*

Mesh Convergence	Elements	Domain	Subdomain1	Subdomain2	Net	Drag Max (N)	ER%
Mesh 1	131195	80	55.5	37	0.46	0.06107	
Mesh 2	369235	37	18.5	10	0.46	0.05995	1.87%
Mesh 3	876906	18.5	9.5	3.5	0.46	0.05981	0.23%

Table 8.16: *Mesh Convergence results for Square Net Panel 17-3 (0.35 m/s).*

Mesh Convergence	Elements	Domain	Subdomain1	Subdomain2	Net	Drag Max (N)	ER%
Mesh 1	131195	80	55.5	37	0.46	0.1223	
Mesh 2	369235	37	18.5	10	0.46	0.1171	4.44%
Mesh 3	876906	18.5	9.5	3.5	0.46	0.1168	0.26%

Table 8.17: *Mesh Convergence results for Square Net Panel 17-3 (0.50 m/s).*

Mesh Convergence	Elements	Domain	Subdomain1	Subdomain2	Net	Drag Max (N)	ER%
Mesh 1	131195	80	55.5	37	0.46	0.2055	
Mesh 2	369235	37	18.5	10	0.46	0.1949	5.41%
Mesh 3	876906	18.5	9.5	3.5	0.46	0.1943	0.31%

Table 8.18: *Mesh Convergence results for Square Net Panel 17-3 (0.65 m/s).*

Mesh Convergence	Elements	Domain	Subdomain1	Subdomain2	Net	Drag Max (N)	ER%
Mesh 1	129722	80	55.5	37	0.46	0.05981	
Mesh 2	368258	37	18.5	10	0.46	0.06175	3.14%
Mesh 3	874181	18.5	9.5	3.5	0.46	0.06109	1.08%

Table 8.19: *Mesh Convergence results for Hexagonal Net Panel 17-3 (0.35 m/s).*

Mesh Convergence	Elements	Domain	Subdomain1	Subdomain2	Net	Drag Max (N)	ER%
Mesh 1	129722	80	55.5	37	0.46	0.1193	
Mesh 2	368258	37	18.5	10	0.46	0.121	1.40%
Mesh 3	874181	18.5	9.5	3.5	0.46	0.1196	1.17%

Table 8.20: *Mesh Convergence results for Hexagonal Net Panel 17-3 (0.50 m/s).*

Mesh Convergence	Elements	Domain	Subdomain1	Subdomain2	Net	Drag Max (N)	ER%
Mesh 1	129722	80	55.5	37	0.46	0.2012	
Mesh 2	368258	37	18.5	10	0.46	0.2015	0.15%
Mesh 3	874181	18.5	9.5	3.5	0.46	0.1989	1.31%

Table 8.21: *Mesh Convergence results for Hexagonal Net Panel 17-3 (0.65 m/s).*
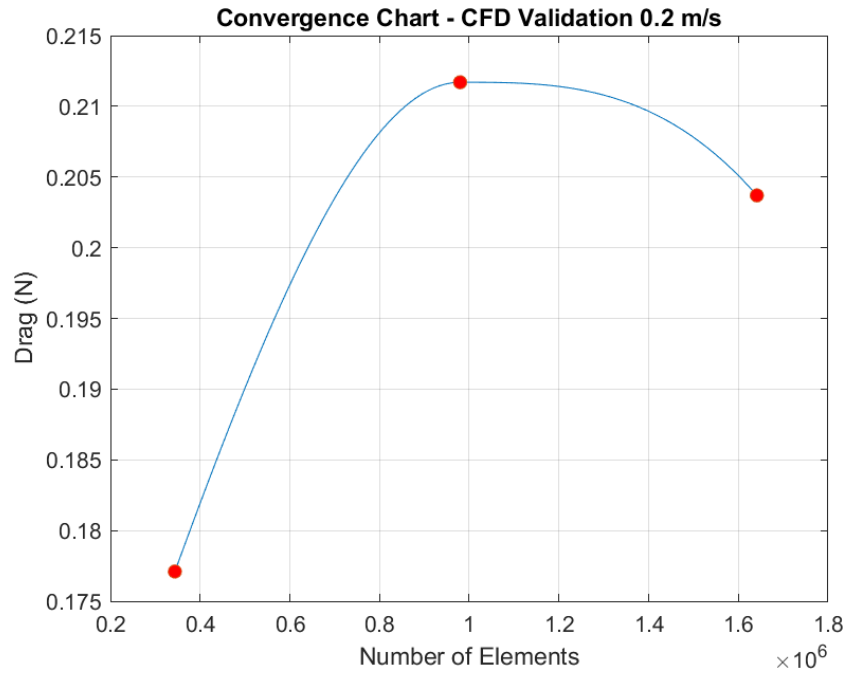
Figure 8.1: *Mesh Convergence Chart for Experimental CFD Validation (0.2 m/s).*
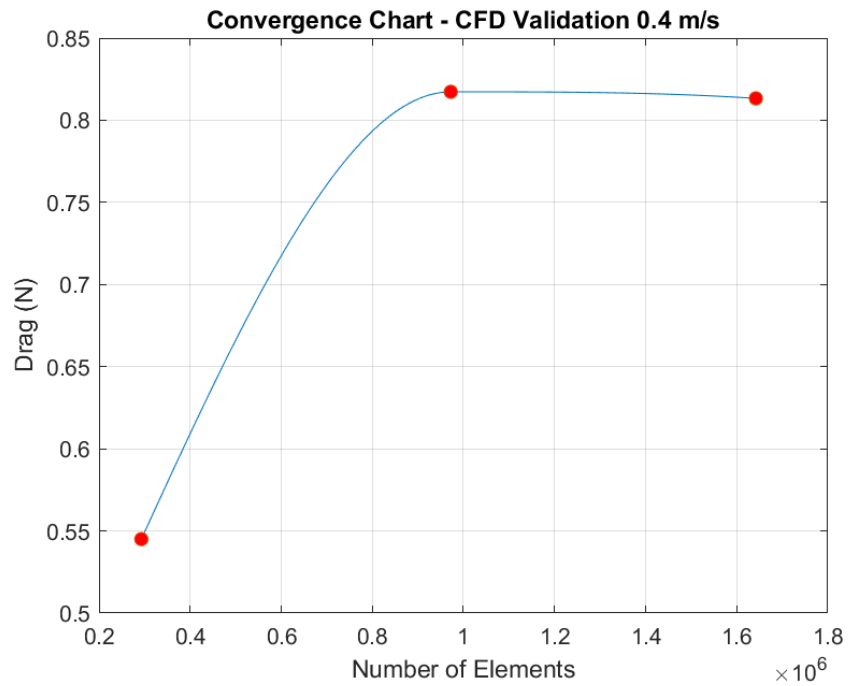
Figure 8.2: *Mesh Convergence Chart for Experimental CFD Validation (0.4 m/s).*
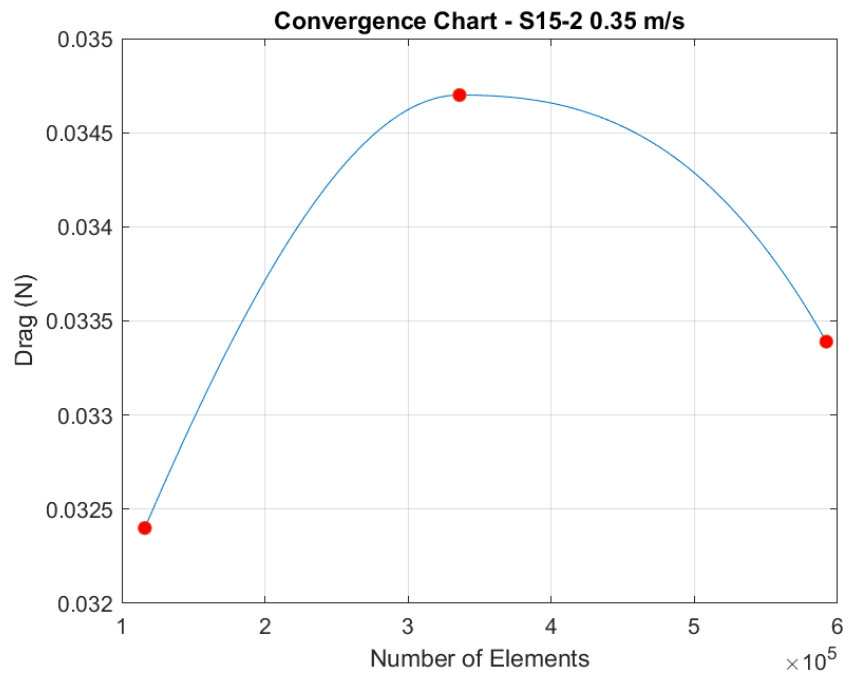
Figure 8.3: *Mesh Convergence Chart for Square Net Panel 15-2 (0.35 m/s).*
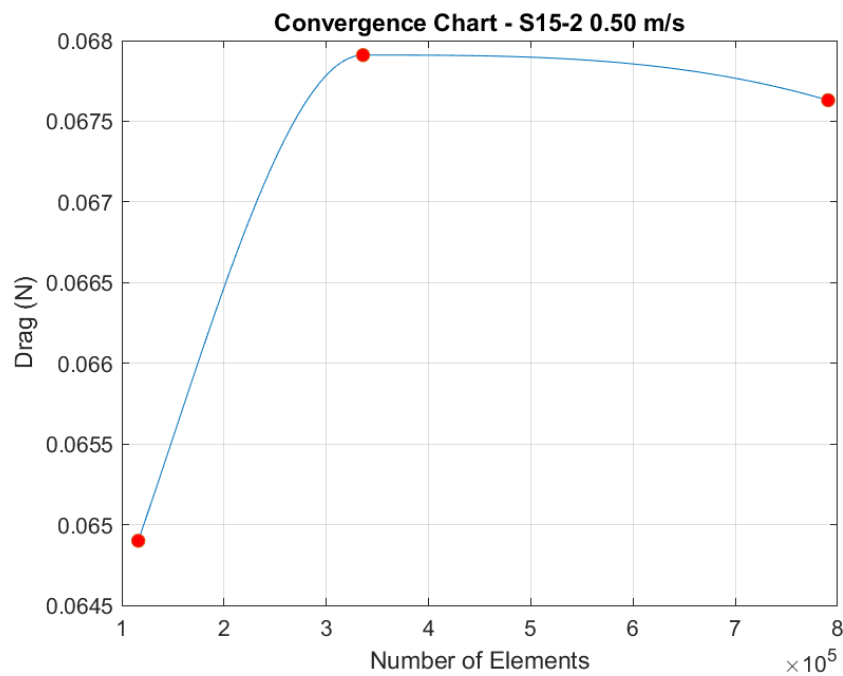
Figure 8.4: *Mesh Convergence Chart for Square Net Panel 15-2 (0.50 m/s).*
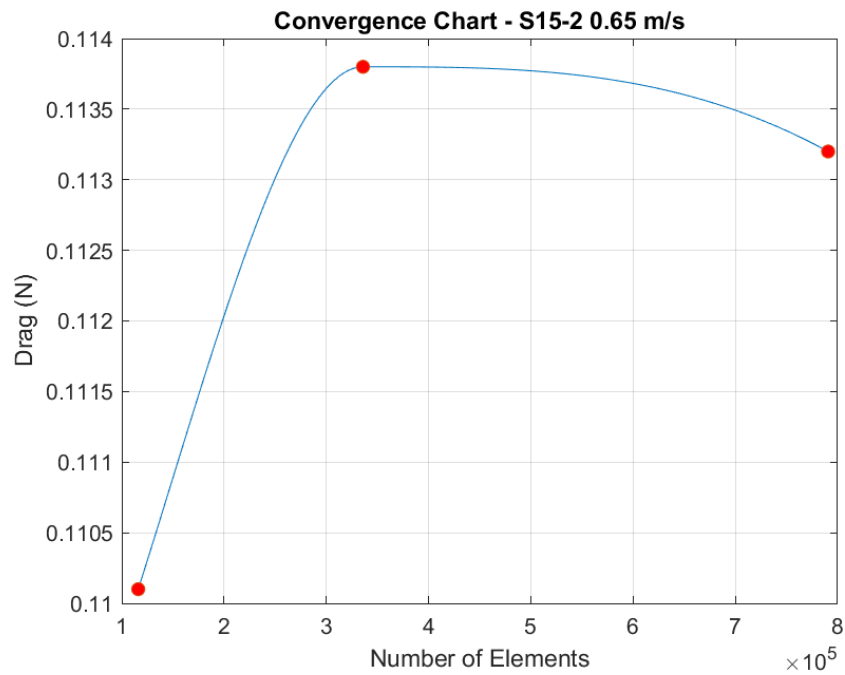
Figure 8.5: *Mesh Convergence Chart for Square Net Panel 15-2 (0.65 m/s).*
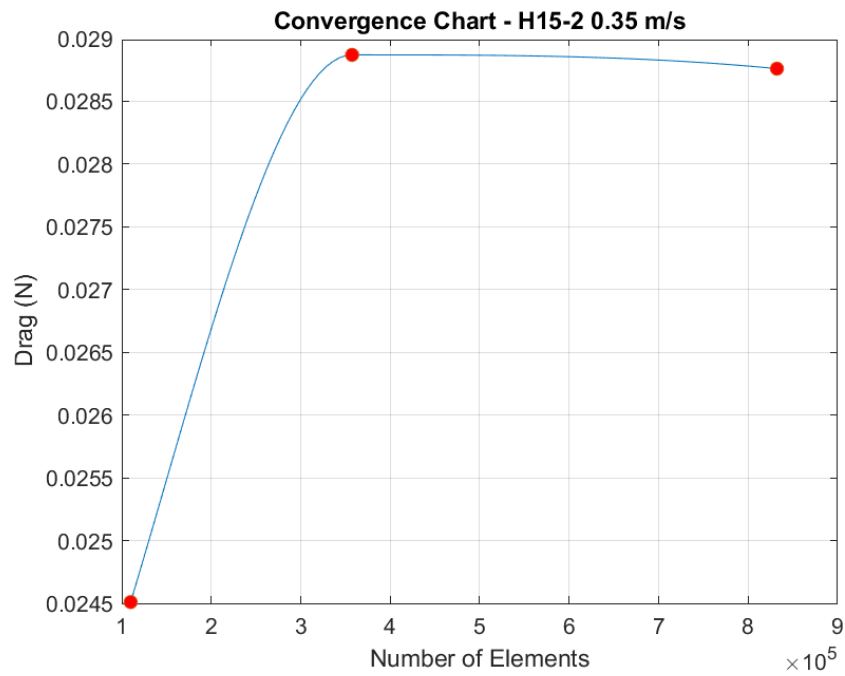
Figure 8.6: *Mesh Convergence Chart for Hexagonal Net Panel 15-2 (0.35 m/s).*
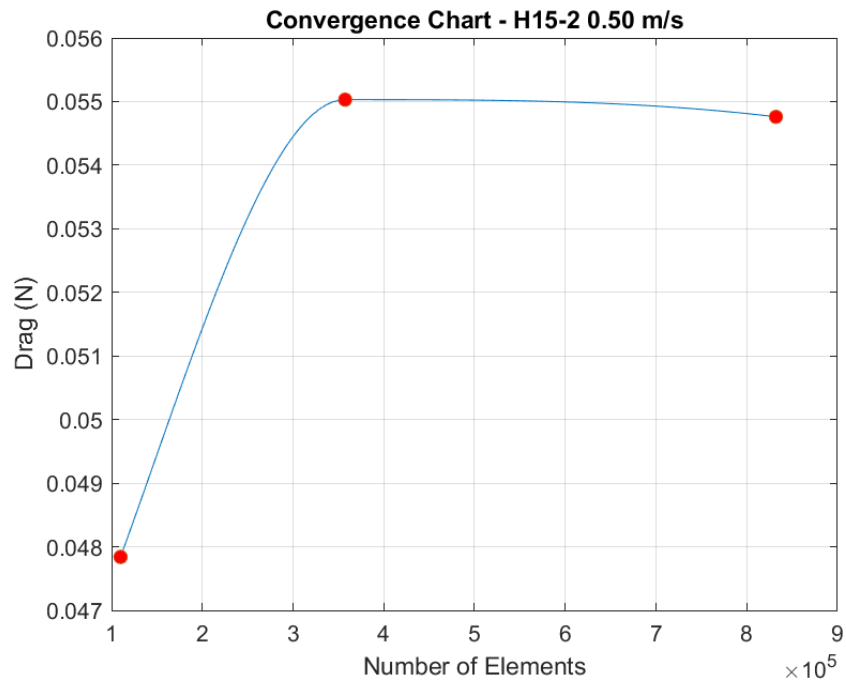
Figure 8.7: *Mesh Convergence Chart for Hexagonal Net Panel 15-2 (0.50 m/s).*
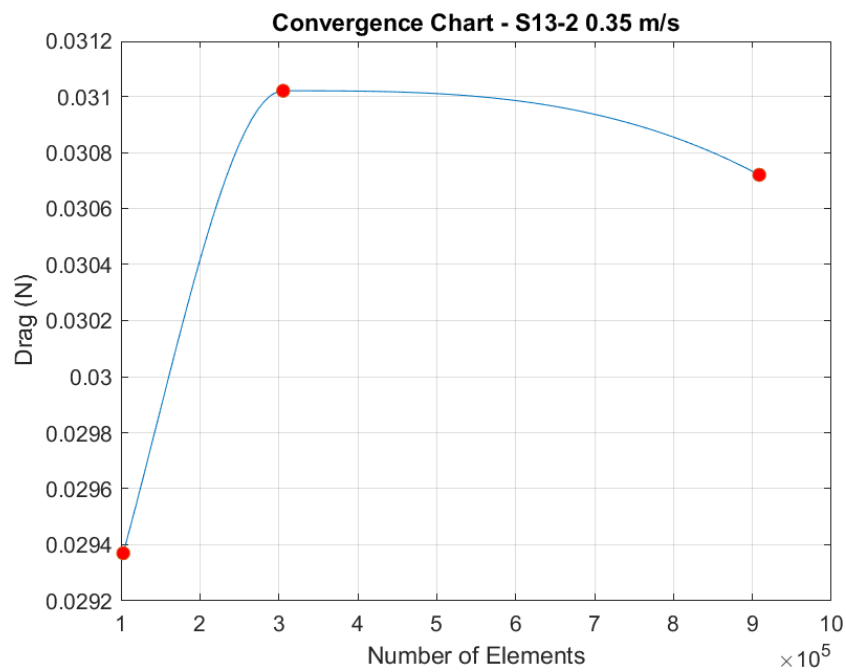
Figure 8.8: *Mesh Convergence Chart for Square Net Panel 13-2 (0.35 m/s).*
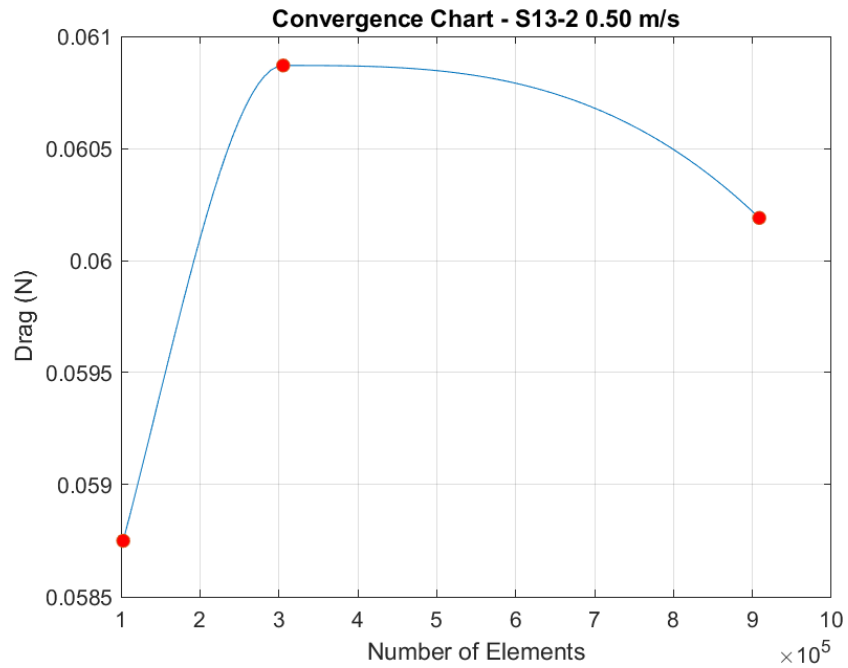
Figure 8.9: *Mesh Convergence Chart for Square Net Panel 13-2 (0.50 m/s).*
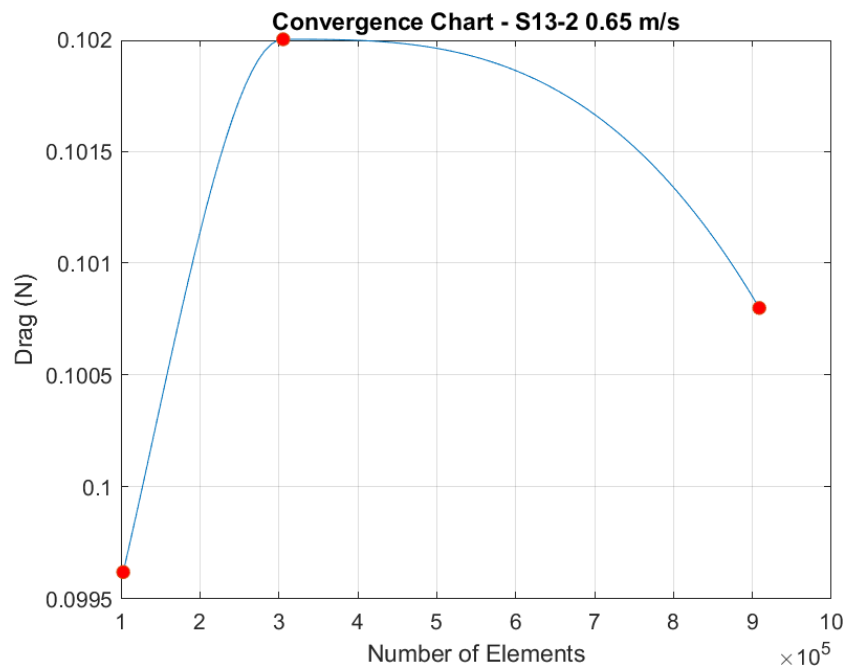
Figure 8.10: *Mesh Convergence Chart for Square Net Panel 13-2 (0.65 m/s).*
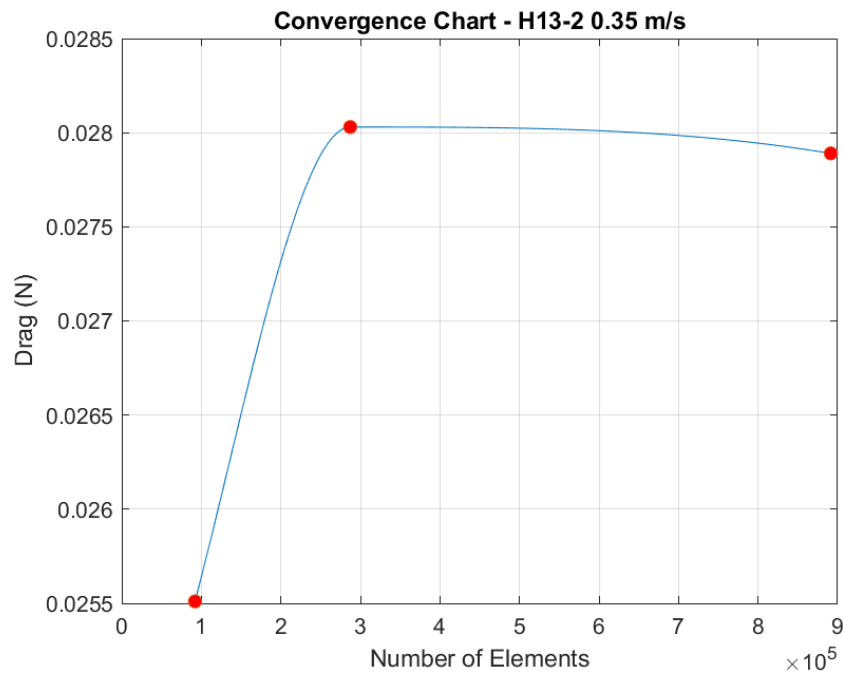
Figure 8.11: *Mesh Convergence Chart for Hexagonal Net Panel 13-2 (0.35 m/s).*
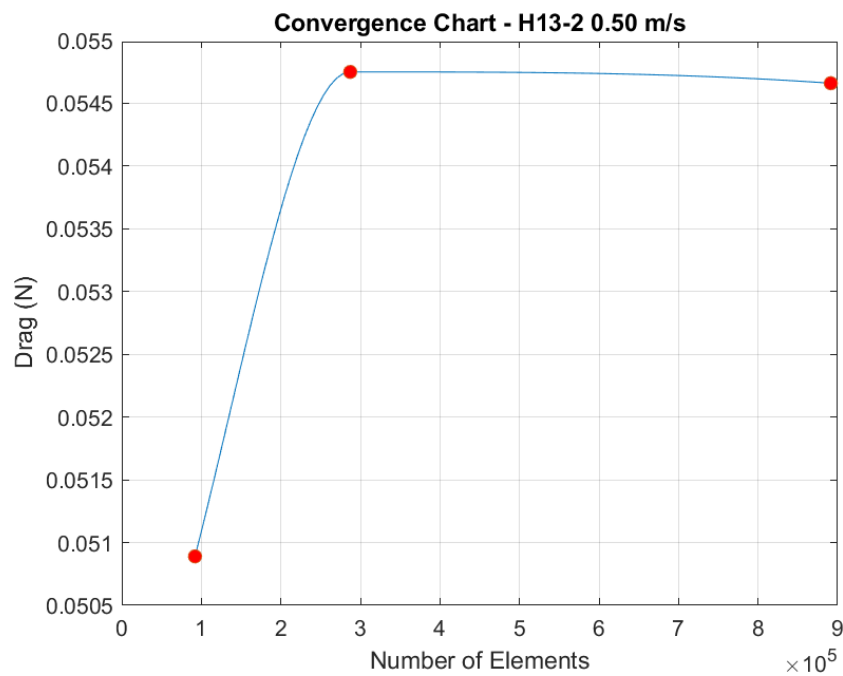
Figure 8.12: *Mesh Convergence Chart for Hexagonal Net Panel 13-2 (0.50 m/s).*
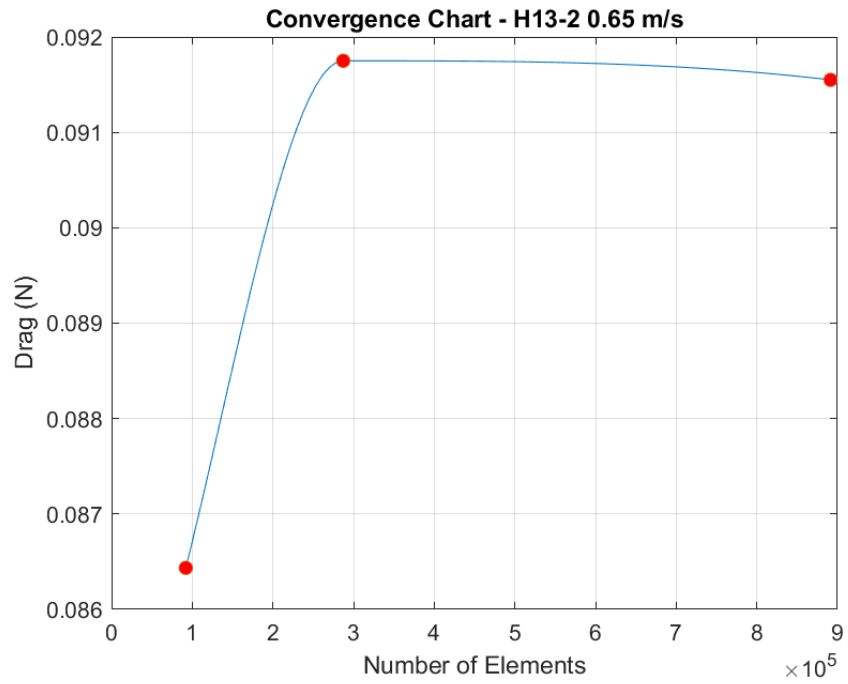
Figure 8.13: *Mesh Convergence Chart for Hexagonal Net Panel 13-2 (0.65 m/s).*
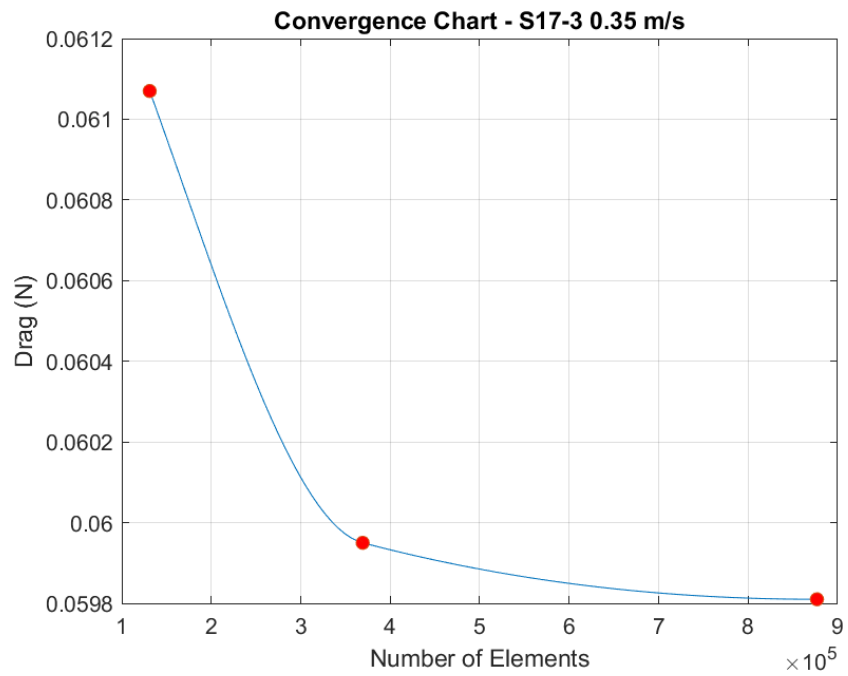
Figure 8.14: *Mesh Convergence Chart for Square Net Panel 17-3 (0.35 m/s).*
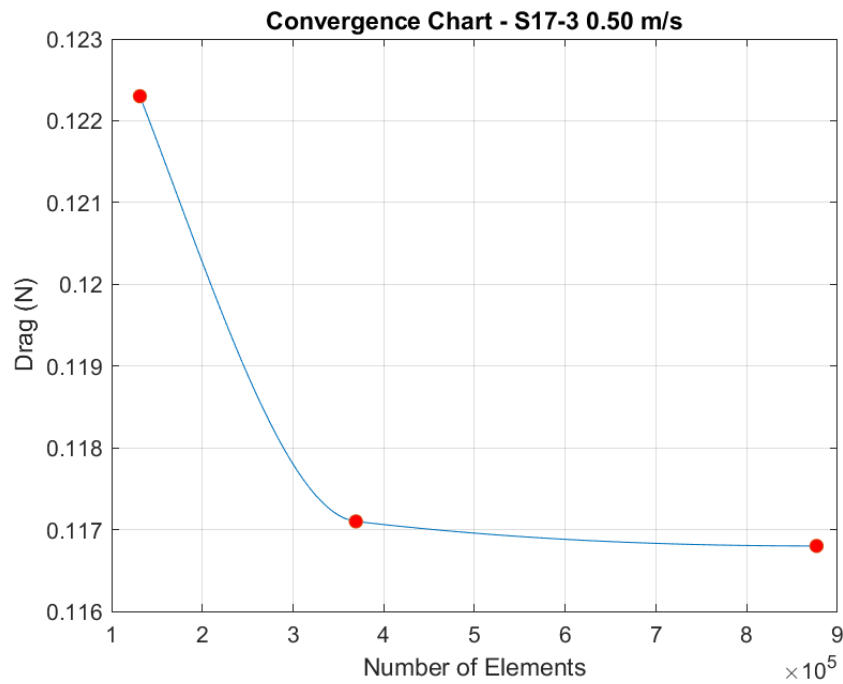
Figure 8.15: *Mesh Convergence Chart for Square Net Panel 17-3 (0.50 m/s).*
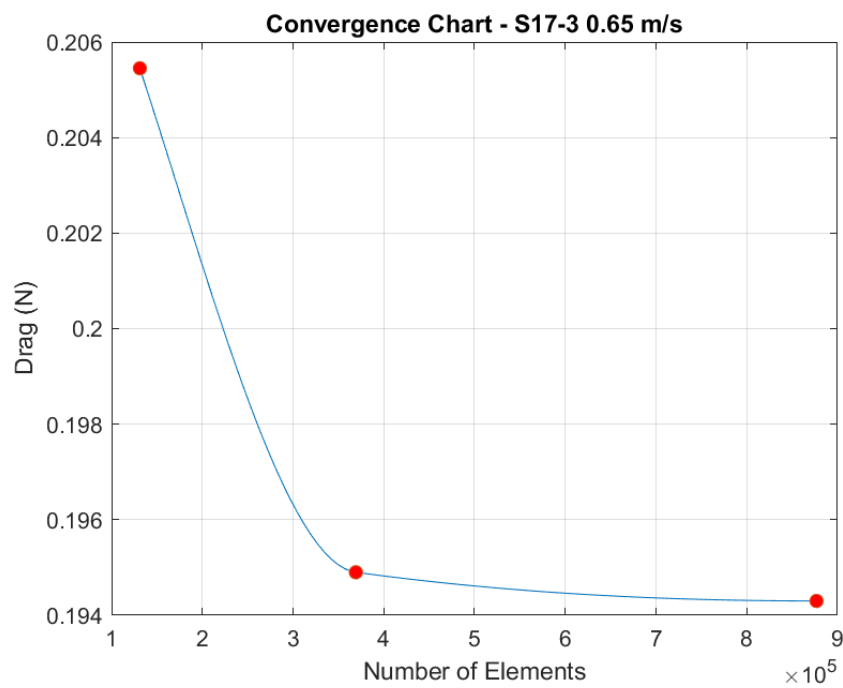
Figure 8.16: *Mesh Convergence Chart for Square Net Panel 17-3 (0.65 m/s).*
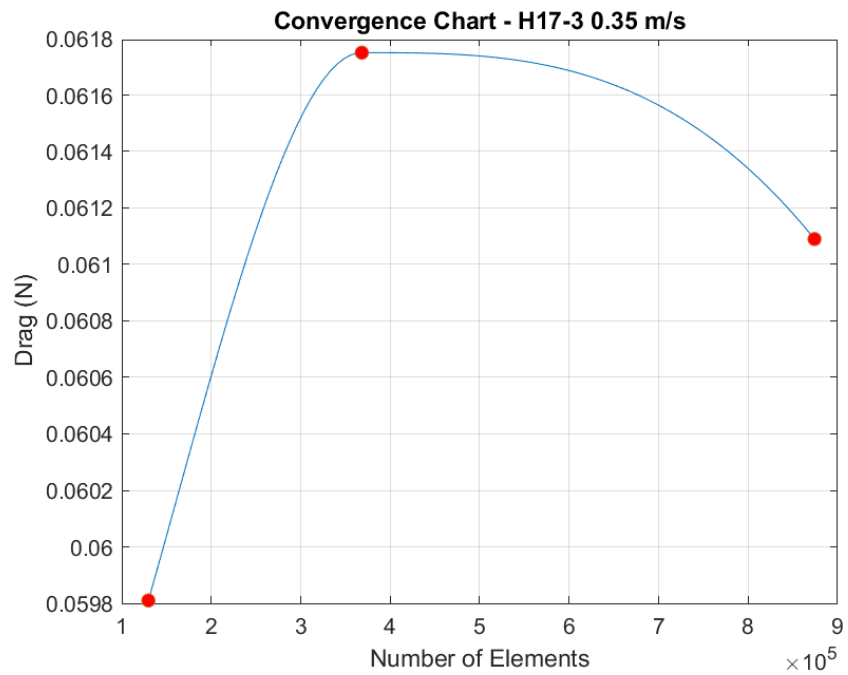
Figure 8.17: *Mesh Convergence Chart for Hexagonal Net Panel 17-3 (0.35 m/s).*
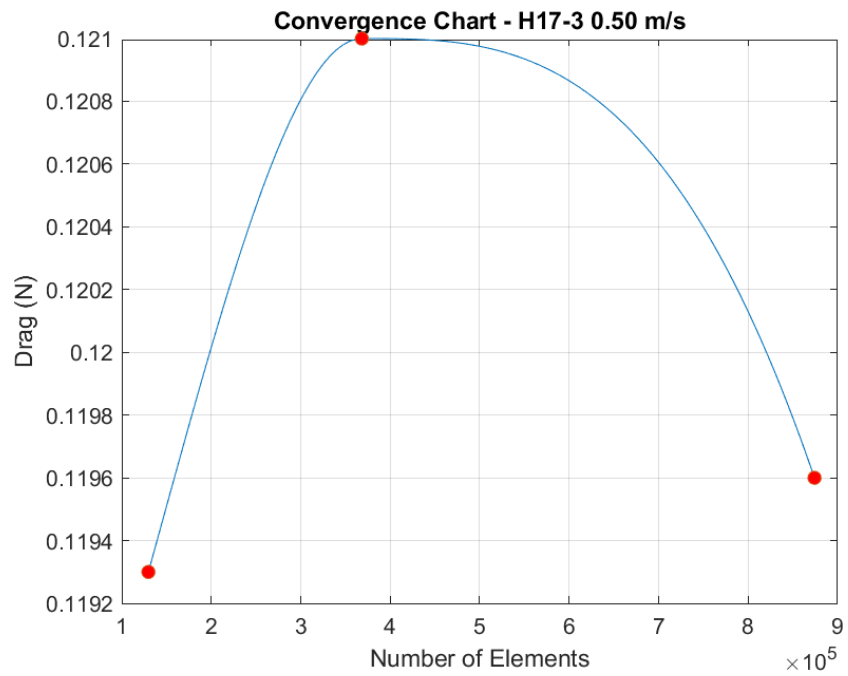
Figure 8.18: *Mesh Convergence Chart for Hexagonal Net Panel 17-3 (0.50 m/s).*
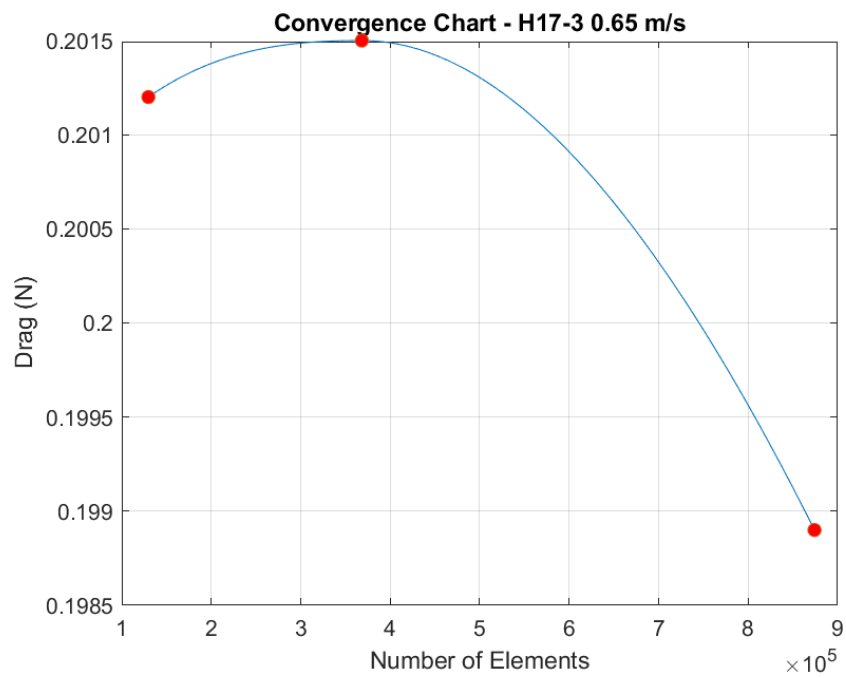
Figure 8.19: *Mesh Convergence Chart for Hexagonal Net Panel 17-3 (0.65 m/s).*

Chapter 9

Appendix: Seakeeping Analysis Results

Element	Inital Coordinates	Final Coordinates
Upper1	-10.5893,-25.8338,0	-10.5893,-25.8338,-7.08275
Upper2	-25.8338,-10.5893,0	-25.8338,-10.5893,-7.08275
Upper3	-25.8338,10.5893,0	-25.8338,10.5893,-7.08275
Upper4	-10.5893,25.8338,0	-10.5893,25.8338,-7.08275
Upper5	10.5893,25.8338,0	10.5893,25.8338,-7.08275
Upper6	25.8338,10.5893,0	25.8338,10.5893,-7.08275
Upper7	25.8338,-10.5893,0	25.8338,-10.5893,-7.08275
Upper8	10.5893,-25.8338,0	10.5893,-25.8338,-7.08275
Lower1	-10.5893,-25.8338,-8.44748	-10.5893,-25.8338,-18.0167
Lower2	-25.8338,-10.5893,-8.44748	-25.8338,-10.5893,-18.0167
Lower3	-25.8338,10.5893,-8.44748	-25.8338,10.5893,-18.0167
Lower4	-10.5893,25.8338,-8.44748	-10.5893,25.8338,-18.0167
Lower5	10.5893,25.8338,-8.44748	10.5893,25.8338,-18.0167
Lower6	25.8338,10.5893,-8.44748	25.8338,10.5893,-18.0167
Lower7	25.8338,-10.5893,-8.44748	25.8338,-10.5893,-18.0167
Lower8	10.5893,-25.8338,-8.44748	10.5893,-25.8338,-18.0167

Table 9.1: *Slender Elements Coordinates.*
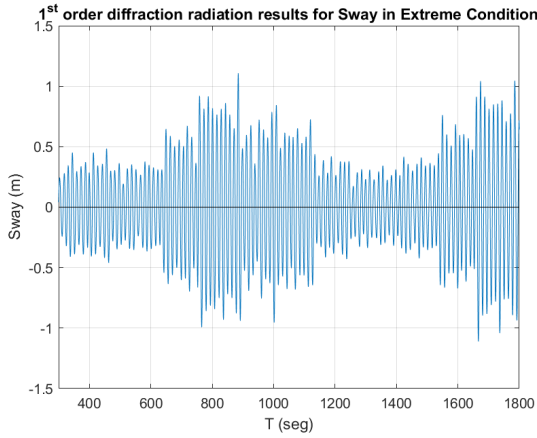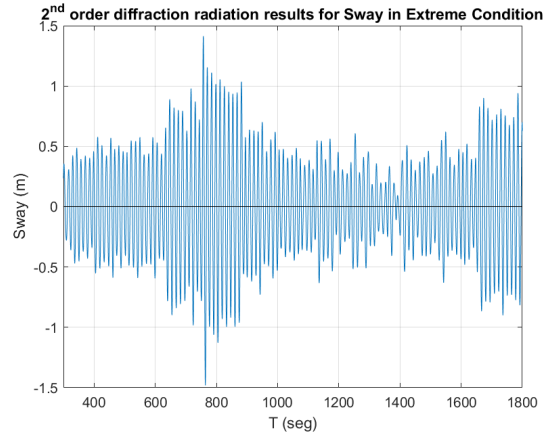
(a) *1ˢᵗ Order Diffraction Radiation.*   (b) *2ⁿᵈ Order Diffraction Radiation.*

Figure 9.1: *Sway Results for Extreme Conditions in a Time-Domain Signal.*
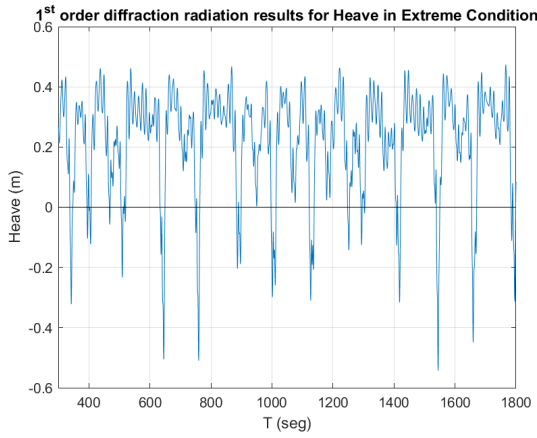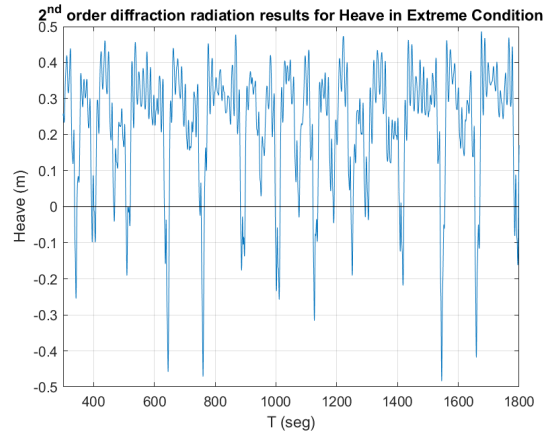
(a) *1ˢᵗ Order Diffraction Radiation.*   (b) *2ⁿᵈ Order Diffraction Radiation.*

Figure 9.2: *Heave Results for Extreme Conditions in a Time-Domain Signal.*
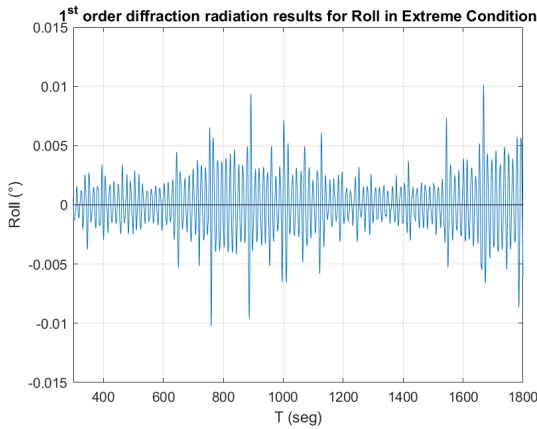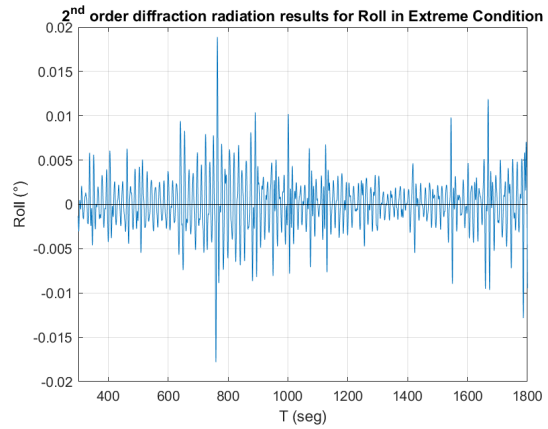
(a) *1ˢᵗ Order Diffraction Radiation.*   (b) *2ⁿᵈ Order Diffraction Radiation.*

Figure 9.3: *Roll Results for Extreme Conditions in a Time-Domain Signal.*
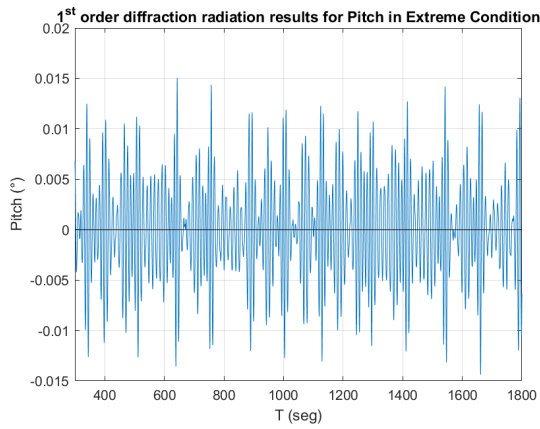
(a) 1st *Order Diffraction Radiation.*
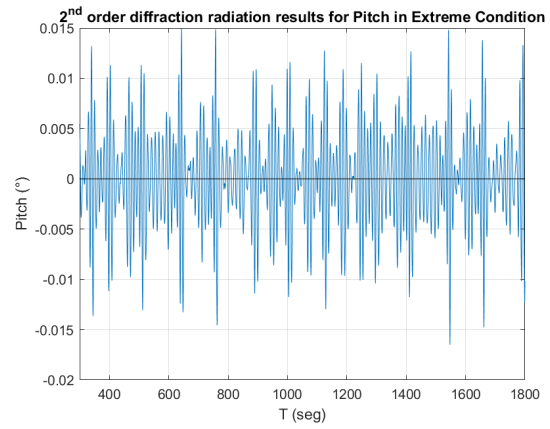
(b) 2nd *Order Diffraction Radiation.*

Figure 9.4: *Pitch Results for Extreme Conditions in a Time-Domain Signal.*
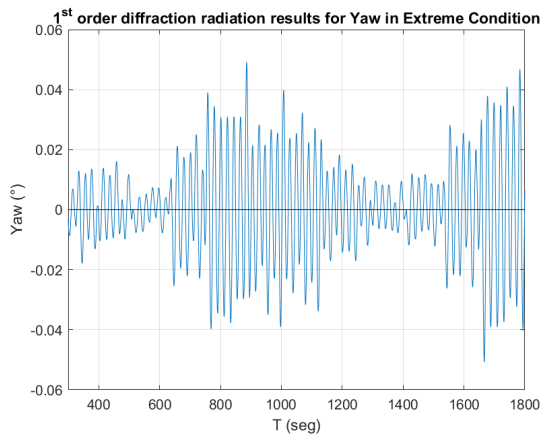
(a) 1st *Order Diffraction Radiation.*
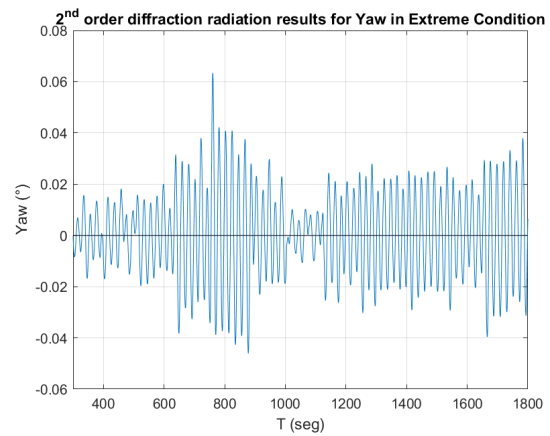
(b) 2nd *Order Diffraction Radiation.*

Figure 9.5: *Yaw Results for Extreme Conditions in a Time-Domain Signal.*
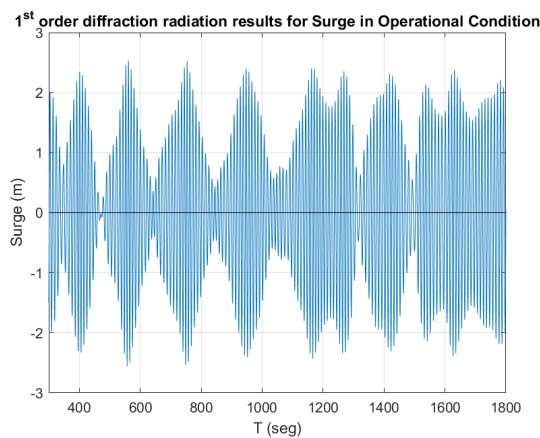
(a) 1st *Order Diffraction Radiation.*
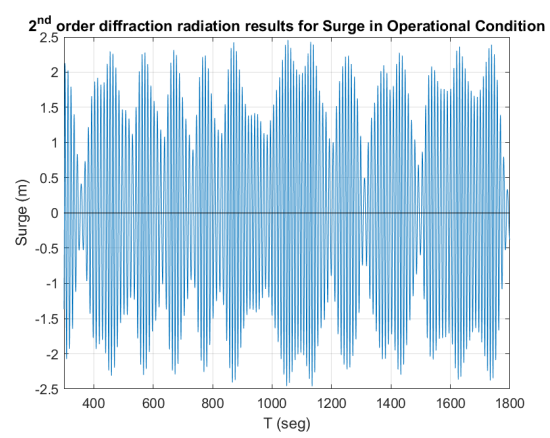
(b) 2nd *Order Diffraction Radiation.*

Figure 9.6: *Surge Results for Operational Conditions in a Time-Domain Signal.*
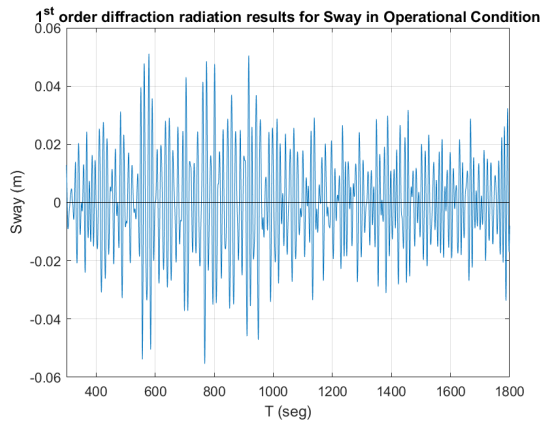
(a) 1st *Order Diffraction Radiation.*
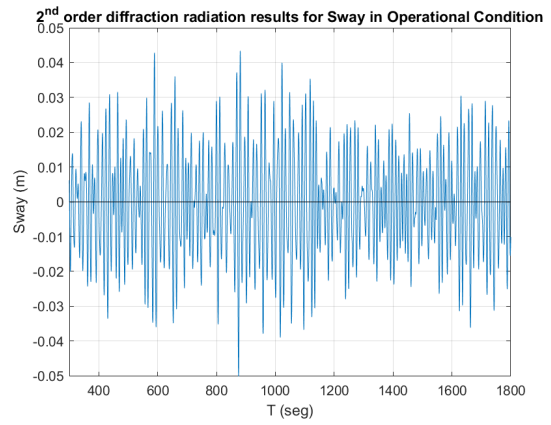
(b) 2nd *Order Diffraction Radiation.*

Figure 9.7: *Sway Results for Operational Conditions in a Time-Domain Signal.*
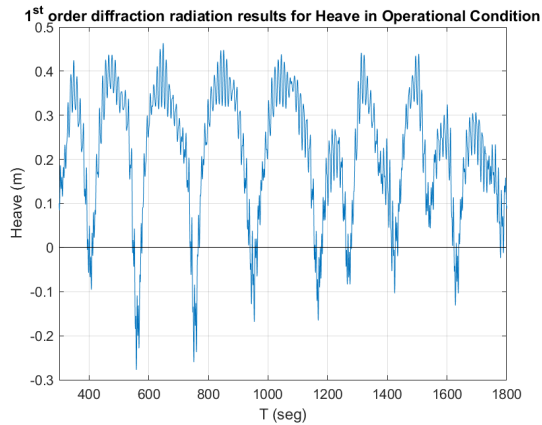
(a) 1st *Order Diffraction Radiation.*
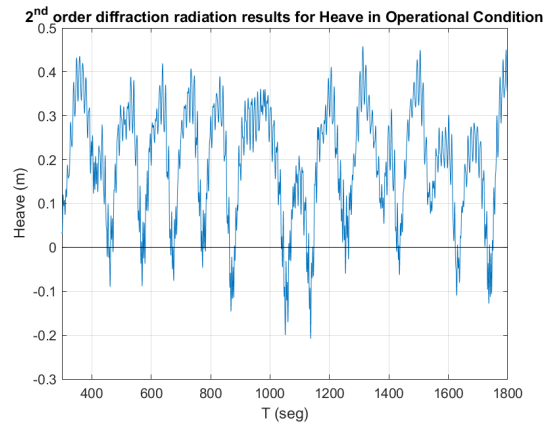
(b) 2nd *Order Diffraction Radiation.*

Figure 9.8: *Heave Results for Operational Conditions in a Time-Domain Signal.*
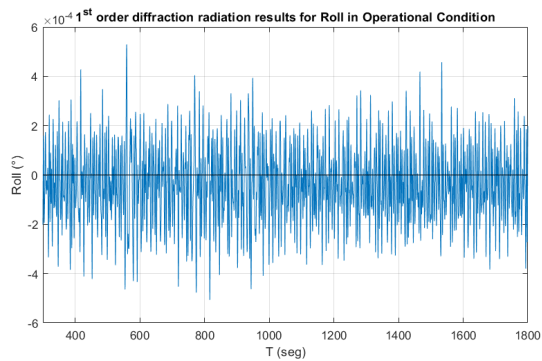
(a) 1st *Order Diffraction Radiation.*
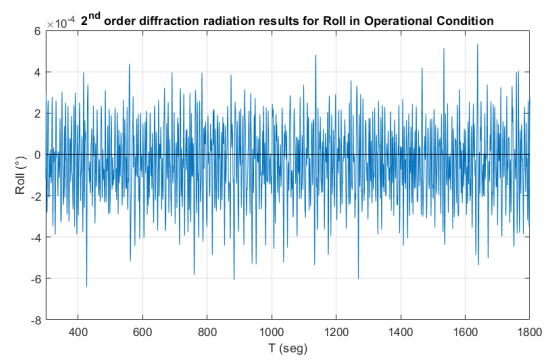
(b) 2nd *Order Diffraction Radiation.*

Figure 9.9: *Roll Results for Operational Conditions in a Time-Domain Signal.*

(a) 1st Order Diffraction Radiation.

(b) 2nd Order Diffraction Radiation.
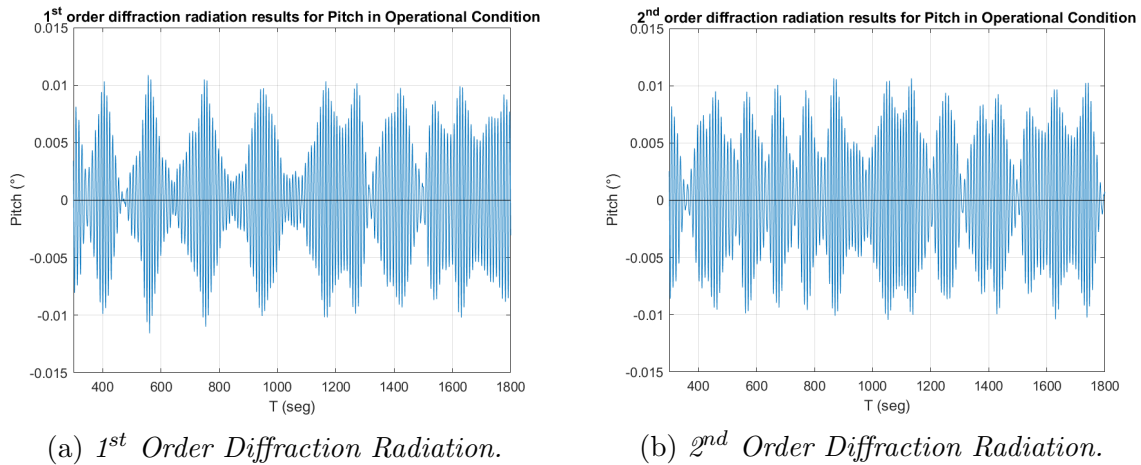
Figure 9.10: *Pitch Results for Operational Conditions in a Time-Domain Signal.*

(a) 1st Order Diffraction Radiation.

(b) 2nd Order Diffraction Radiation.
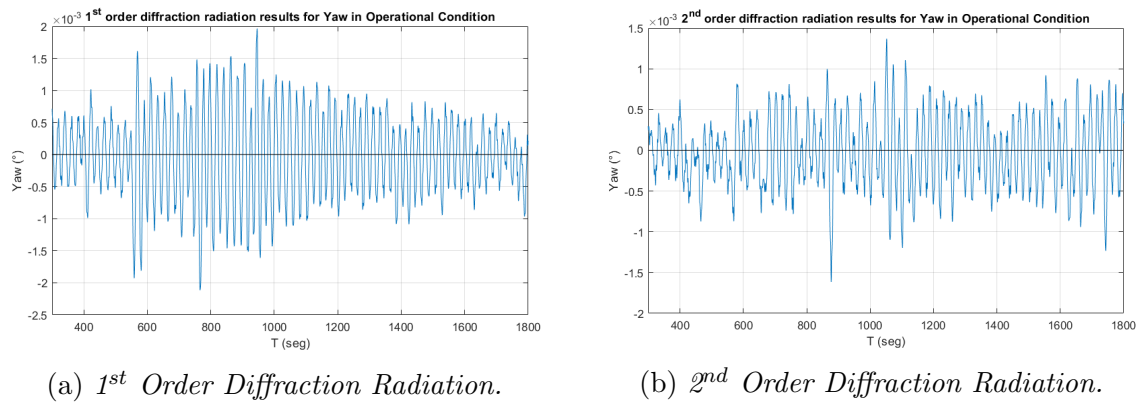
Figure 9.11: *Yaw Results for Operational Conditions in a Time-Domain Signal.*

(a) 1st Order Diffraction Radiation.

(b) 2nd Order Diffraction Radiation.
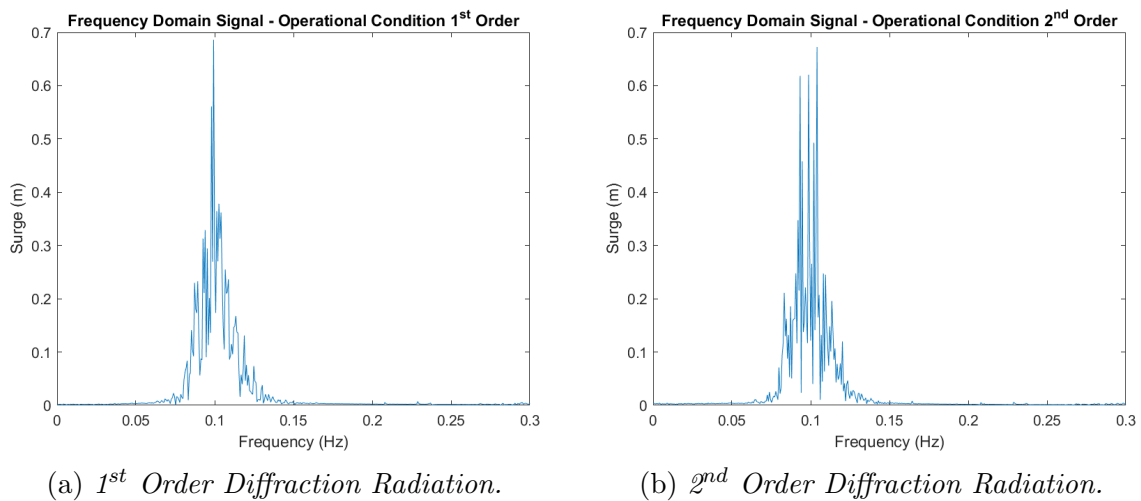
Figure 9.12: *Surge Results for Operational Condition in a Frequency-Domain Signal.*
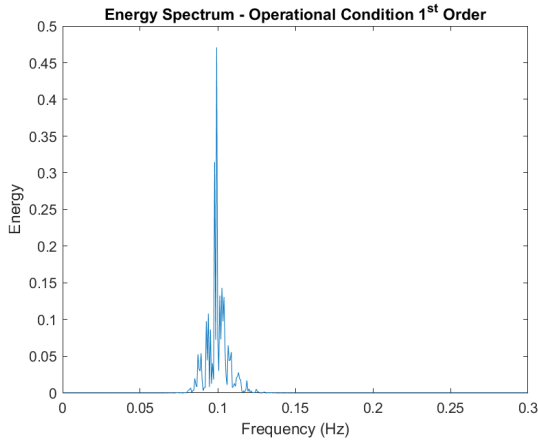
(a) 1st Order Diffraction Radiation.
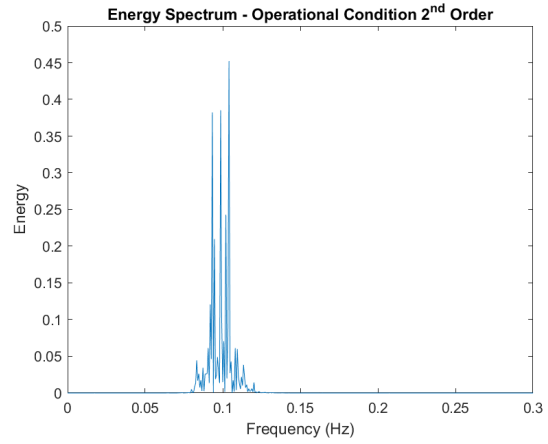
(b) 2nd Order Diffraction Radiation.

Figure 9.13: *Surge Energy Spectrum for Operational Condition.*
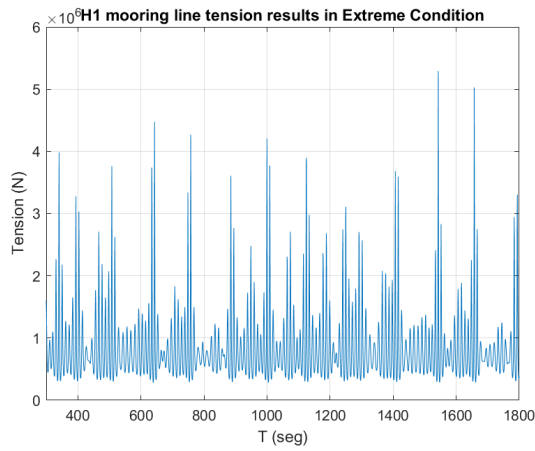
(a) *Extreme Condition.*
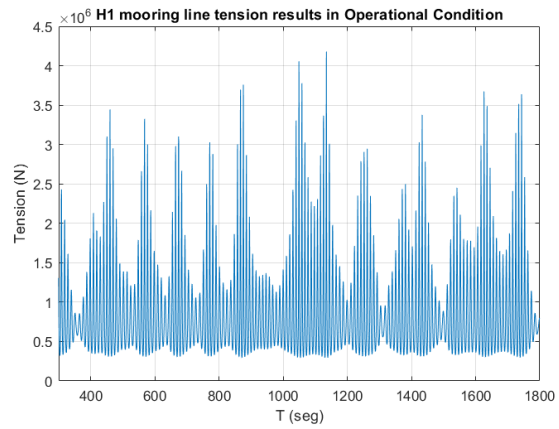
(b) *Operational Condition.*

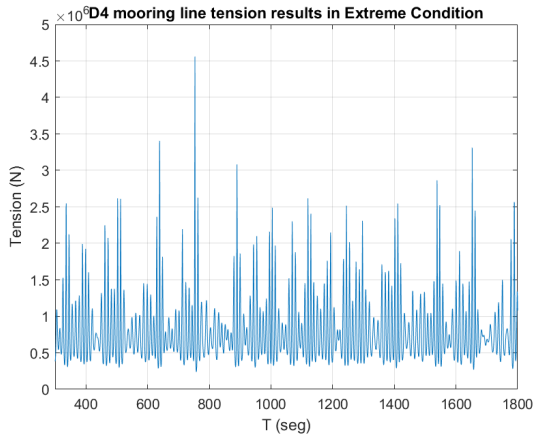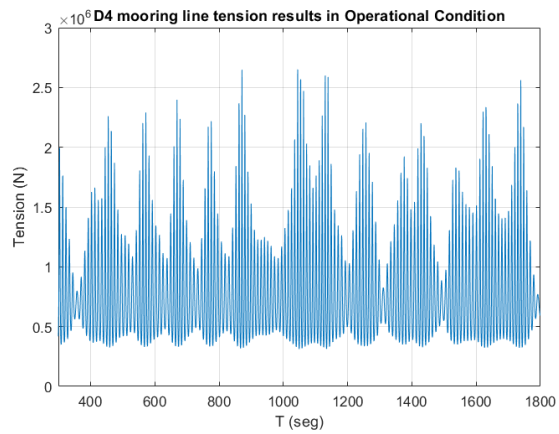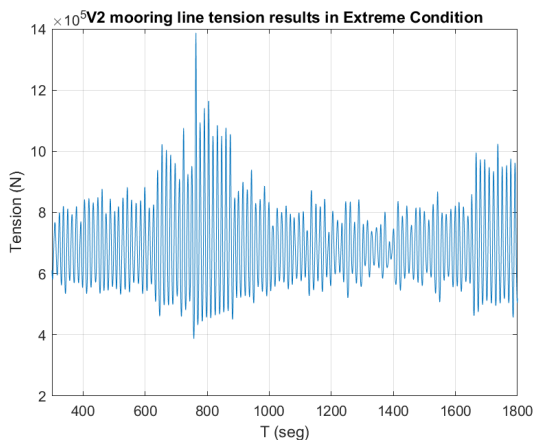Figure 9.14: *H1 Mooring Line Tension Results.*
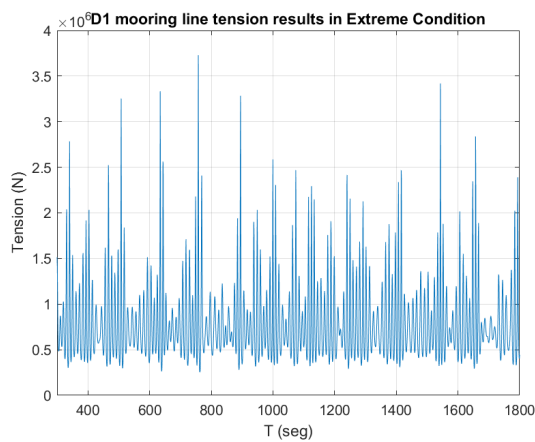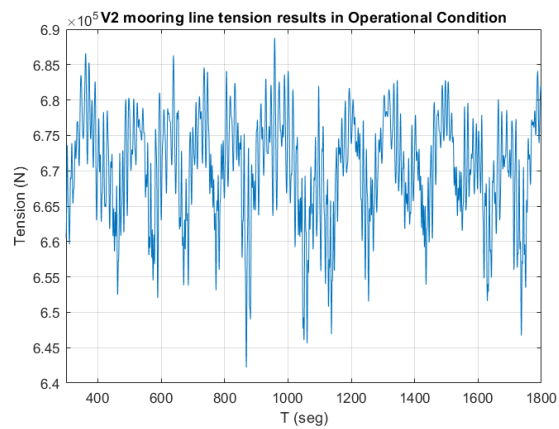

(a) *Extreme Condition.*
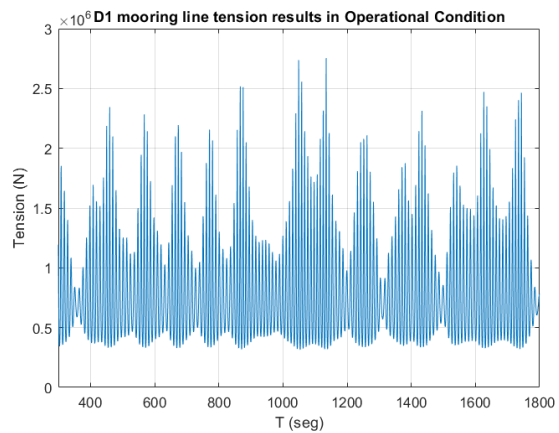
(b) *Operational Condition.*

Figure 9.15: *D1 Mooring Line Tension Results.*
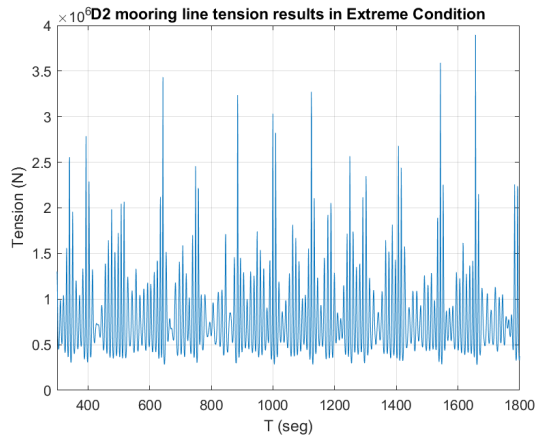
(a) *Extreme Condition.*
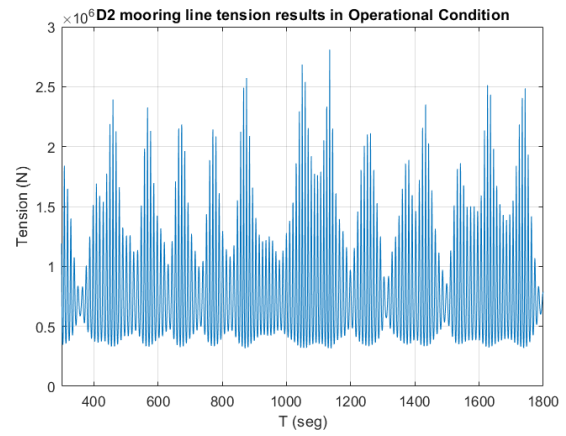
(b) *Operational Condition.*

Figure 9.16: *D2 Mooring Line Tension Results.*
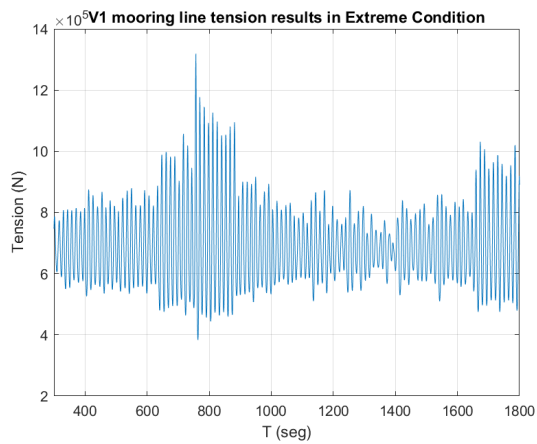
(a) *Extreme Condition.*
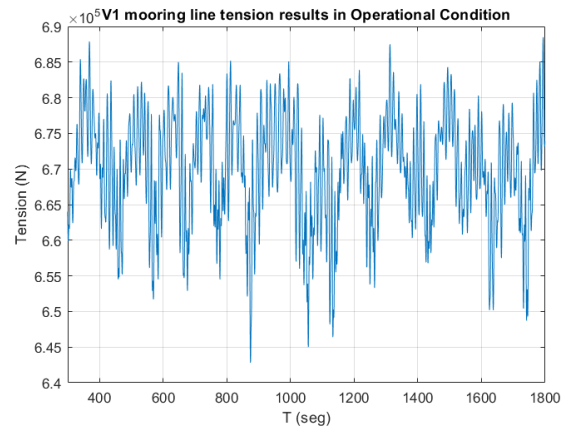
(b) *Operational Condition.*

Figure 9.17: *V1 Mooring Line Tension Results.*
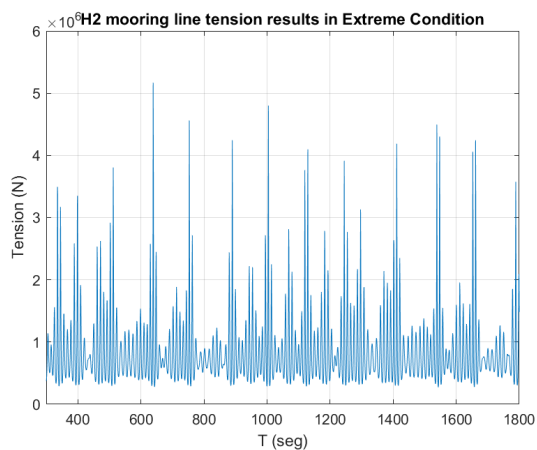
(a) *Extreme Condition.*
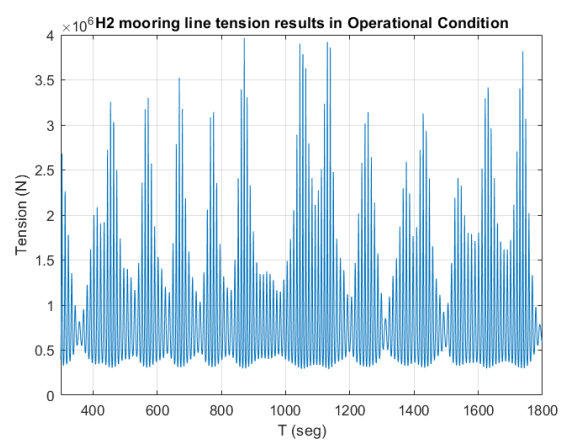
(b) *Operational Condition.*

Figure 9.18: *H2 Mooring Line Tension Results.*
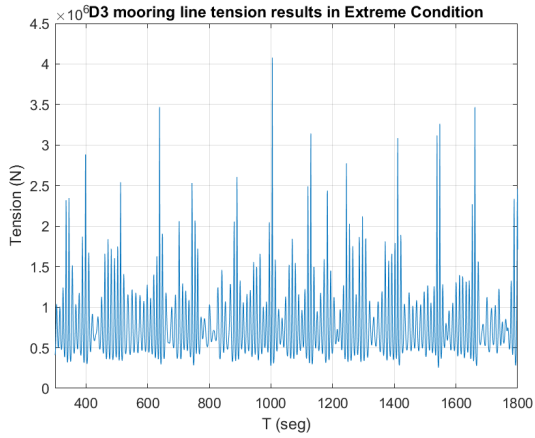
(a) *Extreme Condition.*
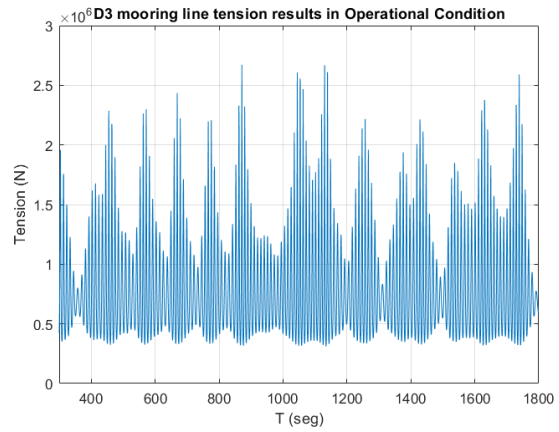
(b) *Operational Condition.*

Figure 9.19: *D3 Mooring Line Tension Results.*

(a) *Extreme Condition.*

(b) *Operational Condition.*

Figure 9.20: *D4 Mooring Line Tension Results.*

(a) *Extreme Condition.*

(b) *Operational Condition.*
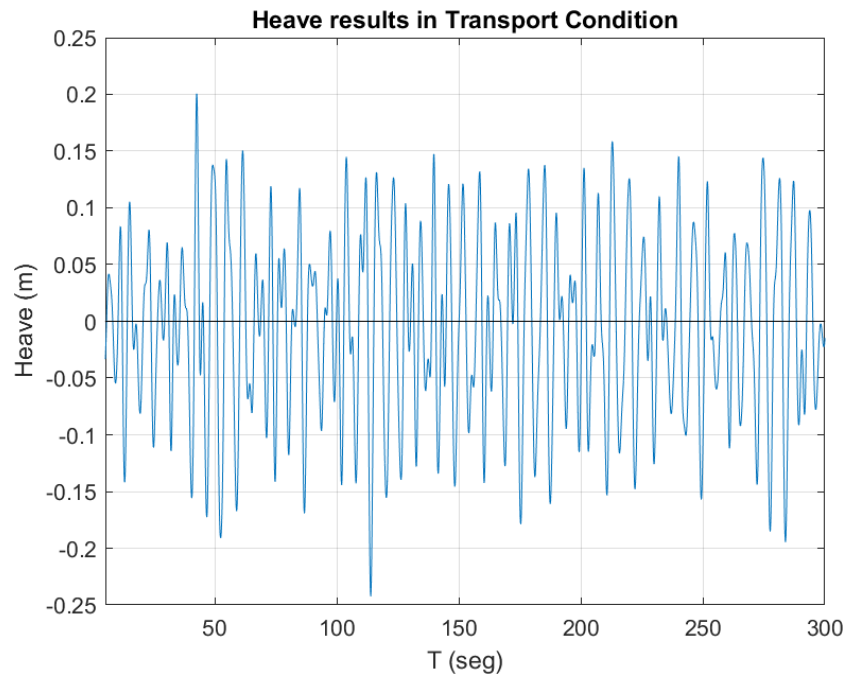
Figure 9.21: *V2 Mooring Line Tension Results.*

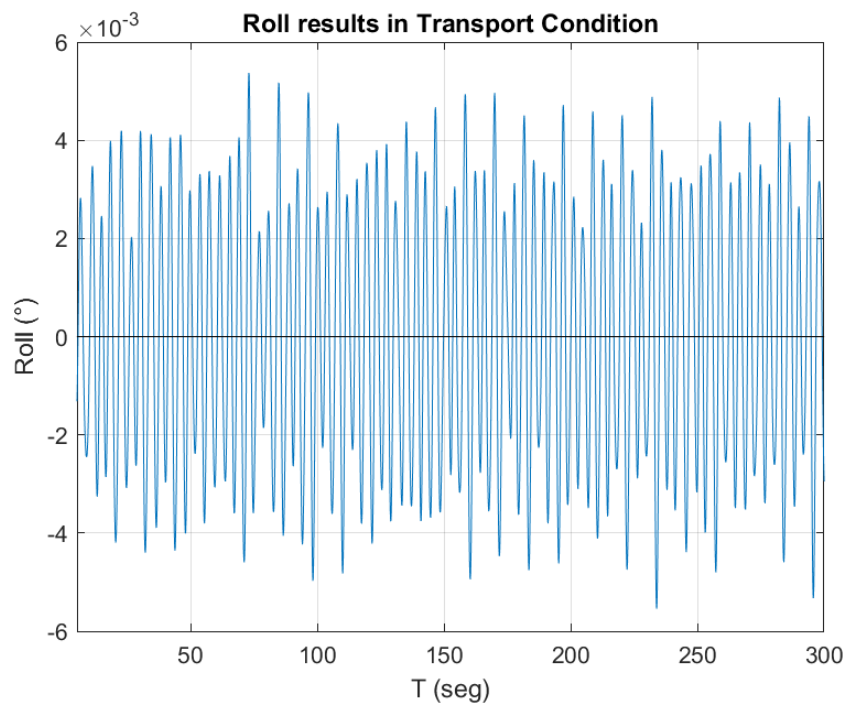Figure 9.22: *Heave Results for Transport Condition in a Time-Domain Signal.*

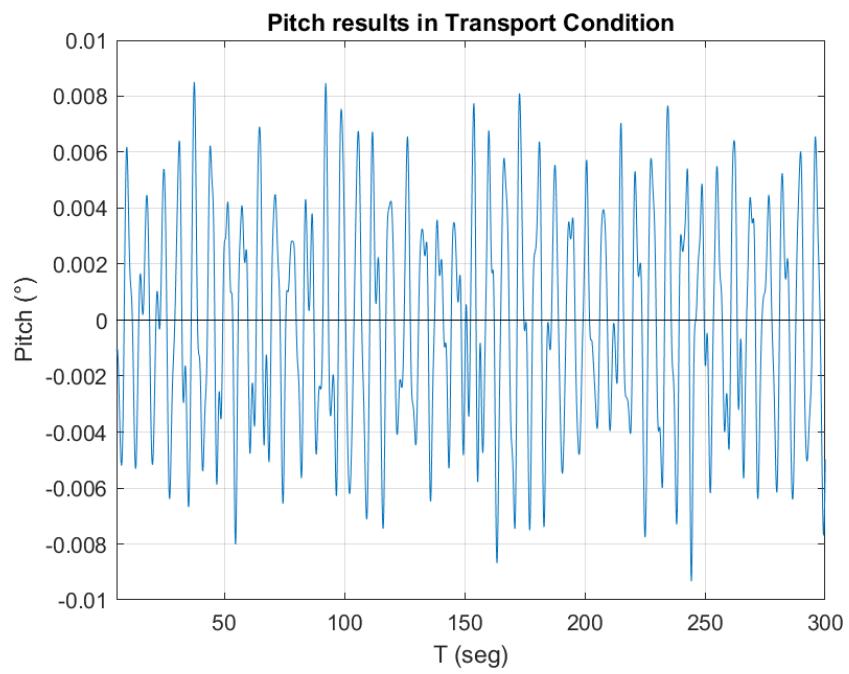Figure 9.23: *Roll Results for Transport Condition in a Time-Domain Signal.*

Figure 9.24: *Pitch Results for Transport Condition in a Time-Domain Signal.*